

Dynamic visualization of deposition processes within porous media by means of MRI

zur Erlangung des akademischen Grades eines
DOKTORS DER INGENIEURWISSENSCHAFTEN (DR.-ING.)

von der KIT-Fakultät für Chemieingenieurwesen und Verfahrenstechnik des
Karlsruher Instituts für Technologie (KIT)
genehmigte

DISSERTATION

von
M. Sc. Florian Ranzinger
aus Frankfurt am Main

Tag der mündlichen Prüfung: 18.2.2022

Erstgutachter: Prof. Dr. Harald Horn

Zweitgutachter: Prof. Dr. Hermann Nirschl

Acknowledgement

First of all I would like to express my thankfulness to Prof. Harald Horn for giving me the chance to start a PhD without research grant at his department and under his guidance. His knowledge, interest, and supervision has guided me through hard times and strongly influenced the outcome of my PhD.

I am grateful for the help and efforts of Michael Wagner who very much contributed to the visualization of image data and conceptualization of the manuscripts. The comments always helped me to improve my manuscript.

I thank Prof. Dr. Hermann Nirschl for taking over the role as co-reviewer.

Special thanks go to Prof. Dr. Gisela Guthausen and Pia Herrling for introducing me to the field of MRI within my bachelor thesis. Further, I am grateful for the opportunity to use the NMR facilities during my PhD. I acknowledged the discussions throughout my PhD. I am very thankful for the support and talks with the whole NMR group. Thank you Basti, Eva, Nico, Roland, and Thomas have for the cooperative working atmosphere.

I am very thankful for the opportunity to supervise students. Maximillian, Karin and Hachem all contributed with their results to the profile and outcome of my PhD. Further, I am grateful that I got to know each one of you.

I appreciated it very much to be a member of EBI. I will forever keep the moments and memories we shared together. Thanks go to all PhDs, namely Alex, Alondra, Amelie, Andreas, Annika, Damare, Giorgio, Hessam, Laure, Luisa, Max H., Max M., Michael S., Oliver, Peng, Phillip, Rowayda, Stephan, Yair who contributed to the nice working atmosphere within the PhD group. Special thanks go to Ali and Prantik for closely sharing the fun as well as hard times of a PhD. I am also thankful for the conversations and help I received from other sides of the institute. Thank you Alfred, Andrea, Axel, Birgit Gordalla, Ewa, Florencia, Gudrun Abbt-Braun, Katharina, Matthias, Norbert, Rafi, Reinhard, Steffi, Sylvia, Uli Reichert, Uli Scherer, Ursula Schäfer for all the support over the past years.

Last but not least I would like to thank my family, friends and my girlfriend Lea who supported me throughout the whole PhD.

Abstract

Porous media can be found in many technical as well as natural systems. Especially in the field of water treatment porous media are used within many purification steps. Their application ranges from the retention of particulate matter, to the adsorption of soluble compounds, and the settlement of microorganisms to enhance biodegradation. In many cases the operation is aligned with accumulations (e.g. biological or particulate origin) within the porous media, which can have a significant burden on the hydraulic properties and ultimately, on the process performance.

Imaging methods offer the possibility to dynamically resolve accumulation processes within porous media to gain a better understanding of these processes. However, the 3D-structure of porous media is only accessible to few imaging devices. In the present dissertation, magnetic resonance imaging (MRI) was used as it is an *in-situ*, non-invasive method that is not limited in penetration depth. A benefit of MRI aligns in the possibility to conduct flow measurements besides of structural images.

By means of MRI accumulation processes within porous media were addressed in respect to the specific application and current questions. Namely these are: (I) How does biofilm grow under alternating water level and how does biofilm effect the water retention? (chapter 2); (II) How is particulate matter retained once water is pumped into aerobic granular sludge (AGS) systems? (chapter 3); and (III) How is particulate matter retained by granulated activated carbon (GAC) filters and how does it influence the local flow field? (chapter 4).

In chapter 2 the biofilm growth under alternating water level was addressed. The approach allowed to visualize all four fractions (biofilm, porous media, water, air) dynamically and spatially resolved. Biofilm was found to preferentially grow within permanently wetted areas, mainly next to the contact points between two spheres or between sphere and glass column. To a lower extend biofilm was found on the free surface of spheres or within the void space. The water retention was increased due to biofilm growth after drainage events. Vice versa, more entrapment of air was found after the flushing events. Further, the connectivity within the liquid phase increased during the experiment indicating that biofilm might enhance diffusive transport processes under partially saturated conditions.

Chapter 3 addressed the transport and retention behavior of particles once they enter into aerobic granular sludge (AGS) systems. The results indicated that the size of particles governs their fate within AGS systems. Particles in the nanometer range were able to penetrate and immobilize within the biofilm. Overall the nanoparticles were immobilized near the surface and did not penetrate deeper than 300 μm . Particles in the micrometer range were retained at the surface of aerobic granules and accumulated within the voids. Due to the size of these accumulations, particles were to a large extent not in contact with the aerobic granules and thus, not attached. During the following aeration cycle of AGS systems, those particles will be redistributed together with the AGS itself and become available for the whole biomass for attachment and degradation.

Chapter 4 deals with the retention of suspended solids (SS) onto a granulated activated carbon (GAC) filter and its impact on the local flow field. During the top-down filtration, SS were retained above and within the GAC filter. The stepwise addition of wastewater allowed to observe the buildup of a deposit layer, redistribution within the porous media as well as changing inflow points and the occurrence of higher velocities. The occurrence of preferential inflow points revealed that the deposit layer did not cover the entire surface. Further, the ongoing accumulation within pore throats and the compaction of SS indicated potential ways to increase the pressure loss. Channeling was observed from the start of the experiment. With an equivalent velocity of 28.8 m/h the measurement is 2.3 times higher than assumed by applying an average filter velocity of 5 m/h, even when taking the porosity (40%) into account (12.5 m/h). The equivalent velocity further increased up to 100.8 m/h at the end of the experiment. Overall the filtration process remains unfavorable due to the compaction and ongoing pore blockage, which have the potential to drastically increase the pressure loss.

Overall the results highlight the suitability of MRI to resolve processes dynamically within porous media. Through individually chosen image analysis, parameter setting and experimental procedure it was possible to visualize the multi component systems in each case. Further, the results reveal unique observations of deposition mechanisms within porous media that extend the current knowledge and may serve for the optimization of the corresponding real scale applications.

Zusammenfassung

Poröse Medien finden sich in technischen oder natürlichen Systemen wieder. Speziell in der Wasser- und Abwasseraufbereitung sind poröse Medien weit verbreitet. So werden Festbettfilter gezielt zum Rückhalt von partikulären Stoffen verwendet, dienen der Adsorption von gelösten Stoffen, oder fungieren als Aufwuchsfläche für Mikroorganismen, um den biologische Abbau zu verbessern. Während dem Betrieb kommt es innerhalb der porösen Medien zu Ablagerungen, die einen maßgebenden Einfluss auf die hydraulischen Eigenschaften und damit einhergehend auf die Leistung dieser Verfahren nehmen können.

Mithilfe bildgebender Verfahren lassen sich detaillierte Aufnahmen der Ablagerungsvorgänge anfertigen. Diese dienen der qualitativen Prozessaufklärung realer Systeme und können zu deren Optimierung herangezogen werden. Aufgrund der 3-dimensionalen Struktur sind poröse Medien nur wenigen bildgebenden Verfahren zugänglich. In der gegenwärtigen Dissertation wurde die Magnetresonanztomographie (MRI; engl. Magnetic Resonance Imaging) verwendet, aufgrund der Möglichkeit Aufnahmen *in-situ*, zerstörungsfrei und ohne Tiefenlimitierung anzufertigen. Zudem lassen sich mithilfe der MRI neben strukturellen Aufnahmen auch Strömungsmessungen durchführen.

In der gegenwärtigen Arbeit wurde sich im Detail mit den folgenden drei Themen befasst: (I) Dem Aufwuchs von Biofilm auf ein poröses Medium unter alternierender Wasserverfügbarkeit; (II) Dem Verbleib von Partikeln innerhalb von granulierten Belebtschlammbecken während dem anaeroben Füllen des Reaktors; (III) der Abscheidung von Partikeln innerhalb von granulierten Aktivkohlefiltern und der einhergehenden Veränderung des Strömungsfeldes.

In Kapitel 2 wurde das Wachstum von Biofilm unter zyklischen Entwässerungs- und Bewässerungsphasen thematisiert. Der Versuch erlaubte die Visualisierung aller vier Bestandteile (Biofilm, poröses Medium, Wasser und Luft). Es zeigte sich, dass der Biofilm hauptsächlich an Porenhälsen aufwuchs, die permanent Flüssigkeitsbedeckt blieben. Zu geringerem Ausmaß wurde der Bewuchs von Hohlräumen oder freier Oberflächen festgestellt. Durch das Biofilmwachstum wurde die Wasserrückhaltung nach Entwässerung erhöht. Im Gegenzug erhöhte sich ebenfalls der Einschluss von Luft nach zyklischer Wasserzufuhr. Zusätzlich konnte eine erhöhte Konnektivität der

Wasserphase nachgewiesen werden. Dies deutet darauf hin, dass der Biofilm Stoffübergangsprozesse in teilgesättigten porösen Medien durch den Rückhalt von Wasser verbessert.

Kapitel 3 thematisiert den Transport und Rückhaltemechanismen verschiedener Partikelgruppen innerhalb von porösen Medien aus granuliertem Belebtschlamm. Im Falle der aeroben Granula wurde gezeigt, dass der Rückhalteprozess von Partikeln größenabhängig ist. Die Partikel im Nanometerbereich waren in der Lage die aeroben Granula zu penetrieren. Gleichzeitig fand eine Immobilisation innerhalb des Biofilms statt, wodurch die Nanopartikel an der Oberfläche des Biofilms immobilisierten und nicht tiefer als 300 µm eindrangen. Die Partikel im Mikrometerbereich konnten zu einem Großteil abgefangen werden und sammelten sich in den Hohlräumen zwischen den aeroben Granula an. Ein Eindringen der Partikel in den Biofilm wurde nicht festgestellt. Aufgrund der Größe der Anhäufungen wird deutlich, dass diese überwiegend nicht direkt an den aeroben Granula anhaften, sondern sich vielmehr in den Hohlräumen ansammeln. In der darauffolgenden Belüftungsphase des Reaktorbetriebs werden Partikelansammlungen mitsamt den aeroben Granula aufgewirbelt, wodurch die Partikel der gesamten Biomasse zwecks Anhaftung und Abbau zur Verfügung stehen.

In Kapitel 4 befasst sich mit der Rückhaltung von partikulären Stoffen (SS; engl. suspended solids) auf einem granulierten Aktivkohlefilter (GAC; engl. granulated activated carbon). Bei abwärts gerichteter Durchströmung wurden SS sowohl auf als auch innerhalb des GAC-Filters zurückgehalten. Durch die schrittweise Zugabe von SS konnte der Aufbau des Filterkuchens, Umschichtungen im porösen Medium als auch Änderungen der Einströmwege und Fließgeschwindigkeiten detailliert erfasst werden. Das Auftreten von bevorzugten Einströmwegen hebt hervor, dass die Deckschicht nicht die komplette Oberfläche bedeckte, und SS tiefer in das poröse Medium eingetragen wurden. Neben der Bedeckung des Filters, zeigte eine zunehmende Blockade von Porenhälsen und Komprimierung von SS mögliche Gründe für die schnell ansteigenden Druckverluste auf, die in realen oder pilot-Anlagen beobachtet wurden. Channeling war bereits vor Beginn der Filtration präsent. Hier zeigt sich das mit einer Äquivalentgeschwindigkeit von 28.8 m/h, der GAC Filter weitaus schneller durchströmt wird wie erwartet. Die Grundannahme einer mittleren Fließgeschwindigkeit von 5 m/h bzw. 12.5 m/h (inklusive Porosität), wurde um den Faktor 2,3 übertroffen. Mit zunehmender Filtrationsdauer wurden die

Channelingeffekte deutlicher. Nach 3.75 h wurde eine Äquivalentgeschwindigkeit von 68.4 m/h gemessen, die nach 7.75 h auf 100.8 m/h anstieg. Insgesamt ist der Filtrationsprozess aufgrund des rasch zu erwartenden Druckanstiegs nachteilig, weshalb eine separierte und vorgeschaltete Filtration plausibler für die Prozessführung erscheint.

Die Ergebnisse verdeutlichen die Eignung der MRI zur Prozessaufklärung von Ablagerungsprozessen in porösen Medien. Mithilfe der MRI war es möglich, Multikomponentensysteme durch die Auswahl der Aufnahmeparameter und weitergehender Bildanalyse zu visualisieren und zeitlich nachzuverfolgen. Weiterhin stellen die Ergebnisse einzigartige Abbildungen der Ablagerungsvorgänge dynamisch dar, die das bestehende Wissen erweitern und zur Optimierung großtechnischer Prozessabläufe beitragen können.

Publications

The chapters 2 and 3 of this dissertation have been published in the first and second of the following peer-reviewed articles.

Ranzinger, Florian, Karin Schröter, Harald Horn, and Michael Wagner. "Investigation of Biofilm Growth within a Monodisperse Porous Medium under Fluctuating Water Level Assessed by Means of MRI." *Water* 13, no. 18 (2021): 2456. <https://doi.org/10.3390/w13182456>

Ranzinger, Florian, Maximilian Matern, Manuel Layer, Gisela Guthausen, Michael Wagner, Nicolas Derlon, and Harald Horn. "Transport and retention of artificial and real wastewater particles inside a bed of settled aerobic granular sludge assessed applying magnetic resonance imaging." *Water research* X 7 (2020): 100050. <https://doi.org/10.1016/j.wroa.2020.100050>

Layer, Manuel, K. Bock, **Florian Ranzinger**, Harald Horn, Eberhard Morgenroth, and Nicolas Derlon. "Particulate substrate retention in plug-flow and fully-mixed conditions during operation of aerobic granular sludge systems." *Water research* X 9 (2020): 100075. <https://doi.org/10.1016/j.wroa.2020.100075>

Ranzinger, Florian, Andrea Hille-Reichel, Erwin Zehe, Gisela Guthausen, and Harald Horn. "Quantification of evaporation and drainage processes in unsaturated porous media using magnetic resonance imaging." *Water Resources Research* 56, no. 2 (2020): e2019WR026658. <https://doi.org/10.1029/2019WR026658>

Cuny, Laure, Daniel Pfaff, Jonas Luther, **Florian Ranzinger**, Peter Ödman, Johannes Gescher, Gisela Guthausen, Harald Horn, and Andrea Hille-Reichel. "Evaluation of productive biofilms for continuous lactic acid production." *Biotechnology and bioengineering* 116, no. 10 (2019): 2687-2697. <https://doi.org/10.1002/bit.27080>

Ranzinger, Florian, Maria P. Herrling, Susanne Lackner, Vanessa W. Grande, Amer Baniodeh, Annie K. Powell, Harald Horn, and Gisela Guthausen. "Direct surface visualization of biofilms with high spin coordination clusters using magnetic resonance imaging." *Acta biomaterialia* 31 (2016): 167-177. <https://doi.org/10.1016/j.actbio.2015.12.007>

Guthausen, Gisela, Julyana R. Machado, Burkhard Luy, Amer Baniodeh, Annie K. Powell, Steffen Krämer, **Florian Ranzinger**, Maria P. Herrling, Susanne Lackner, and

Harald Horn. "Characterisation and application of ultra-high spin clusters as magnetic resonance relaxation agents." *Dalton Transactions* 44, no. 11 (2015): 5032-5040. <https://doi.org/10.1039/C4DT02916J>

The following manuscript has been submitted to peer-reviewed journals and is further listed in chapter 5 of this dissertation:

Ranzinger, Florian, Harald Horn, and Michael Wagner. "Locally and time resolved imaging of particle deposition within a granulated activated carbon filter – Impact on the flow field" Submitted on 25.10.21 to Water Research

Contents

1	Fundamentals	1
1.1	Porous media in water treatment.....	1
1.2	Particle retention in porous media	3
1.2.1	Particle transport towards porous media.....	3
1.2.2	Particle attachment at porous media.....	4
1.2.3	Filtration mechanisms	5
1.3	Biofilms and porous media	7
1.3.1	Biofilm growth within porous media.....	7
1.3.2	Aerobic granular sludge	9
1.4	Imaging techniques for the visualization of deposition processes within porous media.....	13
1.4.1	MRI	13
1.4.2	X-ray computed tomography.....	15
1.4.3	Neutron computed tomography.....	17
2	Investigation of Biofilm Growth within a Monodisperse Porous Medium under Fluctuating Water Level Assessed by Means of MRI (Published in MDPI Water)	18
2.1	Introduction.....	18
2.2	Materials and Methods	20
2.2.1	Experimental Setup and Procedure	20
2.2.2	Cultivation	21
2.2.3	Optical Coherence Tomography (OCT)	22
2.2.4	Magnetic Resonance Imaging (MRI).....	22
2.2.5	Image Analysis.....	23
2.3	Results	24
2.3.1	Dynamics of Water Content	24
2.3.2	Biofilm Growth.....	25
2.3.3	Analysis of Liquid Phase	26

2.4	Discussion	30
2.4.1	Applicability of the MRI Approach	30
2.4.2	Biofilm Growth under Fluctuating Water Level	30
2.4.3	Impact of Biofilm on the Liquid Phase	31
2.5	Conclusions	32
3	Transport and retention of artificial and real wastewater particles inside a bed of settled aerobic granular sludge assessed applying magnetic resonance imaging (Published in Water Research X)	33
3.1	Introduction.....	33
3.2	Material and Methods	35
3.2.1	Aerobic granular sludge	35
3.2.2	Preparation and characterization of particulate organic matter	35
3.2.3	Experimental setup and procedure	37
3.2.4	Adjusted parameters between experimental runs	38
3.2.5	Magnetic resonance imaging	39
3.2.6	Data analysis and visualization	40
3.3	Results	42
3.3.1	Experiment 1: Behavior of colloidal particles (SPIONs)	42
3.3.2	Experiment 2: Behavior of microcrystalline cellulose particles (MCPs) ..	43
3.3.3	Experiment 3: Behavior of real wastewater particles (WWPs)	44
3.3.4	Comparison of particle distribution.....	45
3.4	Discussion	48
3.4.1	Applicability of MRI	48
3.4.2	Particle retention	48
3.4.3	Influence of flow velocity on particle distribution	49
3.5	Conclusions.....	50
4	Locally and time resolved imaging of particle deposition within a granulated activated carbon filter – Impact on the flow field (Submitted).....	51
4.1	Introduction.....	51
4.2	Materials & Methods.....	53

4.2.1	Pretreatment	53
4.2.2	Magnetic Resonance Imaging (MRI).....	53
4.2.3	54
4.2.4	Experimental setup	54
4.2.5	Image analysis	56
4.2.6	Processing of Flow images	56
4.2.7	3D-image analysis:	57
4.3	Results	58
4.3.1	Particle retention and GAC redistribution.....	58
4.3.2	Flow distribution above and within the GAC filter.....	60
4.4	62
4.5	Discussion:	63
4.5.1	Retention of SS in GAC filters is affected by local flow field	63
4.5.2	Impact of volume flow distribution on GAC	64
4.6	Conclusions:.....	65
5	Summary:.....	66
6	Appendix.....	70
6.1	Appendix 2-1: Cultivation under saturated condition for OCT measurements 70	
6.2	Appendix 2-2: Visualization of liquid clusters.....	71
6.3	71
6.4	Appendix 3-1: Image segmentation; analysis and direct comparison	72
6.5	Appendix 5-1: Merging of structure and flow datasets.....	73
7	Nomenclature.....	79
8	References:.....	80

List of Figures

Figure 1-1: Transport processes towards the surface of a porous media after Sutherland and Chase (2011). Particles can be transported towards the surface of a porous medium due to straining (a), interception (b), inertia (c), sedimentation (d), and diffusion (e). Often several transport mechanisms are occurring simultaneously. 4

Figure 1-2: Filtration mechanisms after Sutherland and Chase (2011) applied on packed beds. Commonly sieve filtration (a), depth filtration (b), and cake filtration (c) are distinguished. If none of the above mentioned filtration mechanisms is dominant, intermediate filtration might occur. 6

Figure 1-3: Potential ways of biofilm coverage within porous media: (a) void space coverage; (b) surface coverage; (c) pore throat coverage; (d) discontinuous coverage; (e) streamer shaped growth..... 9

Figure 1-4: Sketch of an aerobic granule. Within the specific zones (aerobic, anoxic and anoxic layer) specific consortia of microorganisms settle and allow for the degradation of carbon, nitrogen and phosphorous sources within one treatment (After Wilén et al. (2018)).11

Figure 1-5: Biological treatment via AGS within sequencing batch reactors. Within the feast-phase (a) fresh wastewater enters from the bottom and COD is taken up by anaerobic metabolizing microorganisms. Within the famine-phase (b) the metabolization is taking place under aerobic conditions. During settling (c) the AGS settles at the bottom of the reactor while forming a porous medium after HaskoningDHV (2020).....12

Figure 2-1: Experimental setup of the MRI experiments. Flushing (a) and drainage (b) events were conducted in alternating order. The timing of work flows is highlighted in (c). In the flushed and drained conditions, both pumps were turned off to acquire images in a static state.21

Figure 2-2: Two-dimensional MRI images displaying the normalized signal intensity in the flushed (a) and drained (b) conditions on days 6, 9, and 12. (a) Biofilm growth can be recognized in the form of dark regions appearing next to contact points of glass spheres. For further clarification, view the highlighted animation. (b) Water retention increases within the porous medium due to the growth of biofilm. Regions of interest (ROIs) that reveal occurring changes are highlighted in red.....24

Figure 2-3: OCT B-Scans acquired from a previous experiment under permanently saturated conditions. (a) Three glass spheres before inoculation. (b) After 6 days, biofilm could be found on the particle surface in the form of small colonies. (c) Biofilm covered the voids between the particles and the column wall after 14 days. A biofilm as distinct as in (c) was accessible by means of MRI.....26

Figure 2-4: Processed 3D images on days 6, 9, and 12 (a) in the flushed condition, (b) in the drained condition, and (c) analyzed for liquid clusters. Solid material (glass column; porous medium) is superpositioned and displayed in grey. The liquid phase is presented in blue. Air is removed from the visualization (transparent areas). Based on row b, the liquid phase was analyzed for connectivity and divided into isolated liquid clusters. Each color represents a separate liquid cluster. Please note that more liquid clusters than colors are shown in (c); therefore, one color might also represent multiple isolated liquid clusters.27

Figure 2-5: Quantification of water content (a) and the total amount of liquid clusters $N_{cluster}$, as well as the volumetric Euler number χV (b) over time. Water content decreased in the flushed condition, while water retention in the drained condition increased. Furthermore, the connectivity of the liquid phase in the flushed condition increased, as indicated by the volume of the largest cluster (a) and the volumetric Euler number (b).....29

Figure 3-1: Experimental setup. MRI images were acquired along the first 22.5 mm of the granular sludge bed, according to the flow direction.....38

Figure 3-2: 2D MRI images (cross-sections) showing the distribution and sorption of SPIONs within the granular sludge bed. $T1$ -weighted images (a) allow for a differentiation between granules and water filled pore space, while $T2$ -weighted images (b) are more sensitive to SPION concentrations (e.g. particle load). The presence of SPIONs in the liquid enhances mainly $T2$ -relaxation, but markedly affects also the $T1$ -contrast. Sorption of SPIONs to granules is indicated as their surface becomes visible in terms of “dark” rings in $T2$ -weighted images.42

Figure 3-3: 2D MRI images showing the accumulation of microcrystalline cellulose particles (MCPs) in the granular sludge bed. *T1*-weighted images (a) allow for a differentiation between granules and water filled pore space, while *T2*-weighted images (b) are more sensitive to the particle load in form of low intensity signals. The granule bed reordered during the particle load, and a flow channel formed. An accumulation of MCPs occurred mainly near the inlet and along the flow channel (preferential flow path).....44

Figure 3-4: 2D MRI images showing the accumulation of real wastewater particles (WWPs) within the granular sludge bed. In *T1*-weighted images (a) granules, water filled pore space (low signal intensity) and particles (high signal intensity) are visible. The *T2*-weighted images (b) display the particles more homogenously. Particles appear dark (low signal intensity) whereas the water filled pore space and granules appear grayish (high signal intensity). The particles accumulated mainly within a channeled void space of the granular sludge bed.45

Figure 3-5: Volume fractions at the end of each experiment. SPIONs are able to penetrate the granules (white bars), while the WWPs and MCPs accumulate in the void space.....46

Figure 3-6: Particle distribution along height. In experiment 1 the SPIONs distributed homogenously along the height of the granular sludge bed. The accumulation of MCPs in experiment 2 is mainly affected by the geometry of the flow path. The amount of accumulated WWPs in experiment 3 decreases sharply within the first millimeters. .47

Figure 4-1: Experimental setup of the MRI experiments. In each cycle 0.2 L of pretreated wastewater were added to the GAC packed column. The upper 1.5 cm and liquid phase above the GAC filter were investigated in time and spatially resolved image series.55

Figure 4-2: Image analysis of 3D measurements. Datasets recorded with the lowest (3.75 ms) and highest (15 ms) echo time were used. After image processing both datasets were merged and further rendered for 3D visualization only.....57

Figure 4-3: Normalized 2D-images show the GAC filter structure and the accumulation of SS. With ongoing addition of wastewater, SS accumulation is dominantly observed at the bulk – GAC interface, resulting in a deposit layer.58

Figure 4-4: Rendered 3D images and height profiles of the experiment after 0 L; 3.2 L and 6.4 L of wastewater passed through the GAC filter. Particles accumulate above GAC filter by formation of a deposit layer. In addition, the accumulation of SS the GAC filter is shown.....59

Figure 4-5: 2D sagittal flow images revealing flow profiles within the bulk liquid above the GAC filter. The accumulation of SS causes redistributions of GAC and accumulated SS at the top of the GAC filter aligned with changing inflow points into the GAC filter. Formation of channeling can be recognized.60

Figure 4-6: Axial flow maps before (I), after 3.0 L (II) and 6.2 L (III) addition of wastewater. Corresponding volume flow distributions are presented in (IV) as probability density and (V) cumulative density function. Characteristic values of Table 4-2 (mode and equivalent velocity) are highlighted within the diagram. The accumulation of SS promotes channeling effects and leads to higher equivalent velocities.....61

1 Fundamentals

1.1 Porous media in water treatment

Packed bed filters are applied within several purification steps in water treatment due to their simple design and operation. The treatment is adapted from nature as water is purified by passing through river banks or soils (Crittenden et al. 2012). Dependent on its integration, the treatment may serve the following purification purposes in water treatment (Crittenden et al. 2012, Gujer 1999, Jekel and Czekalla 2016):

- to retain suspended solids
- to retain colloids and lower turbidity
- to reduce microbial content
- as habitat for microorganisms ongoing with biological degradation of chemical compounds
- as adsorbent material for dissolved chemical compounds

Dependent on the aim of the treatment step a variation of operation and filter material can be found. The porous media may consist of sand, lava rock, pumice, gravel, plastic, or granular activated carbon (Crittenden et al. 2012). Further, a combination of materials is possible in dual media filters. Due to operational cost, the height potential between inlet and outlet is commonly used as driving force to create a flow in top-down direction. Treatments are further divided in respect to their filter velocity. Slow sand filtration (0.06 – 0.3 m/h) aims at removing suspended solids, turbidity, microorganisms, and allows for sufficient time for biological degradation (Gujer 1999). The development of a “Schmutzdecke” is aligned with the ripening during slow filtration. In here, the major fraction of suspended particles, microorganisms, and colloids is retained due to the “Schmutzdecke” at the filter surface (Gujer 1999). However, within urban areas higher throughputs and more compact designs are often required. To increase throughput, rapid filtration with filter velocities of 6 – 15 m/h is applied, which primarily aims at decreasing the amount of suspended solids (Gujer 1999). In here, particle retention is achieved throughout the whole filter height via deep bed filtration (Crittenden et al. 2012, Gujer 1999). During operation microorganisms can settle on the filter material and lead to the formation of biofilms. Due to the biological degradation of chemical compounds the formation of biofilms is often seen as a desirable aspect (Crittenden et al. 2012, Gujer 1999, Jekel and Czekalla 2016).

Chapter 1: Fundamentals

However, in both cases the hydrodynamic conditions are altered during operation and may require backwashing to a certain extent (Crittenden et al. 2012, Gujer 1999, Jekel and Czekalla 2016).

In the following, the mechanisms of particle filtration within porous media are further outlined in chapter 1.2. In addition details on the biofilm growth onto porous media are provided in chapter 0. Finally, imaging methods to study alterations within porous media (i.e. biofilm growth or particle retention) are introduced and an overview on applications is provided (chapter 1.5).

1.2 Particle retention in porous media

Overall the particle retention within porous media can be divided into transport (chapter 1.2.1) and attachment processes 1.2.2. Further, the retention of particles results in filtration mechanisms which are outlined in chapter 1.3.

1.2.1 Particle transport towards porous media

For simplification purposes the fundamental transport processes are reduced to a single particle in the liquid which is introduced within an applied flow field. The flow field within packed beds in wastewater treatment is typically laminar. This implies that flow usually follows streamlines. The first step of retention is the transport from the liquid phase towards the surface of the porous media. For the case that particles strictly follow a streamline, scenario (a) and (b) are plausible transport scenarios:

Straining (a) occurs if a particle is too large in diameter and retained by the smaller pore throat. In that case, the pore throat might be entirely blocked.

Interception (b) becomes relevant if particles pass a porous structure on a streamline which is located close enough to get attracted by surface forces.

If the density of the particle is higher than of the liquid, the particles will not entirely follow streamlines (Crittenden et al. 2012). Thus, the scenarios (c), (d), and (e) are plausible:

Inertia (c) may cause the transport towards a porous structure as particles are not able to follow a streamline. The difference in trajectory can lead to a collision between particle and packed bed. The effect can be increased by applying higher average filter velocities.

Sedimentation (d) can become important for large particles with a significant higher density than water. The sedimentation velocity can be described according to Stokes' law.

Diffusion (e) due to Brownian movement particles can randomly move independent of the streamlines. The process becomes relevant with decreasing diameter. For particles larger than 1 μm drag forces become restrictive and allow to neglect diffusion.

In addition, electrostatic attraction and hydrodynamic conditions (turbulence) can transport particles towards the porous media. However, these can be neglected within the field of water treatment.

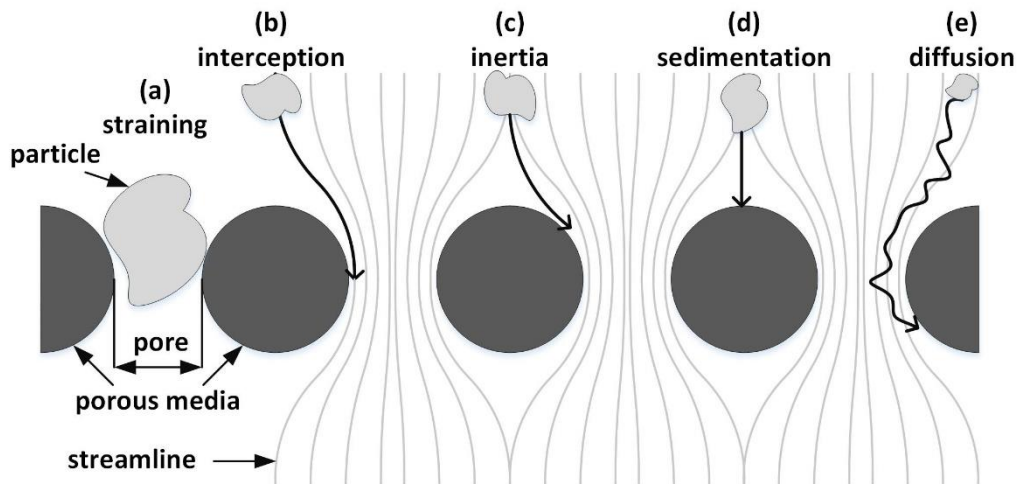


Figure 1-1: Transport processes towards the surface of a porous media after Sutherland and Chase (2011). Particles can be transported towards the surface of a porous medium due to straining (a), interception (b), inertia (c), sedimentation (d), and diffusion (e). Often several transport mechanisms are occurring simultaneously.

Overall, the above listed transport processes do not necessarily exclude each other. Thus, particles are likely affected by several of the mentioned transport processes at the same time (Crittenden et al. 2012).

1.2.2 Particle attachment at porous media

After a transport towards the porous media, particles have to be attracted to ensure an attachment. In here attracting forces in form of van der Waals forces and repulsive forces in form of electrostatic forces counteract each other. The resulting force can be described according to the DLVO theory and results in two characteristic minima. The first minimum at very short distances is irreversible due to the strong attracting force. However, a repulsive maximum must be overcome to bring particles close enough. The second minimum is characterized by a much lower energy barrier to overcome and lower attractive forces. Therefore, particles can be disconnected by shear forces, which allow for a reversible attachment process (Anlauf 2019, Crittenden et al. 2012). In water treatment most particles possess negative surface charges which result in strong electrostatic repulsion. Possibilities to lower electrostatic repulsion and thus, to improve attachment of particles are the addition of positive charged flocculent or an adjustment of pH-Value towards the isoelectric point.

1.3 Filtration mechanisms

Dependent on the particle size, flow velocity, concentration of particles and pore size different filtration mechanism occur. In addition, the dominant effect may change with ongoing filtration time. With ongoing particle deposition not only the interaction between particle and porous medium have to be considered but also the particles can retain themselves by creating a deposit layer. The characteristic filtration models are described below:

- (a) Sieve filtration occurs when the particle size is in a similar size range than the pore throat. Thus, pore throats might be completely blocked leading to a strong pressure drop (Anlauf 2019). Even though, sieve filtration is unlikely to be completely avoided the extend should be reduced by preconditioning of particle size and/or avoiding typical particle size close to the dimension of the pore throat.
- (b) Depth filtration is often desired for packed bed filters, as the particle depositions are distributed over the whole filter height which allows for a higher loading per cycle (Altmann et al. 2016, Jekel and Czekalla 2016). The mechanism is favored by using coarse porous materials compared to the particle sizes.
- (c) Cake filtration is occurring at the filter surface. In here, particles form bridges over pore throats that still allow for a flow to pass through the pore (no entire blockage). Ongoing particle retention is taking place by the particles itself. The process is preferred in many engineering applications, as the pressure drop increases less than compared to other filtration mechanisms. Further, the filter cake can be taken off at specific height to lower the pressure drop. Cake filtration is favored by applying very low filtration velocities in water treatment (Crittenden et al. 2012, Gujer 1999, Jekel and Czekalla 2016). Industrial applications take advantage of pretreatments like agglomeration and/or slurry conditioning (Anlauf 2019).
- (d) In some cases intermediate filtration mechanisms develop. Such filtration processes possess a stronger pressure drop with time than cake filtration but a lower than deep bed filtration (Anlauf 2019).

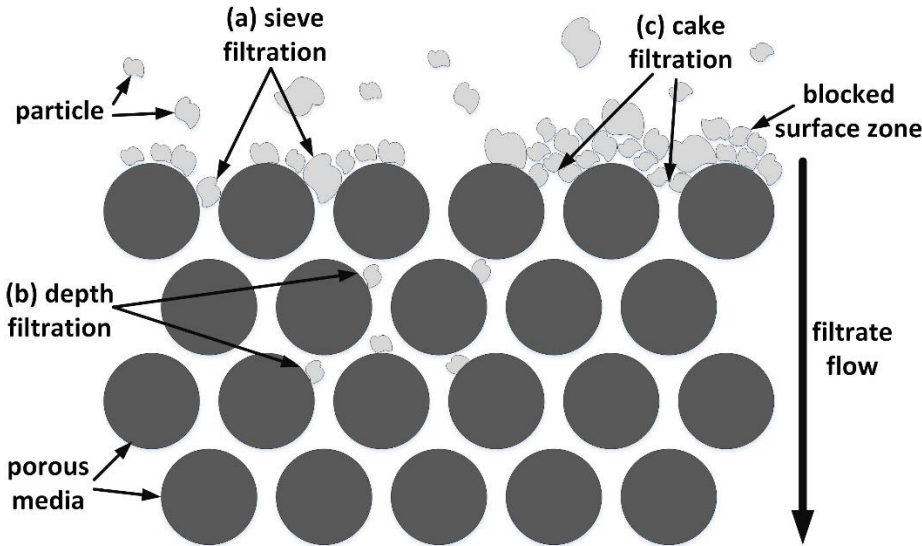


Figure 1-2: Filtration mechanisms after Sutherland and Chase (2011) applied on packed beds. Commonly sieve filtration (a), depth filtration (b), and cake filtration (c) are distinguished. If none of the above mentioned filtration mechanisms is dominant, intermediate filtration might occur.

1.4 Biofilms and porous media

1.4.1 Biofilm growth within porous media

In a first approach bacteria in porous media could be reduced to its cell size of typically 0.2 – 1 μm . However due to the biological activity, ongoing with reproduction of cells and excretion of extracellular polymeric substance (EPS), it becomes clear that the occupation of porous media by microorganisms is influenced by several aspects, retention mechanisms being one aspect among others.

In natural or engineered systems microorganisms are often exposed to harsh or fluctuating conditions in form of shear, nutrient supply, water availability or temperature (Tecon and Or 2017). A common response of bacteria to stressful conditions is surface attachment and the production of EPS, which lead to the formation of biofilms (Flemming and Wingender 2010). With commonly 75 – 90 % the EPS matrix far exceeds the volumetric content of cells within biofilms (Costerton 1999). The EPS matrix is composed of polysaccharides (40 - 95 %), proteins (< 1 - 60 %), nucleic acids (< 1 - 10 %), lipids (< 1 - 40 %), inorganic compounds and humic substances (Flemming and Wingender 2010). Overall, the EPS matrix offers multiple advantageous for microorganisms located within a biofilm compared to a planktonic life-style.

Some functions of EPS are (Flemming and Wingender 2010, Or et al. 2007a, Tecon and Or 2017):

- enhancement of adhesion to surfaces,
- aggregation of bacterial cells enhancing symbiotic effects,
- enhancement of mechanical stability and protection against shear forces,
- retention of water and enhancement of desiccation tolerance,
- protective barrier against predators or antimicrobial agents,
- storage of nutrients,
- sorption of compounds and enzymatic activity.

Within porous media alterations of the hydraulic properties are commonly observed due to the growth of biofilms. Dependent on the application differences in the extend of biofilm coverage can be found. Biofilms within soil typically consist of a few micrometer thick biofilms with web like structures close to grain-grain contact points (Or et al. 2007a, Tecon and Or 2017). On the other hand an extensive growth of biofilm

Chapter 1: Fundamentals

is observed in technical system which can lead to a recognizable pressure drop or even clogging of the systems, similar to filtration processes (Kim et al. 2010, Pintelon et al. 2012, Volk et al. 2016).

In regard of the pore size accumulation several forms of biofilm coverage are known and may affect the hydraulic properties of a porous media in different ways. Possible scenarios are:

(a) an accumulation of biofilm within the void space. A wide accumulation of biofilm within porous media is often observed in lab-scale experiments under ideal growth conditions (excess nutrient supply, and low to moderate flow velocities). The growth may lead to the occurrence of channeling with high shear forces present or a complete clogging of the system (Kim et al. 2010, Pintelon et al. 2012).

(b) surface coverage of biofilm over the porous media. A surface coverage as dominant growth mechanism is tendentially enhanced within porous media with a coarse grain size or a general growth limiting factor (Kim et al. 2010, Tecon and Or 2017).

(c) pore throat coverage of biofilms. The grain-grain contact points may deliver a geometrical advantage for the growth of biofilms (low bridging distance, low shear forces or shelter).

(d) discontinuous coverage of biofilms. A discontinuous coverage may be present if strong heterogeneous conditions prevail (e.g. oxygen, nutrient supply, shear forces, geometrical restrictions) (Carrel et al. 2018).

(e) streamer formation. The formation of streamers is typically observed at high shear forces or turbulent conditions. The streamer formation may represent competitive advantages due to an enhanced mass transfer (Valiei et al. 2012).

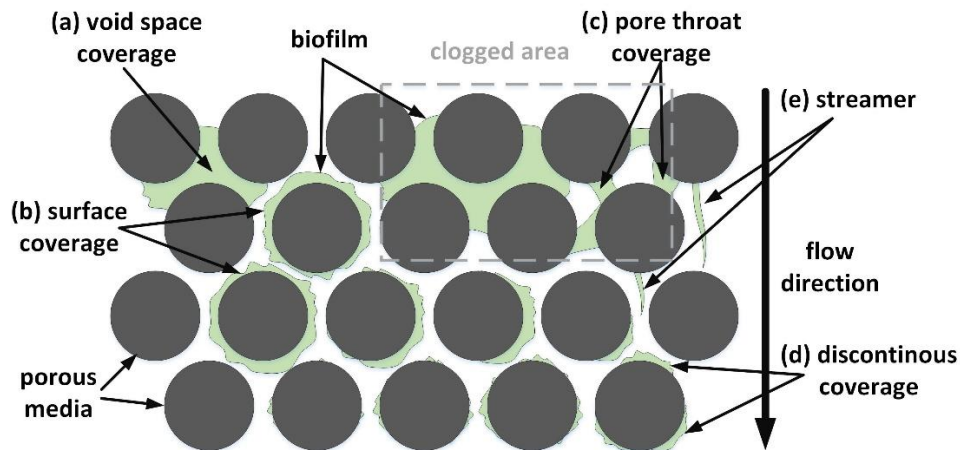


Figure 1-3: Potential ways of biofilm coverage within porous media: (a) void space coverage; (b) surface coverage; (c) pore throat coverage; (d) discontinuous coverage; (e) streamer shaped growth.

Overall, the structure of a biofilm on the mesoscale is largely affected through the flow velocity in terms of mass transfer and shear forces, nutrient and oxygen availability and geometrical conditions of the solid interface biofilms attach on. It should be pointed out that the simultaneous occurrence of several growth mechanisms is likely and may lead to intermediate growth structures. Further, a dominant growth structure may change due to local conditions and during initial stages of biofilm growth.

1.4.2 Aerobic granular sludge

Aerobic granular sludge (AGS) represent a special case. In here, the spherically shaped biofilm itself form a porous media during the settling phase. Within the engineered system, the growth of aerobic granules is favored by anaerobic feeding, high shear stress and withdraw of excess sludge.

Overall the AGS-technology has several competitive advantages over the commonly applied activated sludge process:

- The whole biological treatment can take place within one reactor due to a sequencing batch reactor design. Thus, investment costs for the build up as well as operational costs (pumping costs) can be saved.
- Due to the size and microbial density a higher turnover per volume can be realized. Ongoing is a higher settling velocity of AGS compared to activated sludge. Thus, the settling time can be reduced, leading to shorter process intervals.

- The AGS-technology fulfills advanced treatments as the removal of phosphorous and nitrogen sources can be realized in parallel (Derlon et al. 2016, HaskoningDHV 2020, Wilén et al. 2018).

Structure of aerobic granules

Due to the size of aerobic granules in the range of a few millimeters, different zones within aerobic granules ongoing with varying consortia of microorganisms develop Figure 1-4.

The aerobic zone (outer area) of AGS is supplied with oxygen during the aeration phase. In here, the biological oxidation of organic substances and the nitrification of ammonia take place. Organic substances are typically summarized in form of a parameter that measures the oxygen uptake during the oxidation of organic substances (termed Chemical oxygen demand COD). Through process design the growth of slow growing microorganisms like phosphate accumulating organisms (PAOs) and glycogen accumulating organisms (GAOs) is favored (de Kreuk and Van Loosdrecht 2004). The accumulation of PAO/GAOs has several advantages. PAO/GAOs increase the stability and compactness of AGS (de Kreuk and Van Loosdrecht 2004). Further, PAO/GAOs possess a lower metabolic yield, which lowers the amount of biomass that has to be disposed (Maurer et al. 1997). Especially the growth of PAOs is beneficial as they are able to take up phosphorous from the liquid phase, which improves water quality.

With increasing depth, the oxygen availability becomes lower. The area that is no longer supplied with dissolved oxygen during aerobic phase is called anoxic zone. As dissolved oxygen is not available, microorganisms have to use other electron acceptors as for example nitrate or nitrite (termed NO_x). Generally those microorganisms are called denitrifiers. The purpose of a permanently anoxic zone aligns in the simultaneous denitrification within the anoxic zone combined with a nitrification within the aerobic zone (Derlon et al. 2016). Thus, not only ammonia but also NO_x can be degraded during an aeration phase. Also phosphate and glycogen accumulating organisms are found in the anoxic zone. Due to their ability to perform denitrification, they are called DPAOs/DGAOs.

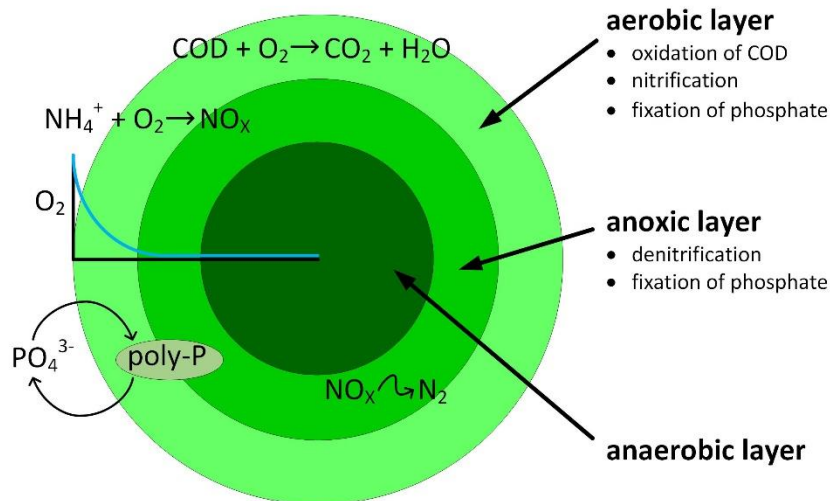


Figure 1-4: Sketch of an aerobic granule. Within the specific zones (aerobic, anoxic and anoxic layer) specific consortia of microorganisms settle and allow for the degradation of carbon, nitrogen and phosphorous sources within one treatment (After Wilén et al. (2018)).

Aerobic granules in sequencing batch reactors

The growth of biofilms in form of AGS is favored by the circumstances realized within sequencing batch reactors. One cycle consists of three phases (Figure 1-5).

During the anaerobic feast phase, the AGS are settled at the bottom of the reactor, where they form a porous medium. Wastewater enters the reactor from the bottom. Simultaneously, water is discharged at the top of the reactor (Figure 1-5a). Typically 50% of the reactor volume is exchanged during one anaerobic feeding phase (Wilén et al. 2018). The anaerobic feeding favors the growth of PAOs and GAOs as they are able to take up easy biological degradable chemical oxygen demand (COD) without the presence of an electron acceptor (de Kreuk and Van Loosdrecht 2004). Slowly biodegradable COD is further metabolized into Polyhydroxyalkanoate (PHAs) that are stored within the cell. The energy is taken from stored glycogen (Maurer et al. 1997). In the case of PAOs the microorganisms are also able to gain energy from the release of phosphorous which is internally stored in form of poly-phosphate (Maurer et al. 1997, Pereira et al. 1996).

Due to the aeration within the following famine phase, the AGS is dispersed over the whole reactor (Figure 1-5b). Heterotrophic microorganisms are able to degrade the remaining COD under now aerobic conditions. Once COD is degraded, microorganisms will degrade ammonia. Even though, the outer areas of aerobic

granules are supplied with oxygen, the inner part remains permanently anoxic. Denitrifying microorganisms take up NO_x as an electron acceptor, thus enabling a simultaneous nitrification/denitrification process (de Kreuk et al. 2005, Pronk et al. 2015b). Under the availability of electron acceptors, GAOs and PAOs metabolize PHAs into glycogen. Especially, PAOs are able to take up phosphorous from the liquid phase and to internally store it as poly-phosphate.

The settling phase is started by turning off aeration. Due to the density difference of aerobic granules and water, the AGS settles down Figure 1-5c. While settling a porous medium out of aerobic granules forms at the bottom of the reactor. In regular intervals, but not at every cycle, excess sludge is taken off from the reactor. Water is discharged with the following anaerobic feeding phase. If NO_x remained in the liquid it will be degraded by denitrifiers, as new easy biodegradable COD is supplied with the next step of anaerobic feeding (Rocktäschel et al. 2013).

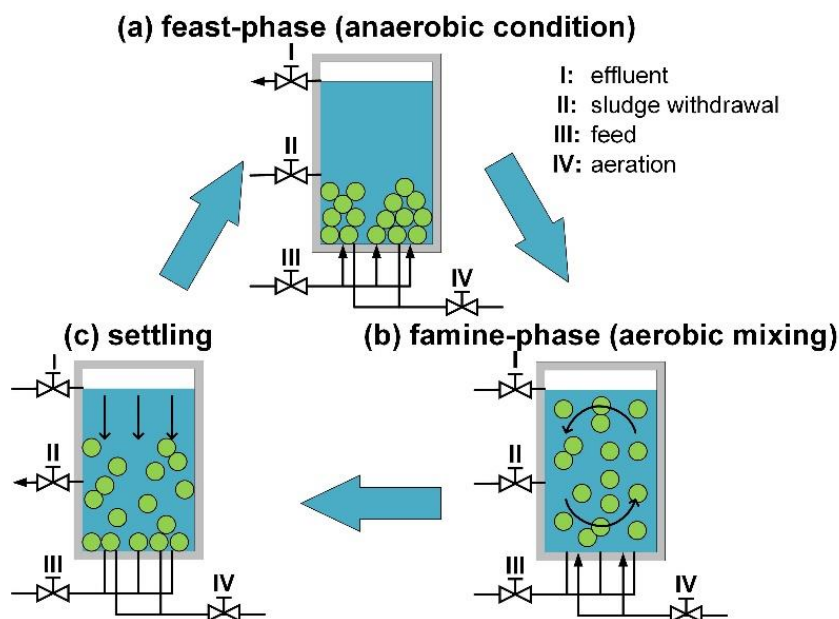


Figure 1-5: Biological treatment via AGS within sequencing batch reactors. Within the feast-phase (a) fresh wastewater enters from the bottom and COD is taken up by anaerobic metabolizing microorganisms. Within the famine-phase (b) the metabolization is taking place under aerobic conditions. During settling (c) the AGS settles at the bottom of the reactor while forming a porous medium after HaskoningDHV (2020).

1.5 Imaging techniques for the visualization of deposition processes within porous media

To dynamically visualize processes within porous media certain requirements are beneficial:

- The possibility to resolve the whole porous media within 3d without depth limitation, which allows to resolve differences within the structure of the porous media and to allocate structure related differences. Hence, UV-VIS light based methods are not considered due to their limited penetration depth.
- A high resolution to resolve processes on the pore scale. Beside the resolution, the grain size of the porous media is of interest.
- Adequate contrast to differentiate between different fractions of the porous media.
- A non-invasive method to avoid impairment of the porous material or microorganisms.

1.5.1 MRI

Background:

MRI is an imaging method based on nuclear magnetic resonance (NMR). The method is selective for isotopes that possess an intrinsic magnetic moment (so called NMR - active nuclei). Once NMR – active nuclei are exposed to a magnetic field, their energy levels split up according to the number of nuclear spin states. For imaging purposes commonly ^1H is used due to its high physical sensitivity and ubiquitous appearance in organic and many inorganic systems. In case of ^1H -NMR, two energy levels exist due to nuclear spin $\frac{1}{2}$ the population of which can be calculated according to the Boltzmann equation. The spin state parallel to the outer magnetic field is energetically slightly preferred resulting in a macroscopic magnetization vector along the direction of the magnetic field. The system is brought into excitation by applying a radio frequency pulse at the Larmor frequency. During excitation, the populations of the energy levels are brought out of thermodynamic equilibrium observable in an alternation of the resulting macroscopic magnetization vector. Ongoing with time, the magnetization returns into the thermodynamic equilibrium, a process named relaxation. Relaxation starts immediately after the excitation. Two main phenomena are known, the longitudinal (T_1 -) and the transversal (T_2 -) relaxation. Both are substance specific and

Chapter 1: Fundamentals

therefore well suited to create image contrast in MRI. Further, a contrast can be enhanced through addition of paramagnetic ions (Paramagnetic relaxation enhancement). A tomograph typically consists of a superconducting magnet, responsible for the magnetic field, which is further homogenized by a shim system. Further, a radiofrequency coil is used for excitation. The same coil can be used for receiving the signal. However, commonly a separate more sensitive receiving coil is preferred. The localization within the sample is achieved by magnetic field gradients. The obtained data points (arranged within the so called k-space), are finally transferred into a cartesian coordinate system by applying a Fast Fourier transformation. Detailed descriptions of MRI are provided in several textbooks (Blumich 2000, Callaghan 1993, Kimmich 2012, Westbrook and Talbot 2018).

Application:

MRI is well suited to study the growth of biofilm within porous media (Neu et al. 2010). Several systems and materials have been used for their growth including porous foams, randomly packed beds or glass columns (Graf von der Schulenburg et al. 2008, Seymour et al. 2004, Wagner et al. 2010). Due to its ability to directly measure flow profiles, MRI was used to investigate alterations in the flow profile aligned with the growth of biofilm (Graf von der Schulenburg et al. 2008, Lewandowski et al. 1992, Manz et al. 2003, Seymour et al. 2004, Wagner et al. 2010). For example, Seymour et al. (2004) showed that anomalous flow distributions develop due to the growth of biofilm within porous media. In addition, the hydrodynamic conditions on the biofilm can be assessed to estimate shear forces and evaluate sloughing events (Wagner et al. 2010). However, quantifying the biofilm might be challenging as water is the by far largest component of the EPS matrix which might cause a slight contrast between biofilm and surrounding bulk phase (Neu et al. 2010). The contrast is potentially influenced by the biofilms properties like compactness, chemical composition, and its binding capacity to water (Herrling et al. 2017, Lewandowski et al. 1992, Seymour et al. 2004). To enhance contrast between water and biofilm, the MRI parameters (Repetition- and Echotime) can be adjusted, or diffusion weighted imaging can be applied (Kirkland 2017, Seymour et al. 2004). Further, the addition of paramagnetic ions represents an alternative. Several studies used the alteration of relaxation due to the accumulation of paramagnetic ions within EPS to study their mass transfer processes. For example, studies have investigated the adsorption of copper, iron, macromolecules, MRI-contrast agents or nanoparticles into the MRI matrix (Bartacek

et al. 2016, Herrling et al. 2017, Phoenix et al. 2008, Ramanan et al. 2013, Ranzinger et al. 2016). In addition, the self-diffusion of water molecules can be measured with NMR. Herrling et al. (2017) highlighted that the self-diffusion within the EPS matrix correlates with its compactness and density. Overall MRI presents many features of interest to study biofilms. Nevertheless, the resolution remains the main drawback of the method. An alternative view is provided when the system is assessed without spatial resolution. Due to the shortening of T_2 -relaxation it is also possible to indicate biofilm growth within packed beds or real soil samples (Hoskins et al. 1999, Kirkland 2017).

Within the field of particle deposition/ filtration mechanisms these features are also helpful. Filtration mechanisms have been observed within randomly packed beds, hollow fibers, flat sheet membranes, or spiral flow membrane modules (Arndt et al. 2017, Bristow et al. 2020, Buetehorn et al. 2011, Schuhmann et al. 2018, Sederman and Gladden 2001). Besides the localizations of depositions, key advantages of NMR/MRI are the ability to measure flow profiles and to investigate the compaction of compressible particle layers aligned with the change of T_2 -relaxation (Adebayo and Bageri 2020, Mikolajczyk et al. 2018).

1.5.2 X-ray computed tomography

Background:

Computer tomography (CT) is based on the diffraction of x-rays. The general set-up consist of a source of x-rays, a sample that is to be imaged, and detectors that convert the incoming x-rays into electronic signals (Kumi et al. 2015, Ritman 2004). For the purpose of 3D visualization either the sample or the scanner (x-ray source and detectors) have to be rotated. Further, the image projection is possible through the filtered back projection which is based on the radon transformation (Hounsfield 1973). The emitted x-rays experience attenuation while passing through the sample. Further, the x-rays interact with the electrons of an atom via absorption or scattering. Therefore, the ratio of attenuation correlates with the atomic number ongoing with the number of electrons. Thus, the atomic number is mainly affecting the contrast between different materials.

Application:

CT finds applications within the field of biofilm growth as well as particle deposition. The visualization of biofilms demands for the addition of contrast agents (Carrel et al. 2017, Iltis et al. 2011, Peszynska et al. 2016). A differentiation was possible by using small particles that enhance the attenuation within the liquid phase (Iltis et al. 2011). Further, the addition of iron was evaluated. However, the incorporation of iron within the EPS matrix showed to be not sufficient to allow for a differentiation of fractions (Carrel et al. 2017). Therefore, Carrel et al. (2017) applied a high iron sulfate concentration to enhance the attenuation of the liquid phase. In regard of harmful radiation it is uncertain how microbial growth is affected under permanent exposure (Peszynska et al. 2016). To the author's knowledge, no complete cultivation was performed within a CT-scanner. Commonly, samples were imaged before the inoculation and at the end of the cultivation. Overall, micro computed tomography allows for a higher spatial resolution than MRI. Therefore it has been used to couple structural findings with growth models (Carrel et al. 2018, Peszynska et al. 2016). Besides simulation, studies combined CT images with MRI to reveal flow profiles (Mikolajczyk et al. 2018). An alternative method represents three-dimensional particle tracking velocimetry based on tracing of neutrally buoyant fluorescent tracer particles and illumination from a monochromatic light source (Carrel et al. 2018, Holzner et al. 2015). However, as the approach is light based, the porous media has to be transparent.

As harmful radiation is not restrictive for most filtration processes more studies can be found within this area. Studies observed the particle depositions/accumulation in terms of deep bed and surface filtration (Al-Abduwani et al. 2005, Chen et al. 2008, Gaillard et al. 2007, Godinho et al. 2019, Mikolajczyk et al. 2018). In here, flow induced drilling events within filter cakes and redistributions within the porous media were observed. In addition, the coupling with simulations and MRI was undertaken to delineate flow profiles (Chen et al. 2010, Mikolajczyk et al. 2018). Besides a high spatial resolution, time-lapse imaging with a sampling frequency in less a second is possible (Godinho et al. 2019). Thus, Godinho et al. (2019) were able to closely monitor failures within filter cake formation.

1.5.3 Neutron computed tomography

Background:

The usage of neutrons for imaging purposes represents a complementary method to x-rays. Similar to x-ray computed tomography, the set-up consists of a neutron source, a sample that is to be imaged, a detector that converts the signal, and a rotating component (either sample or source and detectors) (Lani and Zboray 2020, Strobl et al. 2009). Due to the zero net charge, neutrons strongly interact with the atomic nucleus. A strong attenuation can be found for light elements (mainly hydrogen). Further, it is also possible to differentiate between isotopes. Only poor attenuation is observed for many metals. Therefore, metal containers up to several centimeters thick can be penetrated by neutrons (Lani and Zboray 2020, Strobl et al. 2009).

Application:

Neutron computed tomography presents an alternative method. However, the availability of neutron sources is limited and thus, the method is only applied at some specialized facilities worldwide (Strobl et al. 2009). The method is of interest as it allows for a complementary perspective to μ -CT, especially in terms of contrast generation. By now, some fundamental works revealed its potential for particle deposition in packed beds and biofilm growth within soils (Bianchi et al. 2018, Selamet et al. 2013, Zheng et al. 2018). Especially the high resolution in combination with good contrast between air and liquid allows to observe processes at partially saturated conditions (Zheng et al. 2018).

2 Investigation of Biofilm Growth within a Monodisperse Porous Medium under Fluctuating Water Level Assessed by Means of MRI (Published in MDPI Water)

2.1 Introduction

Microorganisms can be found in natural, as well as engineered, partially saturated systems. Examples include the vadose zone, irrigated agriculture, and aerated biofilters. As a crucial part of the ecosystem, microorganisms are involved in the utilization of carbon sources, guaranteeing water quality, the removal of pollutants, the promotion of plant growth, and the regulation of greenhouse gas emissions within natural soils (Brussaard 2012, Tecon and Or 2017). Their abundance and activity vary depending on the physical environment. Fluctuations in temperature, water, and nutrient availability, combined with geometrical restrictions, require microorganisms to be highly adaptable (Or et al. 2007a, Tecon and Or 2017). A common response of microorganisms to stressful conditions, such as fluctuating water levels, is the production of extracellular polymeric substances (EPSs) and surface attachments, which lead to the formation of biofilms (Flemming and Wingender 2010).

Due to the often non-negligible amount of biofilm that covers the void space, alterations in the hydraulic properties of the porous medium occur. Possible reasons for this include: (I) structural changes via pore size accumulation, (II) the high water-holding capacity of EPS matrices, (III) changes in soil wettability due to surface coverage, and (IV) alterations in the water–air–surface tension (Or et al. 2007a, Zheng et al. 2018).

It has been commonly reported that the EPS matrices of biofilms increase water retention and reduce evaporation, as well as saturated and unsaturated hydraulic conductivity (Bozorg et al. 2015, Roberson and Firestone 1992, Volk et al. 2016, Zheng et al. 2018). Despite these observations, the role of the fragmentation of residual water is relevant for diffusive transport processes on many scales. At low water contents, EPS are associated with the dispersion of nutrients by bridging between isolated water clusters, leading to an enhanced liquid phase connectivity (Or et al. 2007b, Roberson and Firestone 1992, Tecon and Or 2017). However, experimental studies on the impact of EPS accumulation on transport processes within partially saturated porous media

are rare. One such study was conducted by Chenu and Roberson (1996), who addressed this field by conducting diffusion experiments. An alternative approach is the direct visualization via suitable imaging methods.

The interplay of biofilms, porous media, and hydraulic properties has mainly been assessed in completely saturated conditions. The imaging methods of choice include X-ray microtomography (Carrel et al. 2018, Iltis et al. 2011, Peszynska et al. 2016), neutron-radiography (Zheng et al. 2018), magnetic resonance imaging (MRI) (Graf von der Schulenburg et al. 2008, Metzger et al. 2006, Seymour et al. 2004, Vogt et al. 2013), and optical methods on porous microfluidic channels (Bozorg et al. 2015, Karimifard et al. 2021, Sharp et al. 2005, Valiei et al. 2012). The field of biofilm growth within partially saturated porous media is almost unexplored.

The more stringent requirements associated with imaging partially saturated porous media might be the cause of this. We propose that an ideal method requires: (I) a sufficient resolution to accurately resolve the pore spaces, (II) no depth limitation to the three-dimensional visualization of the entire porous medium, (III) adequate contrast to differentiate the phases (e.g., water, biofilm, air, and solid material), and (IV) noninvasiveness of the method in order to avoid the impairment of the porous material or microorganisms. As none of the aforementioned imaging methods fulfill all requirements, compromises have to be made.

The current study aimed at highlighting MRI as a suitable tool to visualize biofilm accumulation within unsaturated porous media. MRI has the benefits of being an *in-situ*, noninvasive method that is not limited in penetration depth. A bed of randomly packed glass spheres with sizes of 2 ± 0.1 mm were chosen as a porous medium to allow for pore-scale visualization. In a previous study, the initial water retention of a packed bed of 2 mm glass spheres showed the most homogeneous dispersion of free water, mostly between pore throats (Ranzinger et al. 2020a). The hypothesis of this study was that a homogeneous distribution of free water would deliver rather equal starting points for biofilm growth.

The focus of this study was to: (I) visualize all fractions within the porous medium (water, air, particles, and biofilm) in a time-resolved manner, (II) identify preferential spots of biofilm development and accumulation within the porous medium, and (III) characterize ongoing changes within the liquid phase in the form of quantity and connectivity.

2.2 Materials and Methods

2.2.1 Experimental Setup and Procedure

A schematic of the experimental setup is depicted in Figure 2-1. The 2 mm glass spheres were placed inside a glass column with an inner diameter of 14 mm and a length of 100 mm. An O-ring and a piece of mesh (size 0.7 mm fabric) were positioned at the lower part to avoid the blockage of the inlet. The height of the packed bed of glass spheres was approximately 90 mm. The field of view was positioned at the middle of the glass column and covered 22.5 mm along the height of the glass column. The glass column was installed inside a 200 MHz magnetic resonance tomograph (Bruker BioSpin GmbH, Rheinstetten). The cultivation setup was an open system that was connected using the tube lines. Drainage/flushing events were conducted in alternating order by temporarily switching the peristaltic pumps on and off. Furthermore, turning off the peristaltic pumps sealed the corresponding tube line. Thus, the integration of valves was avoided. Flushing is depicted in Figure 2-1a. Here, a peristaltic pump sucked water from the feed solution. Once the sample was filled with water, the pump circulated water until the end of the flushing sequence. The drainage of the sample (Figure 2-1b) was conducted by one peristaltic pump pushing air through the sample. Gas breakthrough was recognizable at the outlet once the sample was drained. The drainage/flushing sequence lasted 30 min in total. Approximately 15 min was needed to fill/drain the sample entirely, followed by 15 min of mixing to ensure a homogenous nutrient distribution within the porous medium (Figure 2-1c). In between the drainage/flushing sequence, a break of 30 min was applied. Breaks were used for image acquisition. For 3D images, the time for image acquisition was elongated to 1 h once per day.

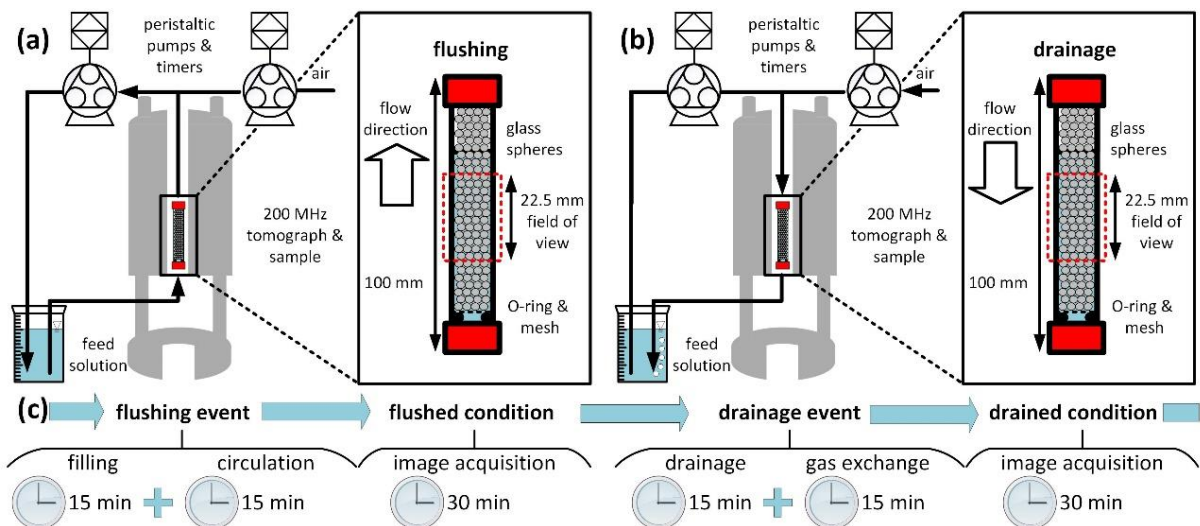


Figure 2-1: Experimental setup of the MRI experiments. Flushing (a) and drainage (b) events were conducted in alternating order. The timing of work flows is highlighted in (c). In the flushed and drained conditions, both pumps were turned off to acquire images in a static state.

2.2.2 Cultivation

The sample was inoculated with *Bacillus subtilis* precultures grown at 37 °C overnight in Luria broth (LB) medium. Twenty milliliters of preculture was added to the feed solution at the beginning of the experiment. *Bacillus subtilis* was chosen as it is abundant in natural soils and able to incorporate iron within the EPS matrix. The feed solution consisted of 1 L of tap water enriched with 1 g/L of acetate (originating from sodium acetate) and 2 mg/L of Fe³⁺ (originating from iron(III)chloride) as a contrast agent for the growing biofilm. The tap water of Karlsruhe contained the following concentrations of ions (mg/L): Ca (112), Na (11), Mg (9.7), Si (5.4), K (1.7), P (<0.01), Fe (<0.01), and Mn (<0.005). More information on constituents is accessible from the homepage of the Stadtwerke Karlsruhe website (<https://www.stadtwerke-karlsruhe.de>) (accessed on 9/11/2020). At day 6, the sample was positioned within the MRI and further monitored over a period of 7 days, resulting in an experiment period of 12 days. The timing of the drainage and flushing events was kept constant over the whole experiment, as described in the previous section.

The relevant cultivation period for the MRI measurements was based on a preliminary experiment. Here, samples were cultivated under permanently saturated conditions to additionally assess the growth by means of optical coherence tomography (OCT). A detailed description of the cultivation is provided in Appendix 2-1. Only the OCT data of the preliminary experiment are shown in the present study.

2.2.3 Optical Coherence Tomography (OCT)

A spectral domain tomograph (GANYMEDE I, Thorlabs GmbH Dachau, Germany) was applied to monitor the biofilm growth on the glass spheres. B-scans were obtained with a resolution of $2.1 \mu\text{m} \times 8 \mu\text{m}$ (x- by -z) in water ($n = 133$) and an A-scan average of 4. Detailed information on the working principle and applications in biofilm research are provided in Wagner and Horn (2017).

In the current study, the acquisition of C-Scans was limited because of the curvature of the glass columns. Furthermore, optical refractions interfered when measuring the biofilm in partially saturated conditions. Therefore, the measurements were feasible only with constantly saturated probes. The conditions and setup for the cultivation under permanently saturated conditions are described in Appendix 2-1.

2.2.4 Magnetic Resonance Imaging (MRI)

MRI experiments were conducted within a 200 MHz super-wide bore magnet equipped with an Avance HDIII console (Bruker BioSpin GmbH, Rheinstetten, Germany). The probe was an MICWB 40 with a 20 mm birdcage. For imaging, gradients of up to 1.5 T/m were available. The multi-slice–multi-echo (MSME) pulse sequence was chosen. The parameters of the MRI experiments are listed in Table 1. Different parameters were chosen for 2D and 3D measurements. The parameters were kept constant over the whole experimental period and no changes in acquisition parameters were conducted between drained and flushed conditions.

Table 2-1: Acquisition parameters of MRI experiments.

	MSME 2D	MSME 3D
repetition time [sec]	1.5	0.5
echo time [sec]	0.01	0.01
field of view (x, y, z) [mm × mm × mm]	16 × 24 (6 slices in y-direction)	15 × 15 × 24
matrix size (x, y, z)	128 × 6 × 192	64 × 64 × 128
voxel size (x, y, z) [$\mu\text{m} \times \mu\text{m} \times \mu\text{m}$]	125 × 125 (200 μm slice thickness in y-direction)	234 × 234 × 188
number of averages [-]	4	1
measurement time [min:sec]	12:48	34:08

2.2.5 Image Analysis

The image analysis was performed by using Avizo 2021.1 (Thermo Fisher Scientific, Waltham, MA, USA) and self-written scripts in Matlab R2018b (Math-Works, Natick, MA, USA). For the 3D image analysis, the exterior material was used for noise adjustment and removed from the dataset. The binary images were obtained by setting a threshold at 3000 out of 2^{15} intensity values. The first image, taken on day 6 in flushed condition, served as a reference. Here, the threshold separated the water-filled void space from glass spheres (solid material). For visualization purposes, the glass spheres were superpositioned onto the other images.

For each measurement, the water content was quantified by keeping the threshold value constant at 3000. After that, clusters of the liquid phase, as well as enclosed cavities smaller than 10 voxels, were removed.

Furthermore, the connectivity function defined liquid clusters by using a neighborhood connectivity of 26 in a 3D matrix. For the connectivity analysis, the specific Euler number χ_V , as suggested by Vogel and Roth (2001), was calculated according to:

$$\chi_V = \frac{N-C+H}{V} [\text{mm}^{-3}] \quad (\text{eq.2-1})$$

where the number of isolated objects is N , the number of redundant connections is C , the number of completely enclosed cavities is H , and the volume of the sample is V .

2.3 Results

2.3.1 Dynamics of Water Content

Figure 2-2 shows 2D images taken on days 6, 9, and 12. The upper row (a) shows the sample in the flushed condition, while the lower row (b) displays the sample in the drained condition. To enhance readability, the following statements refer to four regions of interest (ROI) that are highlighted in Figure 2-2.

MRI obtains a signal from water molecules. Therefore, water-containing voids deliver a signal that is typically indicated in grey (Figure 2-2a). Regions indicated in white are the result of susceptibility artifacts, which appear close to the interface between different fractions. These are observed at the interface between the glass spheres and water or between entrapped air and water. However, the local entrapment of air may vary with the time and cycle. In addition, the occurrence of susceptibility artifacts can be aligned with the entrapment of small air bubbles. The glass spheres, the entrapped air, and the exterior components do not contribute to the signal and appear black. In Figure 2-2a, the void space is almost completely filled with water.

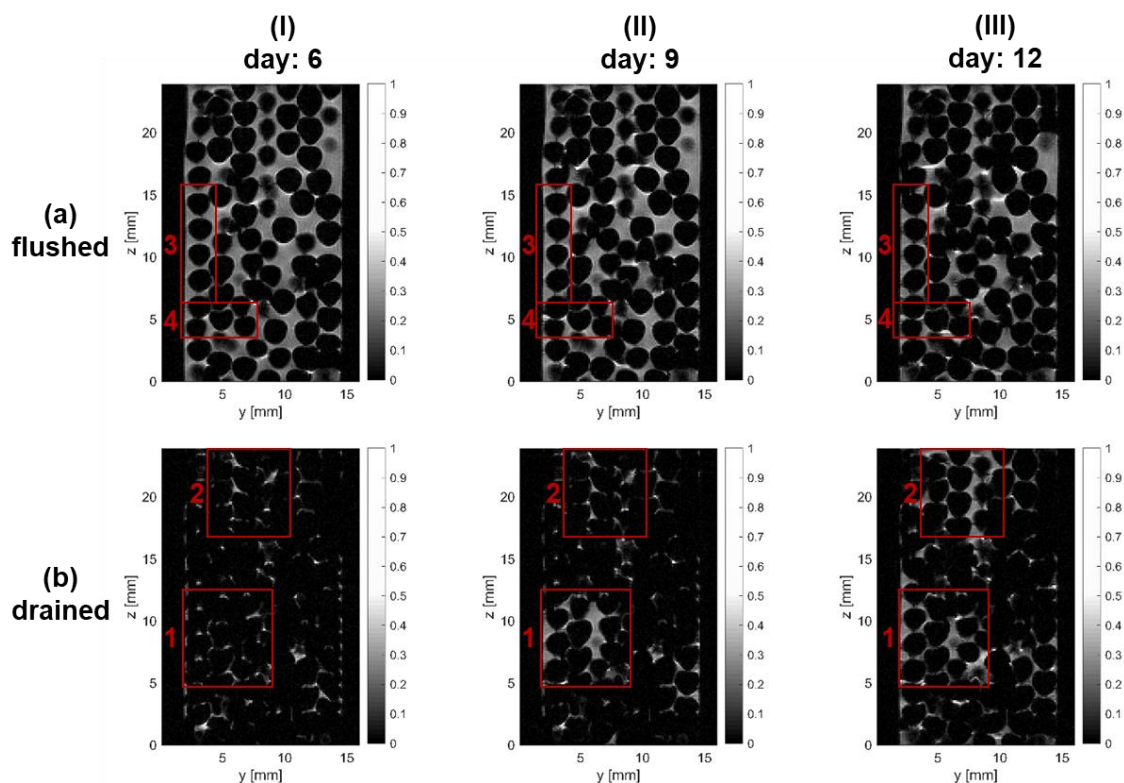


Figure 2-2: Two-dimensional MRI images displaying the normalized signal intensity in the flushed (a) and drained (b) conditions on days 6, 9, and 12. (a) Biofilm growth can be recognized in the form of dark regions appearing next to contact points of glass spheres. For further clarification, view the [highlighted animation](#). (b) Water retention increases within the porous medium due to the growth of biofilm. Regions of interest (ROIs) that reveal occurring changes are highlighted in red.

After the drainage of the sample, most of the void space was filled with air and delivered no signal (Figure 2-2bl). Water could still be found in pore throats between particles or between particles and the column wall (Figure 2-2bl; ROI 1). Only a few pores retained larger amounts of water. A relatively high amount of water retained in pores can be seen in Figure 2-2bl; ROI 2.

At day 9, more water was retained within the porous medium (Figure 2-2bll). The area of ROI 1 retained water almost completely on day 9, whereas changes in ROI 2 were not significant. At day 12, ROI 2 also retained relatively high amounts of water. Both ROIs 1 and 2 retained larger amounts of water than the rest of the porous medium, indicating a heterogeneity in the water retention.

Overall, the water content in the flushed condition did not significantly alter (Figure 2-1all and alll). However, the entrapment of air was locally recognized and is further indicated in the [animated version](#).

2.3.2 Biofilm Growth

The growth of biofilm appeared as dark regions between glass spheres or between glass spheres and the column wall (Figure 2-2). For example, a cross-comparison of ROI 1 over days 6, 9, and 12 highlights the developing pore throat coverage of the biofilm along z (compare Figure 2-2, row a, ROI 3). For clarification, the authors encourage viewing the animation provided in the Supplementary Materials ([animated version](#)). Two locations of biofilm growth were identified in the sample: biofilm accumulated in pore throats, either between two particles or between a particle and a column wall (compare Figure 2-2, row a, ROI 3); additionally, a biofilm coverage of pores was punctually observed (compare Figure 2-2, row a, ROI 4). The biofilm can also be recognized in the drained condition on days 9 and 12 (see Figure 2-2, row b, ROI 1).

Optical coherence tomography (OCT) images (B-scan; xz-plane) provide a closer look at the biofilm situated on the glass spheres next to the column wall (Figure 2-3). Furthermore, they highlight which stages of biofilm growth were accessible by means of MRI. Data were provided from a separate experiment conducted under entirely saturated conditions. On day 0 (before inoculation), the smooth surfaces of three glass spheres were visible (Figure 2-3a). On day 6, small biofilm colonies situated on the surface of the glass spheres were recognized (Figure 2-3b); in addition, the inner edge of the glass wall, recognizable as a curvilinear line, became visible. After 14 days, the

biofilm had grown between the glass wall and the particle surface (Figure 2-3c). The biofilm structure was fluffy. Additionally, cavities were found within the mesoscopic biofilm matrix. Overall, more biofilm was recognized between the glass column and the spheres than at the contact points between the glass spheres (Figure 2-3c). However, from the MRI perspective, only the former case, where a distinct biofilm covered the voids between particles and the column wall, was accessible due to the resolution.

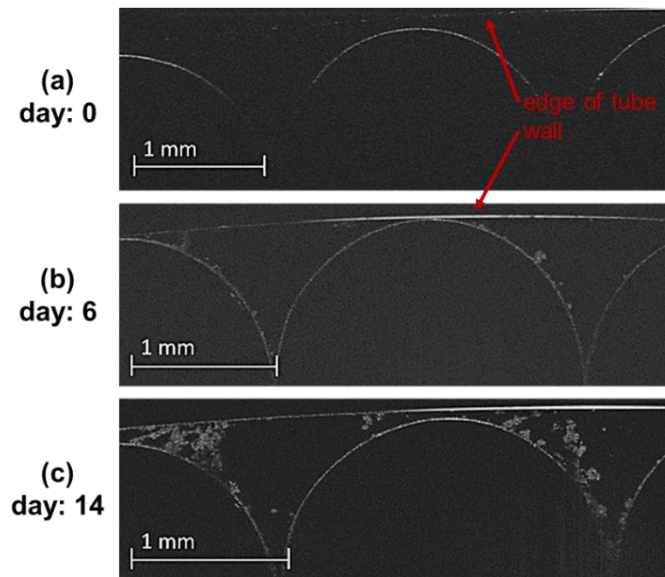


Figure 2-3: OCT B-Scans acquired from a previous experiment under permanently saturated conditions. (a) Three glass spheres before inoculation. (b) After 6 days, biofilm could be found on the particle surface in the form of small colonies. (c) Biofilm covered the voids between the particles and the column wall after 14 days. A biofilm as distinct as in (c) was accessible by means of MRI.

2.3.3 Analysis of Liquid Phase

Figure 2-4 shows processed 3D MRI datasets. For the sake of clarification, the glass spheres and column wall have been superpositioned in the 3D rendering. The distinction between the void space and glass spheres was performed based on Figure 2-4aI. The air is visualized as transparent regions.

An increase in the air entrapment was found at days 9 and 12 (compare Figure 2-4, row a). The increase in water retention after drainage is shown in Figure 2-4, row b. On day 6, most of the water was found close to contact points, while only a few pores were completely filled with water (Figure 2-4bI). The cluster visualization of the liquid phase (Figure 2-4cI) shows many isolated clusters (i.e., many clusters with different colors).

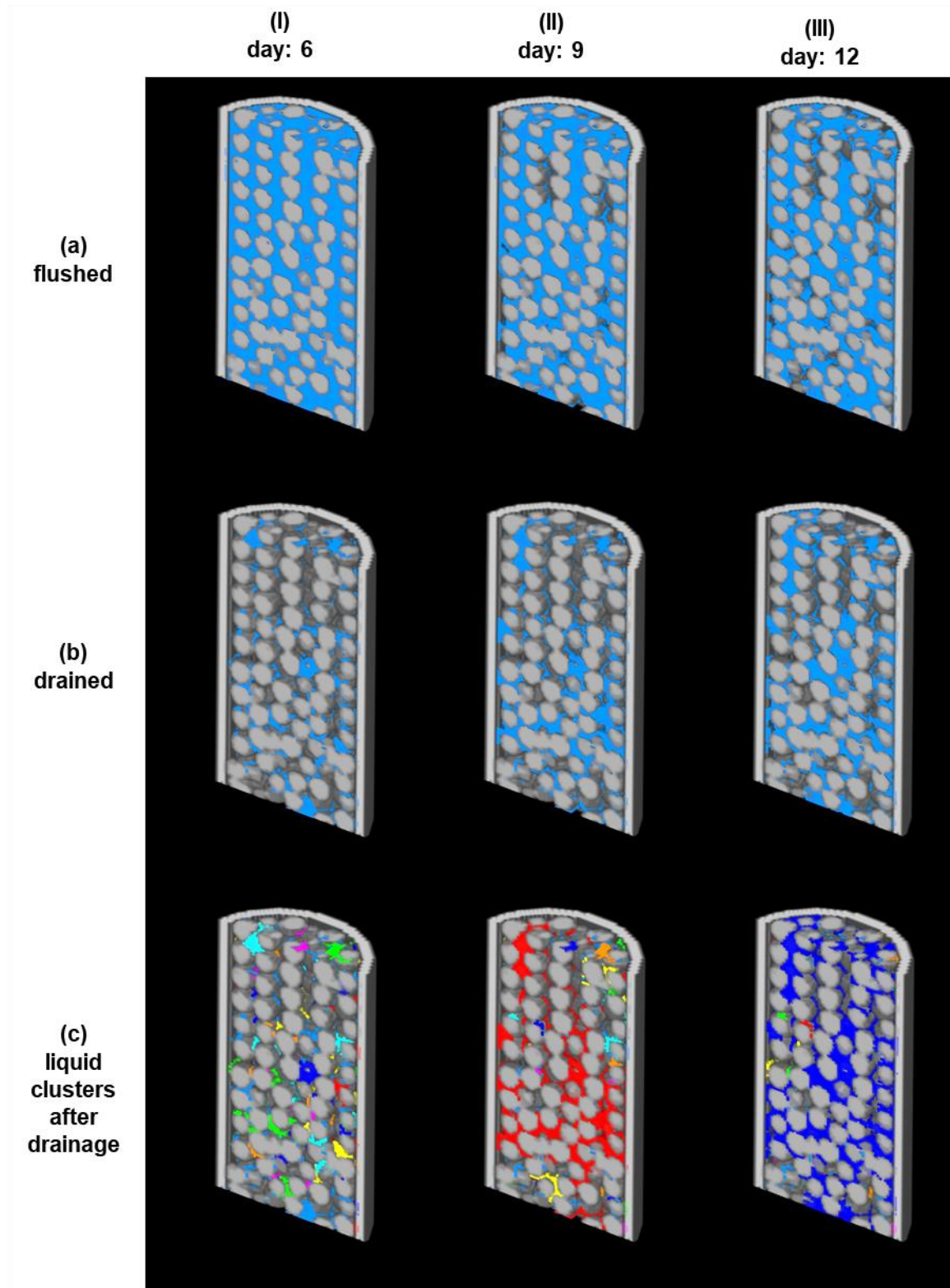


Figure 2-4: Processed 3D images on days 6, 9, and 12 (a) in the flushed condition, (b) in the drained condition, and (c) analyzed for liquid clusters. Solid material (glass column; porous medium) is superpositioned and displayed in grey. The liquid phase is presented in blue. Air is removed from the visualization (transparent areas). Based on row b, the liquid phase was analyzed for connectivity and divided into isolated liquid clusters. Each color represents a separate liquid cluster. Please note that more liquid clusters than colors are shown in (c); therefore, one color might also represent multiple isolated liquid clusters.

Chapter 2: Biofilm growth under fluctuating water level

On day 9, the enhanced water retention led to the formation of a dominant cluster (red) (Figure 2-4cII). The cluster partly covered the width and reached from the top to the bottom of the dataset (Figure 2-4cII). On day 12, almost the complete liquid phase was covered by one cluster (dark blue) (Figure 2-4cIII). Figure 2-5a displays the total water volume over time in under drained and flushed conditions, respectively. In addition, the largest cluster in the flushed condition is shown. The percentages below are in relation to the water content on day 6 after flushing.

The water content in the flushed condition successively decreased from 100% to 72.6% (1236 to 897 mm³) (Figure 2-5a). The water retention in the drained condition increased from 16.7% to 42.6% (206 to 526 mm³) over the duration of the experiment. At the same time, the volume of the largest cluster increased from 1.8% to 38.8% (22 to 479 mm³). Furthermore, the largest cluster covered 11% of the total retained water at day 6, but 91% on day 12. In addition, the volumetric Euler number confirms that the connectivity increased (Figure 2-5b). The volumetric Euler number was below 0 at the beginning of the experiment. This can be explained by the often ring-like shape of the retained water along the pore throats between two particles or between a particle and the column wall (Appendix 2-2), which contributes a value of 0 to the volumetric Euler number (see Equation 2-1). Furthermore, the presence of a few larger clusters with more redundant connectivity led to an overall slightly negative Euler number. Over the experimental period, the volumetric Euler number further dropped, indicating a higher connectivity. The drop in the Euler number can be explained by the creation of more redundant connections due to an increase in the water content and the aggregation of liquid clusters (evidenced by the decrease in the total number of clusters) (Figure 5b). The measurement in the drained condition on day 8 conspicuously does not fit the trends observed.

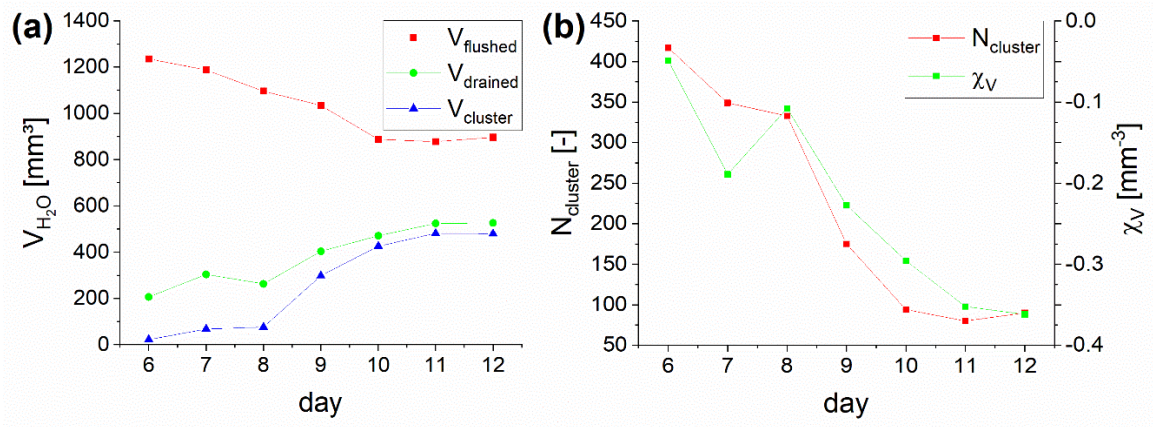


Figure 2-5: Quantification of water content (a) and the total amount of liquid clusters $N_{cluster}$, as well as the volumetric Euler number χ_V (b) over time. Water content decreased in the flushed condition, while water retention in the drained condition increased. Furthermore, the connectivity of the liquid phase in the flushed condition increased, as indicated by the volume of the largest cluster (a) and the volumetric Euler number (b).

2.4 Discussion

2.4.1 Applicability of the MRI Approach

The current study showed the applicability of MRI as a noninvasive and non-depth-limited method for visualizing the four fractions of a porous medium (water, air, particle, and biofilm). A compromise has to be made regarding the resolution, as the resolution hampers the quantification of the biofilm. An increase in resolution is possible when considering a smaller sample diameter, higher magnetic field strength, and a higher number of replications for averaging. For example, Caizán-Juanarena et al. (2019) achieved a resolution of $30\ \mu\text{m} \times 30\ \mu\text{m} \times 30\ \mu\text{m}$ on granular bioanodes when using MRI.

An advantage of the method is that only small amounts of contrast agents are necessary. As reported in previous MRI studies, paramagnetic ions can enhance the contrast between the biofilm and liquid phase (Graf von der Schulenburg et al. 2008, Nott et al. 2001, Ranzinger et al. 2016, Seymour et al. 2004). Furthermore, the addition of low iron dosages has been reported to promote biofilm formation (Hu et al. 2016, O'Toole and Kolter 1998, Peulen and Wilkinson 2011).

2.4.2 Biofilm Growth under Fluctuating Water Level

In the literature, complex biofilm morphologies have been reported in saturated porous media. In general, these can be described as the surface coverage of particles, cluster-like biofilm structures filling complete voids (Peszynska et al. 2016), and biofilm colonies growing as streamers between pore throats (Valiei et al. 2012), as well as intermediate structures (Carrel et al. 2018). In saturated porous media, restrictive nutrient and oxygen supply, as well as local shear rates, must be considered (Carrel et al. 2018, Rittmann 1993, Rockhold et al. 2002). The availability of water becomes an additional restriction in partially saturated porous media (Or et al. 2007a, Tecon and Or 2017). In the present study, preferential spots for biofilm growth were found mainly between the pore throats of two particles or between a glass sphere and the column wall. Biofilm clusters filling voids were observed to a lesser extent. No distinct biofilm was recognizable at the glass sphere surface. However, this outcome does not mean that no biofilm grew on the glass sphere surface. As the pore throats retained water in the form of pendular rings, these regions were identified as preferential spots for biofilm growth. Similar web-like structures of EPS that connect single particles were identified in real soil samples (Chenu 1993, Tecon and Or 2017).

Compared to most studies, the size of the glass spheres and the resulting void space in our study were larger. This may have influenced the extent of biofilm growth. The biofilm in our study had to grow larger to achieve bridging between particles or to cover whole voids, which also affected its resistance to hydrodynamic conditions (i.e., shear) or other physical constraints. Within randomly packed beds of a smaller particle size, the coverage of whole voids might become more pronounced.

2.4.3 Impact of Biofilm on the Liquid Phase

In accordance with the literature, it was shown that biofilm enhances water retention (Bozorg et al. 2015, Volk et al. 2016, Zheng et al. 2018). Potential ways biofilm may affect water-holding properties include: (I) structural changes via pore size accumulation, (II) the high water-holding capacity of the EPS matrix, (III) changes in soil wettability due to surface coverage, and (IV) the alteration of water–air–surface tension (Or et al. 2007b, Zheng et al. 2018). With the present imaging approach, phenomena could be directly assessed and visualized. The usage of a randomly packed bed consisting of monodisperse 2 mm glass spheres revealed structural changes due to the blockage of pore throats. Thus, the entrapment of water above the pore throats played the most dominant role. In addition, the entrapment of air also increased when flushing the sample. Certainly, the usage of smaller particles and the application of lower matrix potentials would drastically reduce the amount of water entrapped above bioclogged throats.

However, Tecon and Or (2017) pointed out that the connectivity of the liquid phase is relevant for transport processes on all scales. As a result of the increased connectivity due to the aggregation within one continuous top-to-bottom liquid cluster, the transport processes may have been enhanced in partially saturated conditions. Nevertheless, in completely saturated conditions, the biofilm at the pore throats would hamper transport processes. Overall, this is in agreement with the findings of Chenu and Roberson (1996), who achieved a faster diffusion of glucose through artificial EPS-amended clay compared to pure clay for various matrix potentials.

2.5 Conclusions

- MRI was a suitable analytical tool for visualizing the growth of biofilm within a partially saturated porous medium. This approach allowed us to differentiate and quantify the liquid, gaseous, and solid phases after flushing and drainage events. In addition, the biofilm fraction could be visualized but not quantified in the current state.
- The biofilm grew preferentially in pore throats that remained permanently wetted in the flushed and drained conditions. Biofilm also filled voids to a lesser extent. The biofilm did not grow distinctly enough to be recognized on the free surface of glass spheres by means of MRI.
- As a result of the usage of coarse monodisperse 2 mm glass spheres, the blocking of pore throats by biofilm was determined as the dominant water retention mechanism. With the ongoing biofilm accumulation, most of the water was entrapped above the bioclogged throats. In addition, a higher entrapment of air was found when flushing the sample.
- Ongoing biofilm accumulation led to an increase in the connectivity of the liquid phase. Therefore, the transport of nutrients may potentially be enhanced in partially saturated systems. However, in completely saturated conditions the blocking of throats by biofilms would hamper transport processes.

3 Transport and retention of artificial and real wastewater particles inside a bed of settled aerobic granular sludge assessed applying magnetic resonance imaging (Published in Water Research X)

3.1 Introduction

Within the last decade aerobic granular sludge systems for municipal wastewater treatment have proved to be economically competitive compared to the activated sludge systems (Giesen et al. 2013, Pronk et al. 2015b). By now, around 50 aerobic granular sludge reactors have been set into operation in full scale for the treatment of wastewater (HaskoningDHV 2020, Li et al. 2014). Despite these full scale plants only little is known about the granulation process during municipal wastewater treatment as well as the factors causing low or high effluent concentrations of particulate organic matter (Derlon et al. 2016, Rocktäschel et al. 2015, Wagner et al. 2015, Wilén et al. 2018).

Around 50 % of the chemical oxygen demand in municipal wastewater are dedicated to particulate organic matter. The latter represents a crucial carbon source in municipal wastewater treatment (Orhon and Çokgör 1997). Particulate organic matter has to undergo hydrolysis before it can be metabolized to carbon dioxide and new biomass by the microorganisms. The removal of particulate organic matter can be divided into 4 steps: (I) external transport to the biofilm surface, (II) attachment of the particles, (III) hydrolysis of particulate organic matter and release of hydrolytic products, (IV) uptake of these products by microorganisms (Boltz and Motta 2007, Li et al. 2018). Theories about the removal of particulate organic matter in granular sludge reactors typically assume that it attaches/adsorbs at the granule surface during the feeding phase (De Kreuk et al. 2010, Pronk et al. 2015a). Overall, the degradation of particulate organic matter takes several days (Benneouala et al. 2017). Thus, attachment is a prerequisite to ensure that particulate organic matter can serve as a carbon source for aerobic granular sludge systems and is not washed out with the effluent. To understand how particulate organic matter behaves within a bed of settled granules during anaerobic feeding, imaging techniques might be applied. Imaging techniques such as confocal

laser scanning microscopy (CLSM), optical coherence tomography (OCT), and micro-computer tomography (μ -CT) are either limited by their penetration depth or by exposing microorganisms to potentially harmful radiation (Adav et al. 2008, Bouma 2001, Li et al. 2018, Peszynska et al. 2016). Magnetic Resonance Imaging (MRI) is a powerful and widely applied tool in biofilm research (Herrling et al. 2019, Neu et al. 2010). MRI is a non-destructive *in-situ* method with a spatial resolution down to some tens of μm . MRI offers the spatial investigation of the distribution of NMR active nuclei (commonly ^1H), relaxation times, diffusional and advective transport. An image contrast between water and biofilm is generated by their difference in the so-called longitudinal (T_1) and transverse (T_2) relaxation times (Manz et al. 2003, Seymour et al. 2004). The image contrast depends on the biofilm properties, i.e., its compactness and chemical composition. So far, MRI studies mainly focused on water diffusion and distribution in biofilms, transport and fate of heavy metals, trace metals, macromolecular substances and nanoparticles (Bartacek et al. 2016, Herrling et al. 2017, Phoenix et al. 2008, Ramanan et al. 2013, Ranzinger et al. 2016). In addition, MRI can be applied to resolve the dynamics of the water distribution and structure of the biofilm. Several studies explored biofilm development, its impact on fluid flow, biomass distribution and shape as well as cohesive and adhesive strength in tube reactors or porous media (Graf von der Schulenburg et al. 2008, Manz et al. 2003, Seymour et al. 2004, Wagner et al. 2010).

The current study aims at exploiting the capabilities of MRI in order to assess the fate of particulate organic matter during the anaerobic feeding phase of a granular sludge bed. To our knowledge, mass transport studies have been limited to single granules and/or did not resolve an entire granular sludge bed. The main objectives of this study were thus: (I) to demonstrate the feasibility and applicability of MRI for the (structural) characterization of granular sludge beds, (II) to investigate the transport, loading and retention behavior of particulate organic matter within a bed of settled aerobic granules and (III) to demonstrate the dependence of the retention mechanism on the size of particulate organic matter. Super paramagnetic iron oxide nanoparticles (SPIONs, $d_p = 38 \pm 10 \text{ nm}$) have been applied which resemble the colloidal fraction of particulate organic matter. The results are supplemented by the investigation of artificial microcrystalline cellulose particles (MCPs, $d_p = 1 - 20 \mu\text{m}$) and real wastewater particles (WWPs, $d_p = 28 - 100 \mu\text{m}$) as models for particulate organic matter in the micrometer range.

3.2 Material and Methods

3.2.1 Aerobic granular sludge

Aerobic granular sludge was taken from a lab-scale sequencing batch reactor (SBR) at Eawag. Samples were sieved to separate flocs from aerobic granules ($d \geq 0.63\text{mm}$). The granule size allowed for a sufficient resolution of the voids between the granules. The granules had a smooth surface and a typical size range of 1 to 2 mm. Granules were sent from Eawag (Dübendorf, Switzerland) to Karlsruhe (Germany): Approx. 200 mL of granules were filled in a bottle and filled up to the top with water. The glass was placed in a styrofoam box together with ice, to keep the samples cooled. The maximum delivery time was 2 days. Samples were stored in a fridge immediately after delivery. MRI experiments were conducted within one week after delivery.

3.2.2 Preparation and characterization of particulate organic matter

Colloidal particles (SPIONs)

Superparamagnetic iron oxide nanoparticles (SPIONs) with a diameter d_p of 38 ± 10 nm were utilized as reference for colloidal particles resembling the colloidal fraction of particulate organic matter, (nanomag®-D-spio; Micromod Partikeltechnologie GmbH, Rostock, Germany). SPIONs consist of iron oxide cores covered by an organic dextran matrix. Large macromolecules consisting of dextran have been successfully applied in hydrolysis experiments before (Confer and Logan 1997). SPIONs have a zeta potential close to zero. Further, the particles showed no signs of agglomeration or sedimentation. The iron oxide cores serve as paramagnetic tagging causing fluctuating disturbances of the magnetic field. Hence, mainly transverse relaxation is enhanced creating predominantly a T_2 contrast. Information about the applied particle concentration and loading is given in Table 1. A detailed characterization of these particles is given in Cuny et al. (2015).

Chapter 3: Particle retention within aerobic granular sludge

Table 3-1: Experimental conditions for the experiments. To meet the requirements for MRI measurements, sample design and conditions differ from full- or lab-scale application. Changes between experiments are explained in chapter 3.2.4.

	experiment 1	experiment 2	experiment 3
applied particles	colloidal particles (SPIONs)	microcrystalline cellulose particles (MCPs)	real wastewater particles (WWPs)
paramagnetically tagged?	yes	yes	no
mean particle diameter/ size range	38 ± 10 nm	1 – 20 µm	28 – 100 µm
average flow velocity	0.78 m/h	0.78 m/h	0.39 m/h
flow direction	top to bottom	bottom to top	bottom to top
dry mass of particles applied during the experiment	13 mg	139 mg	155 mg
concentration	73.1 mg/L	1.0 g/L	4.7 g/L
particle load:			
applied volume duration	37 mL 37 min	80 mL 80 min	24 mL 48 min
dry mass of particles applied	2.7 mg	80 mg	113 mg
additional particle load:			
applied volume duration	140 mL 140 min	59 mL 59 min	9 mL 18 min
dry mass of particles applied	10.28 mg	59 mg	42.3 mg

Microcrystalline cellulose particles (MCPs) as model particulate organic matter

Cellulose is a major fraction of particulate organic matter in domestic wastewater as it originates from toilet paper (Ruiken et al. 2013). A dispersion of the base product (Alfa Aesar, Thermo Fisher Scientific GmbH, Karlsruhe, Germany) was sonicated and wet sieved to collect a size fraction between 1 and 20 μm . For paramagnetic tagging, MCPs have been suspended in a 50 g/L ferrous sulphate solution under anoxic conditions. After draining, the iron(II) saturated microcrystalline cellulose particles were dried at room temperature over night to allow for a complete oxidation of the often diamagnetic iron(II) to paramagnetic iron(III). No mobilization of iron(III) ions was recognized later on.

Real wastewater particles (WWPs)

Primary effluent wastewater of the pilot-scale wastewater treatment plant at Eawag, Dübendorf (Switzerland) was collected to extract real WWPs. After centrifuging (3000 rpm, 5 min) and decanting settled particles were collected and freeze-dried. Before conducting the experiment, the freeze-dried particles were suspended in ultrapure water, homogenized and wet sieved. A size fraction between 28 and 100 μm was further used.

3.2.3 Experimental setup and procedure

A small sample design was necessary, to meet imaging requirements (sufficient signal-to-noise ratio). The authors are aware that due to the small column diameter wall effects have a larger impact on the process compared to commonly applied pilot and full scale aerobic granular sludge reactors.

A schematic of the experimental setup is presented in Figure 3-1. The aerobic granules were placed inside a glass column with an inner diameter of 14 mm and a length of 100 mm. The height of the bed of settled granular sludge was approximately 50 mm. 2 cm space were given at each end of the column to distribute the flow before reaching the granular sludge bed. At the bottom glass spheres with a diameter of 2 mm stabilized the granular sludge bed. An O-ring and a mesh (size 0.7 mm, fabric) were positioned in between to separate the granules from the glass spheres. Both beds were wet packed to avoid air entrapment. The glass column was installed into the 200 MHz spectrometer and connected to a peristaltic pump (Ismatec, IPC, IDEX Health and

Science GmbH, Wertheim, Germany) via polytetrafluoroethylene capillaries (inner diameter: 0.75 mm; Duratec Analysentchnik GmbH, Hockenheim, Germany).

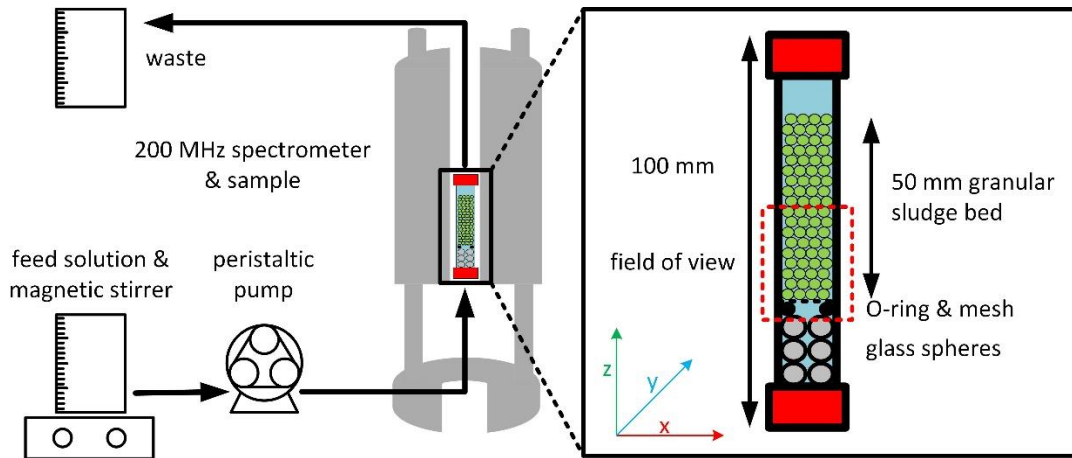


Figure 3-1: Experimental setup. MRI images were acquired along the first 22.5 mm of the granular sludge bed, according to the flow direction.

The granular sludge bed was initially rinsed with tap water for 60 min with a volumetric flow rate of 1 mL/min, corresponding to a flow velocity of 0.78 m/h. The particles were pumped through the column during two loading phases (see Table 3-1). In between the flow was turned off for image acquisition. The particle suspension (feed) was positioned on a magnetic stirrer being continuously mixed to avoid particle sedimentation. As channeling occurred at average velocities higher than 1 m/h, the particle concentration was adjusted to ensure a moderate experiment duration.

3.2.4 Adjusted parameters between experimental runs

The artificial particles (SPIONs and MCPs) were paramagnetic tagged. Paramagnetic tagging strongly enhances image contrast via paramagnetic relaxation enhancement. Untreated particulate organic matter does not significantly alter the MRI signal, unless it appears in a large concentration and geometric extensions e.g. in form of particle layers. The occurrence of particle layers in experiment 2, lead to the conclusion that paramagnetic relaxation enhancement is not necessary for micrometer sized particles in large concentrations. Thus, no paramagnetic relaxation enhancement was conducted in experiment 3. In addition, a larger minimum particle diameter has been chosen for the WWPs to conclusively neglect penetration into the biofilm matrix.

As channeling occurred at average velocities higher than 1 m/h, the particle concentration was adjusted to ensure a moderate experiment duration. In addition, the average flow velocity was adjusted in experiment 3 due to the channeling event in experiment 2. In general, high concentrations of particles in relation to biomass were necessary to allow for a clear detection of the transport behavior and differentiation of particles and granular sludge (e.g. signal-to-noise ratio).

Flow direction and field of view were changed for experiment 1 due to the aim of highlighting the granular sludge bed in contact with the bulk interface. Due to their particle size SPIONs are staying suspended for weeks without any signs of settling.

3.2.5 Magnetic resonance imaging

The experiments were performed on a 200 MHz nuclear magnetic resonance spectrometer (Bruker Avance HDIII 200 SWB, Bruker BioSpin GmbH, Rheinstetten, Germany). The superconducting magnet has a vertical bore of 150 mm and a magnetic-flux density B_0 of 4.7 T. A 25 mm birdcage of the MICWB 40 series was used. Gradients up to 1.5 T/m were available in all spatial directions (x , y , z). Multi-slice multi-echo imaging (MSME) was performed in 2D and 3D as provided within Paravision 6.0.1 (Bruker BioSpin GmbH, Rheinstetten, Germany). A signal-to-noise study revealed that a combination of T_1 - and T_2 -weighting is the most convenient. T_1 -weighted images favor the so called longitudinal relaxation differences, while simultaneously, but to a smaller extent transverse relaxation is occurring. Vice versa, the same applies for T_2 -weighted images. T_1 -weighted images were used to differentiate between granules and the bulk liquid. T_2 -weighted images were acquired to supplementary locate the added particles within the bed of settled granules. Data acquisition parameters are listed in Table 3-2.

Table 3-2: MRI data acquisition parameters. If not mentioned differently, the parameter values apply to both 2D and 3D measurements.

	T_1 -weighted	T_2 -weighted
Repetition time (T_R)	500 ms	2000 ms
Echo time (τ_E)	5 ms	2D: 30 ms, 3D: 35 ms
Averages	2D: 16, 3D: 2	2D: 4, 3D: 1
Image matrix size	2D: 192×128	
2D: zx-plane	3D: $192 \times 128 \times 128$	
Field of view	2D: 22.5 mm \times 15 mm	
2D: zx-plane	3D: 22.5 mm \times 15 mm \times 15 mm	
Resolution	117 μ m isotropic in 3D, in plane in 2D	
Slice thickness	1 mm (only 2D)	
Slice gap	2 mm (only 2D)	
Scan duration	2D: 17 min, 3D: 4.5 h	2D: 17 min, 3D: 9 h

3.2.6 Data analysis and visualization

Data analysis was performed within Matlab R2018b (MathWorks, Natick, MA, US) using home-written scripts and Avizo 9.4 (Thermo Fisher Scientific, Waltham, Massachusetts, USA). Graphical illustrations of the data analysis are provided in the supporting information. Briefly, the 3D datasets recorded at the end of each experiment have been segmented via interactive thresholding. In the T_1 -weighted images the shell of the granules showed high signal intensity and appeared bright. These signals were used to separate the granules from the background (e.g., bulk water phase). From T_2 -weighted images the dark appearing particles were extracted. The resulting binary datasets were combined, and an artificial color allocation was given to differentiate between void space (black), granules (green) and particles (yellow). In addition, granules and particles were assigned to the fraction of “granule + particle” (white) in case of spatially overlapping signals (co-localization, see Appendix 4-1). It has to be noticed, that the void space includes all voxels which have not been assigned to granules or particles during thresholding. In particular, these are interpreted as water filled pores and channels as well as the interior of granules (confer T_1 -weighted images in Appendix 4-1).

Chapter 3: Particle retention within aerobic granular sludge

Quantification has been achieved as follows: The volumetric fractions of each class have been determined for a region of interest in 3D. As the wastewater particles were also visualized (T_1 -weighted images), image analysis was adapted to quantify the fractions of granules, particles and void spaces correctly within the limitations of the approach (see Appendix 4-2).

3.3 Results

3.3.1 Experiment 1: Behavior of colloidal particles (SPIONs)

The aim of this experiment was to visualize and quantify the interaction of SPIONs in the bulk phase and the granular sludge bed. A set of MRI images shows the behavior of SPIONs in the granular sludge bed Figure 3-2.

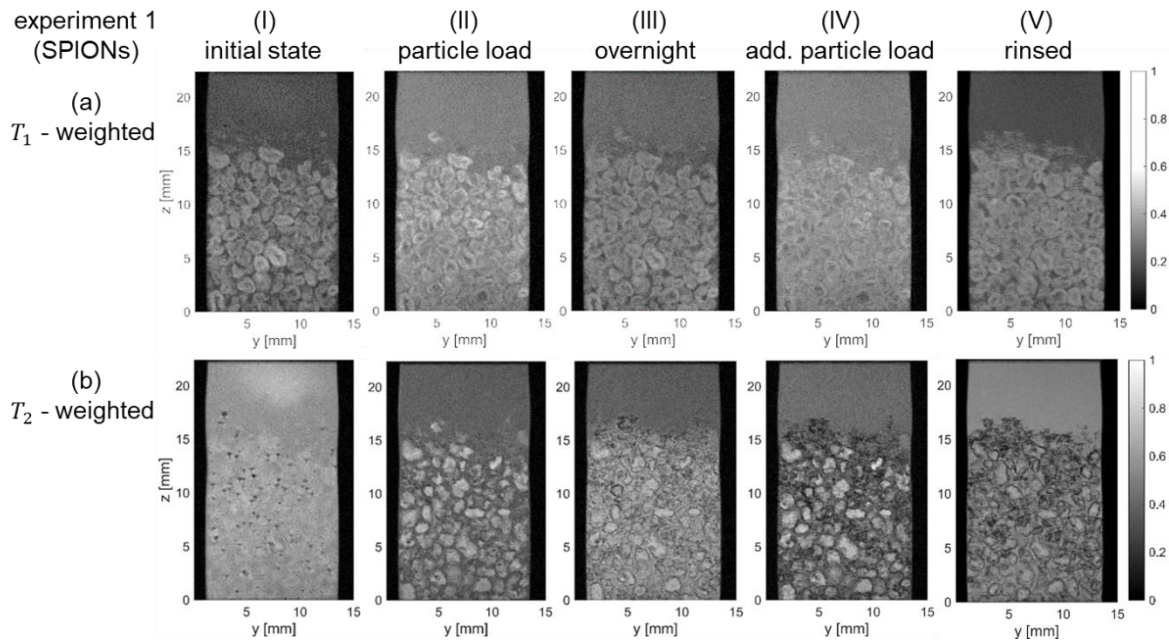


Figure 3-2: 2D MRI images (cross-sections) showing the distribution and sorption of SPIONs within the granular sludge bed. T_1 -weighted images (a) allow for a differentiation between granules and water filled pore space, while T_2 -weighted images (b) are more sensitive to SPION concentrations (e.g. particle load). The presence of SPIONs in the liquid enhances mainly T_2 -relaxation, but markedly affects also the T_1 -contrast. Sorption of SPIONs to granules is indicated as their surface becomes visible in terms of “dark” rings in T_2 -weighted images.

In Figure 3-2a, the T_1 -weighted images show the structure of the granular sludge bed. Bulk liquid phase and granules can be distinguished based on their respective T_1 -relaxation times. After applying the particle load, SPIONs were distributed within the pores of the granular sludge bed as visible in Figure 3-2a after step II. SPIONs enhance the relaxation of the liquid phase. The result is a brighter appearing liquid phase and a declined contrast between granules and liquid phase in T_1 -weighted images immediately after the SPION injection (compare steps I and II in Figure 3-2a). However, the T_2 -weighted images are more sensitive for the detection of SPIONs due to the inherent relaxivities of these SPIONs (Cuny et al. 2015). In T_2 -weighted images (Figure 3-2b, step II) the enhanced relaxation causes the low signal intensity of the liquid phase. In contrast to the initial image shown in Figure 3-2b (step I), the liquid phase can be distinguished from the granules in T_2 -weighted images.

To study the interaction of the SPIONs with and within the granular sludge bed driven by diffusion, flow was stopped. After 16 h without flow the pore space within the granular sludge bed appears bright in T_2 -weighted images (Figure 3-2, step III), which correlates to a low SPION concentration. The sorption of the colloidal particles to the granule surface is visible as a “ring” of low intensity in the T_2 -weighted images in Figure 3-2b (step III). In relation to the intensity of the granular sludge bed, the dark appearing bulk liquid phase above the granular sludge bed (see Figure 3-2b, step III) indicates a relatively high concentration of SPIONs. Without applied flow the SPIONs were not deeply entering the granular sludge bed, as no concentration gradient within the granular sludge bed is observed (Figure 3-2b, step III $z = 0 - 14$ mm). An additional particle load was reestablishing the concentration of SPIONs within the pore space of the granular sludge bed (compare Figure 3-2a and 2b, steps II and IV). By rinsing the granular sludge bed (see Figure 3-2, step V), mobile particles were removed. The T_2 -weighted image in Figure 3-2b (step V) shows residual SPIONs immobilized at the granule surface (see “dark” rings). The liquid above and within the pore space exhibit a similar signal intensity compared to the initial state indicating a low SPION concentration in the bulk liquid (compare Figure 3-2a, steps I and V).

3.3.2 Experiment 2: Behavior of microcrystalline cellulose particles (MCPs)

The set of T_1 - and T_2 -weighted MRI images in Figure 3-3 illustrates the behavior of MCPs ($d_p = 1 - 20$ μm) in the granular sludge bed. The formation of a channel through the granule bed can be observed on Figure 3-3a steps I to III at $y = 10 - 15$ mm. MCPs are not recognizable in the T_1 -weighted images.

After the initial particle load MCPs accumulated below the granular sludge bed which is indicated by the darker regions in Figure 3-3b (step II; $z = 0 - 3$ mm). Further accumulations of MCPs are visible along the channel at $y = 10 - 15$ mm (see Figure 3-3b, step II). In detail, MCPs are found at the granule surfaces or in void spaces situated next to the channel. Nevertheless, the major part of the granular sludge bed is free from MCPs (bright regions remaining in step II compared to step I in Figure 3-3b).

After the additional particle injection (see Figure 3-3b, step III) further particle accumulation filled void space next to the channel and partially the channel itself, while no (additional) particles distributed over the rest of the granular sludge bed. The development of a preferential flow path at $y = 10 - 15$ mm through the granular sludge bed was further confirmed by measuring flow (data not shown).

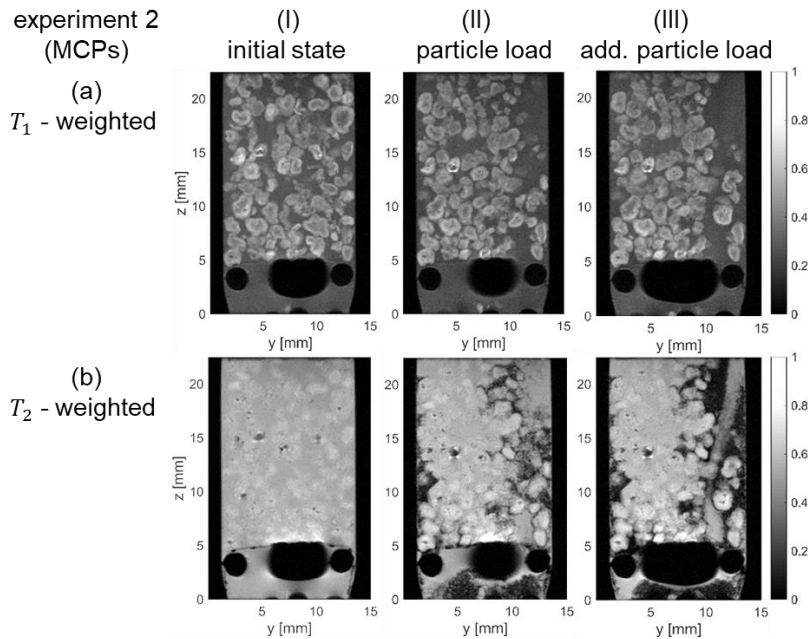


Figure 3-3: 2D MRI images showing the accumulation of microcrystalline cellulose particles (MCPs) in the granular sludge bed. T_1 -weighted images (a) allow for a differentiation between granules and water filled pore space, while T_2 -weighted images (b) are more sensitive to the particle load in form of low intensity signals. The granule bed reordered during the particle load, and a flow channel formed. An accumulation of MCPs occurred mainly near the inlet and along the flow channel (preferential flow path).

3.3.3 Experiment 3: Behavior of real wastewater particles (WWPs)

Figure 3-4 illustrates the behavior of real WWPs ($d_p = 28 - 100 \mu\text{m}$) inside the granular sludge bed. To avoid immediate channeling as observed during the experiment with MCPs (see section 3.3.2 above), the average flow velocity was lowered to 0.39 m/h.

Compared to the particles applied in the first two experiments (SPIONs, MCPs), WWPs caused an additional image contrast in predominantly T_1 -weighted images (see Figure 3-4a, steps II and III). WWPs appear brighter than the granules. The WWPs appear also more inhomogeneous in terms of signal intensity and are surrounded by some susceptibility artifacts (black dots in bright layer Figure 3-4a, steps II and III). The T_2 -weighted images are more sensitive to the WWPs. In Figure 3-4b the WWPs appear dark because of a faster T_2 -relaxation whereas the granules and void space are similar in signal intensity.

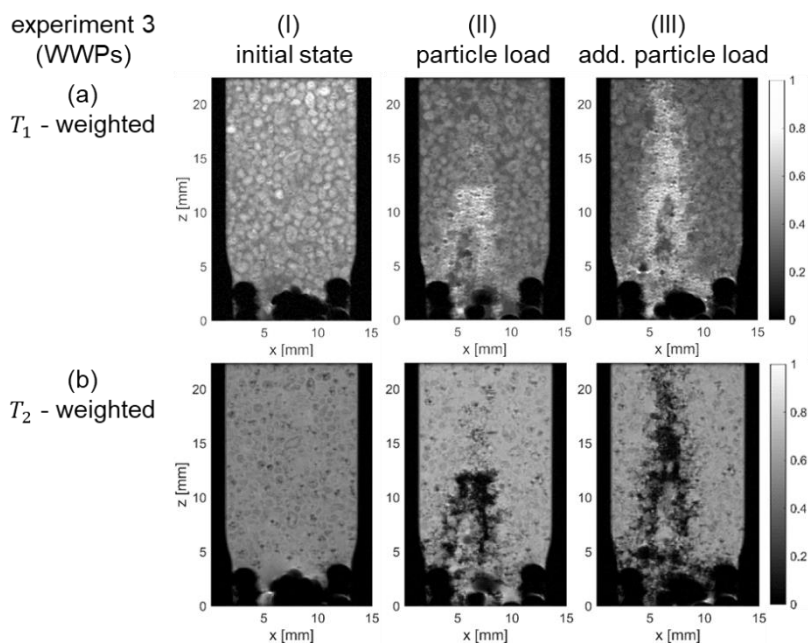


Figure 3-4: 2D MRI images showing the accumulation of real wastewater particles (WWPs) within the granular sludge bed. In T_1 -weighted images (a) granules, water filled pore space (low signal intensity) and particles (high signal intensity) are visible. The T_2 -weighted images (b) display the particles more homogenously. Particles appear dark (low signal intensity) whereas the water filled pore space and granules appear grayish (high signal intensity). The particles accumulated mainly within a channeled void space of the granular sludge bed.

The WWPs show a similar behavior compared to the MCPs. An accumulation in the void space and around the granule surfaces is observed after both injections (see Figure 3-4, steps II and III). Particles distribute within the granular sludge bed in the region of $x = 5 - 10$ mm and $z = 5 - 20$ mm. The granular sludge bed was slightly rearranged during both particle loadings as indicated in Figure 3-4a, step I compared to II and III. In this case the particles were slightly pushed through the granular sludge bed. In Figure 3-4, step III the additional particle load led to further infiltration of WWPs along the height of the granule bed as well as accumulation at the inlet ($z = 5$ mm, $x = 3 - 10$ mm).

3.3.4 Comparison of particle distribution

In this section, 3D MRI datasets from the end of each experiment are analyzed and compared. SPIONs (experiment 1) and micro particles (experiment 2 and 3) interact differently with the granular sludge bed (Figure 3-5). The SPIONs penetrated into the granules and remained immobilized/sorbed (white bars, Figure 3-5). Analysis of these 3D MRI datasets further revealed that SPIONs penetrated each granule independent of its surrounding environment (e.g., packaging density, granule size). Sorption of SPIONs occurred homogenously within the granular bed height ($z = 3 - 13$ mm) as

Chapter 3: Particle retention within aerobic granular sludge

presented in Figure 3-6, experiment 1. The penetration depth for SPIONs into the granules was estimated to up to $300 \pm 50 \mu\text{m}$.

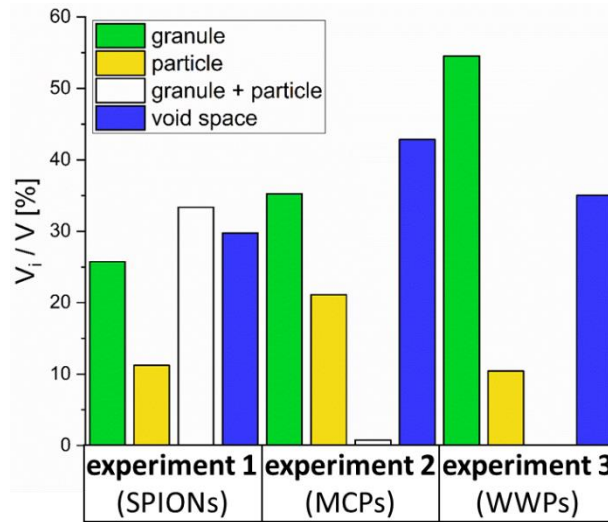


Figure 3-5: Volume fractions at the end of each experiment. SPIONs are able to penetrate the granules (white bars), while the WWPs and MCPs accumulate in the void space.

Due to the flow direction that's compacting the granular sludge bed, the granule content in experiment 1 is the highest ($\approx 60\%$ for "granule" and "granule + particle") in Figure 3-5. The higher flow velocity in experiment 2 and the channeling event lead to a lower granule fraction compared to experiment 3. In general, the "granule" fraction is underestimated within this approach, due to lower signal intensities at the inner of the aerobic granules.

Compared to the behavior of SPIONs, MCPs locate nearby granules (see Figure 3-5, experiment 2) but do not penetrate the granules. In consequence, the fraction of "granule + particle" (white color allocation) is below 1% in Figure 3-5 for MCPs compared to approximately 34% for SPIONs. Since the WWPs are larger than the MCPs no penetration of the larger particles into the granules is assumed. MCPs and WWPs behave similarly in terms of spatial distribution. Moreover, micro particles preferentially accumulate at lower parts of the granular sludge bed rather than distributing equally within the void space due to advective and diffusive transport processes as concluded from Figure 3-6, experiment 2 and 3. The distribution of MCPs is mainly affected by the geometry of the flow path (Figure 3-6, experiment 2). Particles gradually fill the void space along the channel, which causes a heterogeneous distribution of MCPs. In addition, a deposit of settled MCPs on top of the granular sludge bed was detected. The wastewater particle fraction (yellow) is sharply decreasing within the lower part ($z = 4 - 6 \text{ mm}$) of the granule bed (see Figure 3-6

experiment 3). The low “particle” fraction for WWP in Figure 3-5, indicates that most particles are already retained at the glass spheres positioned below the granular sludge bed (Figure 3-1). Almost complete particle retention was observed within the first 20 mm of the granule bed (see Figure 3-6, experiment 3). Also, an additional particle load or a higher flow velocity would release particles to the bulk phase atop the granular sludge bed similar to the observations made in experiment 2.

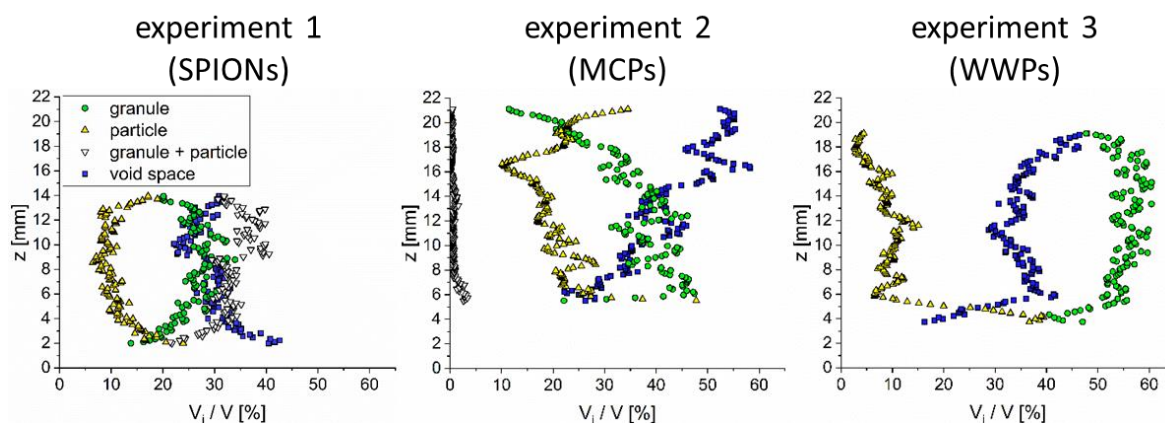


Figure 3-6: Particle distribution along height. In experiment 1 the SPIONs distributed homogenously along the height of the granular sludge bed. The accumulation of MCPs in experiment 2 is mainly affected by the geometry of the flow path. The amount of accumulated WWPs in experiment 3 decreases sharply within the first millimeters.

3.4 Discussion

3.4.1 Applicability of MRI

The results prove the applicability of MRI to study the fate and transport of particles into and through a settled bed of aerobic granules. T_1 -weighted images were successfully applied to resolve the structure of a settled bed of aerobic granules. Colloidal (SPIONs) as well as micro particles (MCPs, WWP) were resolved in time and space (x, y, z) by T_2 -weighted images.

Further processing and merging of 3D MRI data sets allowed for the determination of the particle position inside the granular sludge bed. Some uncertainties remain in the predictability of the granule and void space volume fractions. Because of their signal intensity, the cores of the granules are assigned to the void space fraction. The changes in signal intensity caused by diverse relaxation times within biofilms are usually aligned with its properties (i.e. compactness and chemical composition). For example, Bartacek et al. (2016) observed that the outer zone of aerobic granules has a faster T_1 - and T_2 -relaxation than the inner core. The faster relaxation times might be related to a higher amount of extracellular polymeric substances (EPS) and microorganisms at the outer layers (Adav et al. 2008, McSwain et al. 2005, Wang et al. 2005). Further, the presence of precipitates in granules was reported, which locally fastened relaxation time (Herrling et al. 2017, Kirkland 2017). Nevertheless, advanced image segmentation might improve the differentiation of void space and granule core via shape validating tools as applied by Bégin et al. (2014) on nerve fibers.

3.4.2 Particle retention

The current study demonstrates that the retention mechanism of particulate organic matter is size dependent. Retention of particulate organic matter in an aerobic granular sludge reactor increases with decreasing influent wastewater particle size (Schwarzenbeck et al. 2004). Our results show that colloidal particles distribute equally within the granular sludge bed under applied flow. Thus, colloidal particles are able to attach and penetrate granules. We hypothesize that the hydrolysis of colloidal particles takes place within the granules and will lead to a rather uniform distribution of additional substrate during the subsequent cycles of a SBR. Furthermore, the estimated penetration depth up to $300 \pm 50 \mu\text{m}$ suggests that the colloidal particles partially immobilize within the anoxic zone of aerobic granules. Therefore, hydrolysis would potentially release organic carbon to phosphorous accumulating and denitrifying

microorganisms in the anoxic zone and contribute to the growth of stable and compact granules (de Kreuk and Van Loosdrecht 2004, Layer et al. 2019, Pronk et al. 2015a).

Experiments with MCPs and WWPes support findings of Schwarzenbeck et al. (2004) who concluded that the removal efficiency of micro particles seems critical. Recent studies demonstrated that micro particles are not able to penetrate granules and are retained at the granule surface (De Kreuk et al. 2010, Morgenroth et al. 2002, Pronk et al. 2015a, Wagner et al. 2015). This study supports and extends this knowledge, as the accumulation of micro particles inside the void space was directly visualized during the feeding phase. Further particle accumulation leads to the formation of particle layers. The particle layer thickness exceeds the particle diameter, which leads to the conclusion that most of the particles are not attached to the granule surface but remain available/mobile after the feeding phase. Overall, around 80% of the particulate organic matter are in the micrometer range after a primary treatment step (Sophonsiri and Morgenroth 2004). Therefore, a large quantity of particulate organic matter might not necessarily be washed out with the effluent but stays distributed/remobilized over the whole reactor within the (aerobic) mixing phase.

3.4.3 Influence of flow velocity on particle distribution

Average flow velocity through the granular sludge bed during the anaerobic feeding phase is a particularly important strategic parameter. Experiment 1 showed that convection is necessary to distribute the SPIONs over the granular sludge bed. Here, a low flow velocity of 0.78 m/h allowed for a uniform distribution of particles within the void space which is followed by sorption of SPIONs to aerobic granular sludge. The impact of flow on the particle distribution is evident in the experiments utilizing MCPs and WWPes, respectively. Channels formed, that led to preferential flow and thus advective transport of particles occurred. In experiment 2, high velocities inside the channel lead to a transport of MCPs through the entire granular sludge bed. This caused the sedimentation of MCPs on top of the granular sludge bed. In case of the WWPes a reduced average velocity of 0.39 m/h was sufficient to retain the majority of the particles within the first 20 mm of the settled bed of aerobic granules. However, for the typical anaerobic feeding time of around one hour 0.39 m/h would be much too low. Typically, average flow velocities range from 1 – 5 m/h for low strength wastewater (Derlon et al. 2016, Li et al. 2014, Pronk et al. 2015b, Wagner et al. 2015). Channeling has been reported on full scale reactors at average filter velocities from 3 to 3.3 m/h

(Pronk et al. 2015b). Our findings indicate that channeling might also occur at average filter velocities below 1 m/h. Hence, average filter velocities and volume exchange ratio should be considered to minimize the risk of washing out particulate organic matter during simultaneous fill and draw, as applied by Pronk et al. (2015b) on full scale reactors.

3.5 Conclusions

- MRI is a suitable analytical tool to visualize and quantify the transport and retention behavior of colloidal (SPIONs) and micro particles (microcrystalline cellulose particles (MCPs) and real wastewater particles (WWPs) inside a granular sludge bed. The combination of T_1 - and T_2 -weighted images allowed for the localization of granules, void space and particles in all spatial directions and over time.
- The size of particles (colloidal or several micrometer large) governs their fate within the granular sludge bed during feeding.
- Colloidal particles (SPIONs) distributed equally in the void space during the feeding phase. These also penetrate the granules homogeneously by up to $300 \pm 50 \mu\text{m}$. As these particles are retained and immobilized inside the granules, degradation will most likely occur delivering additional substrate even in anoxic regions of aerobic granules.
- Micrometer-sized particles of micro crystalline cellulose (model particles) as well as real wastewater particles were affected by gravitation/sedimentation. Particles accumulated within as well as on top of the granular sludge bed. Results indicate that a large fraction of these particles remains mobile and might be degraded in subsequent phases of a SBR cycle or might be discharged causing constant or elevated effluent concentrations.

4 Locally and time resolved imaging of particle deposition within a granulated activated carbon filter – Impact on the flow field (Submitted)

4.1 Introduction

Both phosphorous and micro pollutants (MPs) discharged into surface water can be identified as threat to water quality (Brack et al. 2018, Eggen et al. 2014, Leaf 2018). Accordingly, phosphorous and micro pollutants (e.g. diclofenac, benzene) are listed as hazardous substances to the aquatic environment by the European water directive (Council of the European Communities 1976, European Parliament and Council of the European Union 2008). As the final barrier before pollutants enter into the aquatic environment, wastewater treatment plants (WWTPs) play an important role in the sustainable development of natural water bodies. In Germany, several federal states react to the problem by introducing higher requirements for the discharge of phosphorous and implementation of advanced treatment methods for the removal of MPs (Bornemann et al. 2012, Hillenbrand et al. 2016, Telgmann et al. 2020).

Amongst others, granulated activated carbon (GAC) is an advanced treatment method. Dependent on the integration within the treatment, a GAC filter may fulfill several purposes. Besides the use as adsorbent, the accumulation of biofilm allows for a simultaneous biological degradation of slowly biodegradable substances. Recently, Fundneider et al. (2021b) reported of an extended life span of 25 – 42% related to the biological degradation within GAC filters. Further, the function of GAC as filter medium is widely reported. In regard of the removal of suspended solids (SS), different integrations of GAC filters within a treatment are reported: (I) GAC was used as a pretreatment step to remove SS and to prevent fouling of micro-/ultrafiltration units (Hamid et al. 2017, Im et al. 2019, Pramanik et al. 2014), (II) GAC filters were applied as single filtration step (Altmann et al. 2016, Meinel et al. 2015, Telgmann et al. 2020), (III) a separate filtration step was applied to remove SS before the GAC treatment (Fundneider et al. 2021a, Knopp et al. 2016). These approaches highlight different perspectives on the suitability of GAC as a filtration medium, which might be caused by a lack of knowledge in the occurring filtration processes.

Chapter 4: Particle deposition on GAC filters

However, some observations can be drawn from full and pilot scale. In general, the filtration process and occurring headloss is influenced by characteristics like the grain size of GAC, filtration velocity and SS concentration. Ongoing with the amount of SS in the influent more frequent backwashing of GAC filters is required. However, the backwashing frequency should be kept at a minimum as it is related to downtimes, abrasion of GAC and additional energy requirements. Commonly GAC filters are applied in top-down filtration. In here, most particles do not enter deeply into the GAC filter, resulting in a strong headloss at the upper 30 cm (Altmann et al. 2016, Telgmann et al. 2020). To gain detailed insights into the particle deposition within GAC filters and related consequences, imaging methods might be applied. X-ray and nuclear magnetic resonance (NMR) based methods allow to resolve the packed bed structure and particle deposition *in-situ* in 3D (Al-Abduwani et al. 2005, Godinho et al. 2019, Mikolajczyk et al. 2018, Ranzinger et al. 2020b). Besides a detailed localization of particle depositions, recent studies were able to resolve flow induced particle layer redistributions within deposit layers and packed beds via μ CT (Adebayo and Bageri 2020, Godinho et al. 2019). A benefit of MRI is the possibility to measure flow distributions within packed beds in addition to structural images (Graf von der Schulenburg et al. 2008, Mikolajczyk et al. 2018, Seymour et al. 2004, Wagner et al. 2010).

Overall the most efficient treatment to reduce phosphorous discharge to low levels, is seen in precipitation/ flocculation followed by a filtration step (Fundneider et al. 2020, Telgmann et al. 2020). In here, an overlap can be found as a GAC filter can be used as a filter medium to remove precipitated phosphorous in form of SS and MPs simultaneously. The aim of the present study is to gain further insights into the filtration process, to evaluate if a combination or separation of treatments is advantageous from a pore scale perspective. Therefore, the present study used MRI to dynamically visualize the deposition of SS onto a GAC filter. Further, real wastewater originating from a secondary clarifier was loaded in steps of 0.2 L. In accordance to previous studies, a pretreatment in form of a coagulation/flocculation step was applied to the wastewater (Altmann et al. 2016, Telgmann et al. 2020). In detail, the aim of the study was: (I) to reveal spatially and time resolved insights in the filtration process of SS onto GAC and (II) to investigate the impact of SS deposition on flow distributions within GAC filters.

4.2 Materials & Methods

4.2.1 Pretreatment

Wastewater was collected from the secondary clarifier effluent at the wastewater treatment plant in Bruchsal, Germany. The plant is designed for a population equivalent of 57.750. Initial concentrations were 14.9 mg/L dissolved organic carbon (DOC), 0.03 mg/L phosphate and 2.2 mg/L total suspended solids (TSS). To increase TSS content, 2 mg Phosphate (originating from potassium dihydrogenphosphate) were added to one liter of wastewater and precipitated by the addition of 5 mg iron (originating from iron(III)chloride). During precipitation, the sample was stirred at 200 rpm. For flocculation 100 rpm were applied. After pretreatment the wastewater contained 8.4 ± 0.5 mg/L TSS.

Granulated activated carbon (GAC) was obtained from Cabot Corporation, Boston, Massachusetts, USA. The GAC type (NORIT® RB 0.8 C) was extruded and had a cylindrical shape ($d = 0.8$ mm, $l = 3$ mm). Moreover, the chosen GAC showed the least artifacts and thus the best image quality. Previous to the experiments the GAC was sieved, washed and stored for one week in demineralized water to ensure complete outgassing of GAC.

4.2.2 Magnetic Resonance Imaging (MRI)

MRI experiments were performed in a 200 MHz superwide bore magnet equipped with an Avance HDIII console (Bruker BioSpin GmbH, Rheinstetten, Germany). The probe was a MICWB 40 with a 20 mm birdcage. For imaging, gradients up to 1.5 T/m were available. The parameters of MRI experiments are listed in Table 4-1. Multi-slice-multi-echo (MSME) was chosen for structure images. Multiple Echoes were recorded within the 3D measurement. Tagging was applied for the sagittal flow images.

Table 4-1: Acquisition parameters of MRI experiments.

Notation:	Coarse structure image	Sagittal flow image	Axial structure image	Axial Flow Map	Sagittal structure image	3D image
Acquisition time:	17 min 4 s	12 min 48 s	17 min 4 s	12 min 48 s	1 h 8 min	9 h 6 min
Data provided in:	Supporting video material	Figure 4-5 + supporting video material	Figure 4-6 + (Appendix)	Figure 4-6 + (Appendix)	Figure 4-3	Figure 4-4
Acquisition interval:	0.25 h; 0.2 L	0.5 h; 0.4 L	0.5 h; 0.4 L	0.5 h; 0.4 L	1.0 h; 0.8 L	2.0 h; 1.6 L
Field of view: (x, y, z)	15 mm, -, 22.5 mm	15 mm, -, 22.5 mm	15 mm, 15 mm, -	15 mm, 15 mm, -	15 mm, -, 22.5 mm	15 mm, 15 mm, 22.5 mm
Resolution: (x, y, z)	117 μm , -, 117 μm	117 μm , -, 117 μm	117 μm , 117 μm , -	117 μm , 117 μm , -	59 μm , -, 59 μm	117 μm , 117 μm , 117 μm
Slice thickness: [μm]	400	400	400	400	400	N/A
Repetition time:	2000 ms	2000 ms	2000 ms	1000 ms	2000 ms	2000 ms
Echo time:	15 ms	15 ms	15 ms	5 ms	15 ms	3.75 ms ... 15 ms
Averages:	4	3	4	3	16	1

4.2.3 Experimental setup

A schematic of the experimental setup is presented in Figure 4-1. The sample (height: 200 mm; inner diameter 14 mm) was wet packed with GAC to a height of approximately 100 mm. An O-ring and mesh at the bottom of the column served as supporting layer. Further, the sample was connected using tubings and installed into the 200 MHz NMR spectrometer. The sample was positioned within the spectrometer so that the field of view covered the upper layer of the GAC as well as the bulk liquid above. For one cycle, 0.2 L of pretreated wastewater were filled into a syringe. The syringe pump was positioned above a magnetic stirrer to ensure fully mixed conditions within the syringe during the cycle.

A filter velocity of 5 m/h was applied corresponding to a volumetric flow rate of 12.8 mL/min and a cycle time of 15.6 min. During a cycle, flow in either x-, y- or x-, z-direction was measured. As two different approaches for flow imaging (Sagittal flow image and axial flow map; see Table 4-1) have been chosen, these were acquired in alternating

order every 0.4 L. In between cycles, structural images were acquired. As compromise between image quality and data acquisition duration, coarse structure images were acquired after every cycle of 0.2 L in sagittal orientation and every second cycle in axial direction. 2D-images with higher resolution were obtained every 0.8 L. Further, 3D images were only obtained overnight (every 1.6 L). Details of the applied measurements and pulse sequences are provided in Table 4-1.

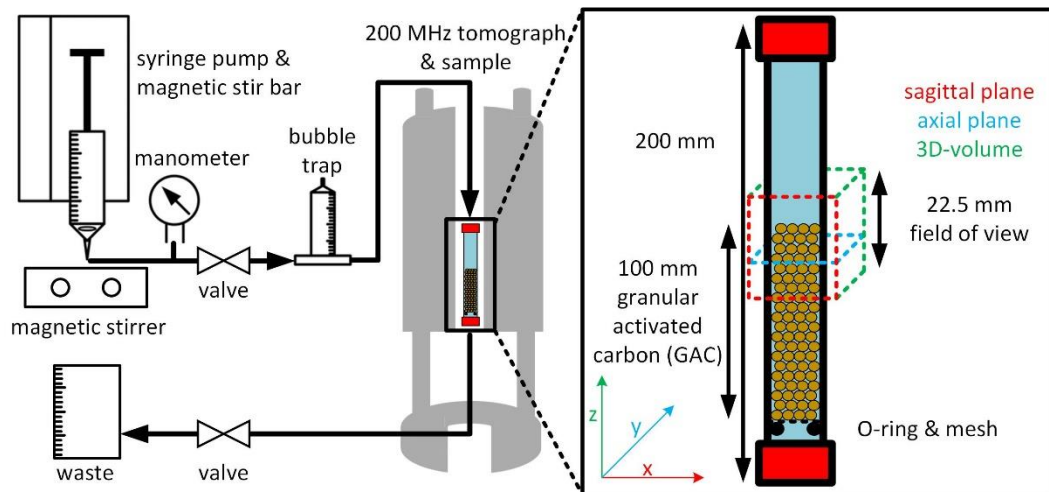


Figure 4-1: Experimental setup of the MRI experiments. In each cycle 0.2 L of pretreated wastewater were added to the GAC packed column. The upper 1.5 cm and liquid phase above the GAC filter were investigated in time and spatially resolved image series.

4.2.4 Image analysis

Image analysis was performed by using Avizo (Thermo Fisher Scientific, Waltham, Massachusetts, USA) and self-written scripts within Matlab (Math Works, Natick, Massachusetts, USA). In the following paragraph the analysis of flow distribution and 3D images are described in detail.

4.2.5 Processing of Flow images

For visualization purposes, the axial structure image and axial flow map were merged similar to (Gladden and Mitchell 2011, Klotz 2019). All raw and merged images can be found in the supporting information (Appendix 4-1). To distinguish the void space and solid material (GAC and SS), a threshold of 4500 out of 2^{15} intensity values (32768 values due to data format) was set. Further, a circle was manually defined, to distinguish between exterior parts and GAC. Within the axial flow-map only pronounced velocities above 0.1 cm/s were included. Values below 0.1 cm/s were considered as noise and removed from the image. The images were merged according to the following priority: (I) the highest priority was given to velocities > 0.1 cm/s of the flow map; (II) solid components (GAC and SS) were implemented (dark grey); (III) residual voxels within the drawn circle, that did not contribute to either GAC or a measured velocity were attributed to a flow velocity of 0 cm/s (appear dark blue); (IV) elements outside the circle were not included (appear black).

In addition, the measured flow distributions were classified. Overall 30 classes were defined according to a class width of 0.4 cm/s. Thus, the total velocity range was 0.1 - 12.1 cm/s. To calculate the volumetric flow rate (Q) of each voxel its velocity in z-direction was multiplied by the voxel size in x- and y-direction (= areal cross-section). In respect to one class all volumetric flow rates were summed up.

The flow distributions are plotted as probability density functions (PDF) and cumulative density functions (CDF) similar to (Carrel et al. 2018, Holzner et al. 2015). Further, the points were used to fit the “Lognormal” and “LognormalCDF” function as provided within Origin (OriginLab, Northampton, Massachusetts, USA).

4.2.6 3D-image analysis:

From the 3D measurements, the datasets recorded at the lowest (3.75 ms) and highest echotime (15 ms) were used for analysis purposes (compare Figure 4-2I and III). The dataset obtained after an echo time of 3.75 ms (Figure 4-2I) allows to highlight GAC. Further, a threshold of 4500 out of 2^{15} intensity values was applied. In addition, the connected objects smaller than 5 voxels in 2D were removed from the data set. The highlighted GAC is presented in Figure 4-2II.

The dataset obtained from an echo time of 15 ms were binarized at the same value (4500 out of 2^{15} intensity values). In respect to the fine structure of SS, the connected objects were evaluated in 3D. Again all connected objects smaller than 5 voxels were removed. The highlighted GAC + SS are presented in (Figure 4-2IV).

After that images were merged to distinguish between GAC and SS (Figure 4-2V). In here, a voxel was aligned to GAC if it was binarized in both images. If a voxel was only binarized at a higher echotime, it was aligned to SS. Further, height profiles were obtained from the merged datasets (Figure 4-2V). For visualization purposes images were rendered in 3D (Figure 4-2VI).

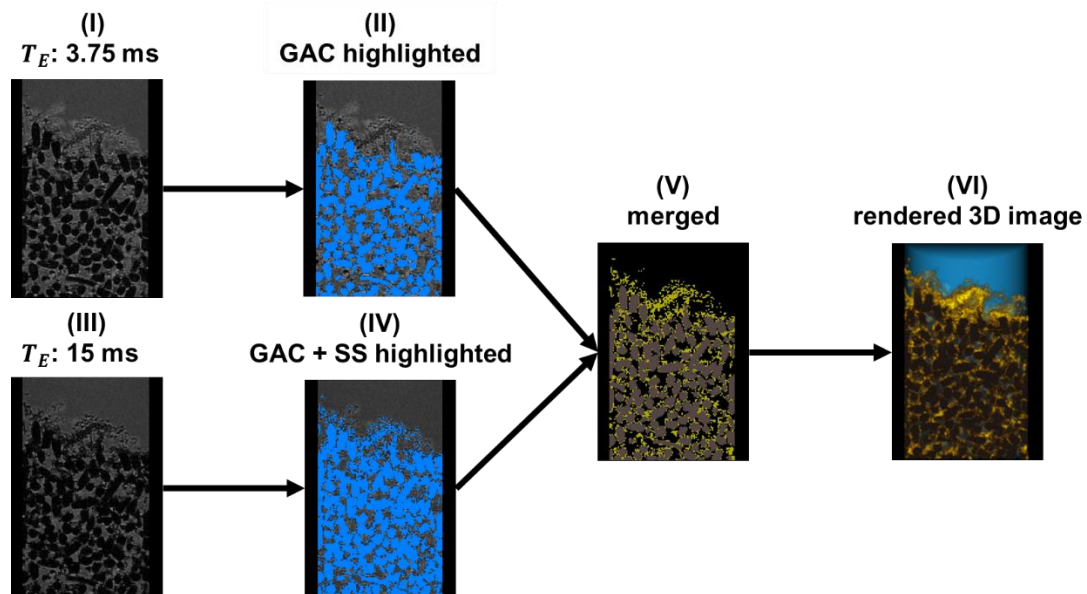


Figure 4-2: Image analysis of 3D measurements. Datasets recorded with the lowest (3.75 ms) and highest (15 ms) echo time were used. After image processing both datasets were merged and further rendered for 3D visualization only.

4.3 Results

4.3.1 Particle retention and GAC redistribution

Sagittal images ($y = 7.5$ mm) show the upper layer of the GAC filter (Figure 4-3). An image of the GAC packing before the addition of wastewater is provided in Figure 4-3I. MRI obtains most of the signal from the hydrogen atoms of water molecules. Thus, bulk liquid above the GAC filter as well as voids within the GAC filter appear grey. Regions indicated in white are the result of susceptibility artifacts, which appear near the interface between water and GAC filter. No signal is obtained from the GAC filter and exterior components. Thus, they appear black. Further, the cylindrical shape of the GAC can be recognized (Figure 4-3I).

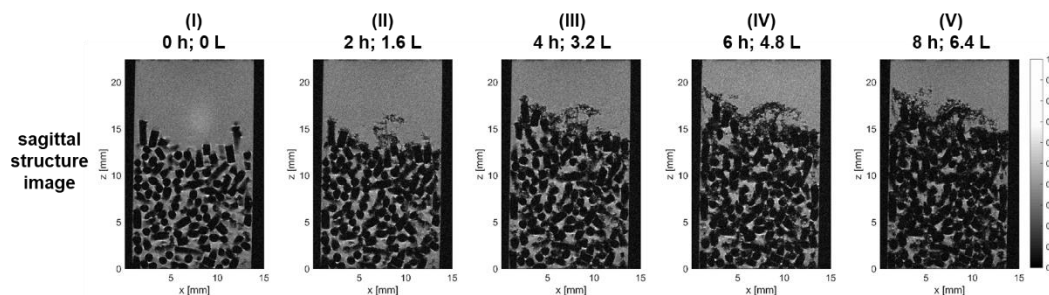


Figure 4-3: Normalized 2D-images show the GAC filter structure and the accumulation of SS. With ongoing addition of wastewater, SS accumulation is dominantly observed at the bulk – GAC interface, resulting in a deposit layer.

After 1.6 L of wastewater were added, SS accumulation was determined on the bulk – GAC interface (Figure 4-3II, $z = 12 - 16$ mm). The visualization of particles is influenced by the dimension of flocs/particles (approximately $1-10$ μm), the plane resolution of the MRI images (59 $\mu\text{m} \times 59$ $\mu\text{m} \times 200$ μm), and paramagnetic relaxation enhancement (through precipitation with iron). Overall, SS are only recognizable when present as accumulations. Further, the SS accumulations appear darker than water. In addition, their fluffy appearance is recognizable in terms of structure as well as diversity of signal intensity (Figure 4-3II, $z = 12 - 16$ mm).

After 3.2 L of wastewater were loaded, the occurrence of a deposit layer can be recognized atop the GAC filter (Figure 4-3III, $z = 13 - 18$). Further, a redistribution of the GAC filter occurred. The redistribution is distinct in the area of $z = 12 - 18$ mm and $x = 0 - 5$ mm (compare Figure 4-3II and III). In general, redistributions are aligned with an increase in pressure until a disruption within the filter structure occurs (Godinho et al. 2019). As seen in Figure 4-3IV and V more SS accumulated after loading 4.8 and 6.4 L, respectively. Moreover, the deposit layer appears darker and more compact,

which indicates a compression of particles at the upper edge. Beside of the formation of a deposit layer, SS are also retained within the GAC filter. For a more dynamic perspective on the particle retention within the GAC filter, the authors encourage to view the animations provided within the supporting information.

Rendered 3D images with corresponding height profiles are presented in Figure 4-4. As explained in material and methods 3D images of an echo time of 3.75 and 15 ms were merged (see Figure 4-2) for differentiation between GAC and particle accumulations. Dashed lines mark the start and end, respectively, of the developing deposit layer. In consequence, Figure 4-4II-a does contain only 1 dashed line that separates the fully developed GAC filter from the GAC – bulk interface.

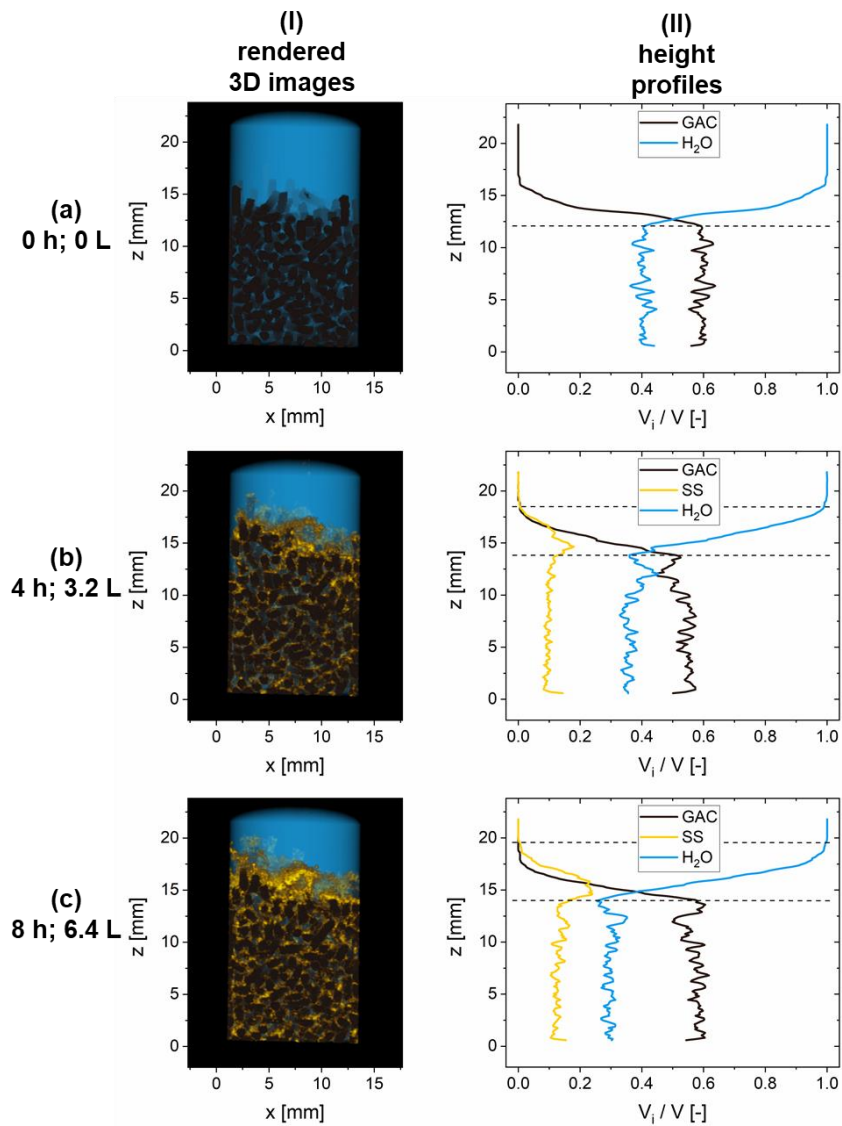


Figure 4-4: Rendered 3D images and height profiles of the experiment after 0 L; 3.2 L and 6.4 L of wastewater passed through the GAC filter. Particles accumulate above GAC filter by formation of a deposit layer. In addition, the accumulation of SS the GAC filter is shown.

The height profiles show the highest amount of SS at the bulk – GAC interface (Figure 4-4: row b; $z = 13.5 - 18$ mm). Successively, more SS can be found above the GAC filter after 6.4 L passed. In addition, the height of the deposit layer increases from approximately 5 to 6 mm compare Figure 4-4; row b and c. Further, the minima of V_{H_2O} / V at $z = 14$ mm indicates progressing pore blockage.

SS were also retained within the GAC filter. No clear trend within the GAC filter is seen for the SS profile after 3.2 L were loaded (Figure 4-4; row b; $z = 0 - 13.5$ mm). Within the GAC filter ($z = 0 - 13.5$ mm) V_{SS} / V increased during operation from 9.8% (3.2 L) to 12.9% (6.4 L). Vice versa, V_{H_2O} / V within the GAC is lowered, starting from 40.5% (0 L) down to 36.8% (3.2 L) and 29.8% (6.4 L). In respect of V_{H_2O} / V a redistribution of the GAC filter is recognizable at 3.2 L, leading to a loosening of the GAC structure (Figure 4-4; row b; $z = 8 - 13.5$ mm). Therefore, V_{GAC} / V is higher after 6.4 L (57.3%) compared to 3.2 L (53.4%) (compare Figure 4-4; row b and c; $z = 8 - 13.5$ mm).

4.3.2 Flow distribution above and within the GAC filter

In Figure 4-5 sagittal flow images are presented. In here, horizontal stripes are implemented that allowed to derive flow profiles above the GAC filter.

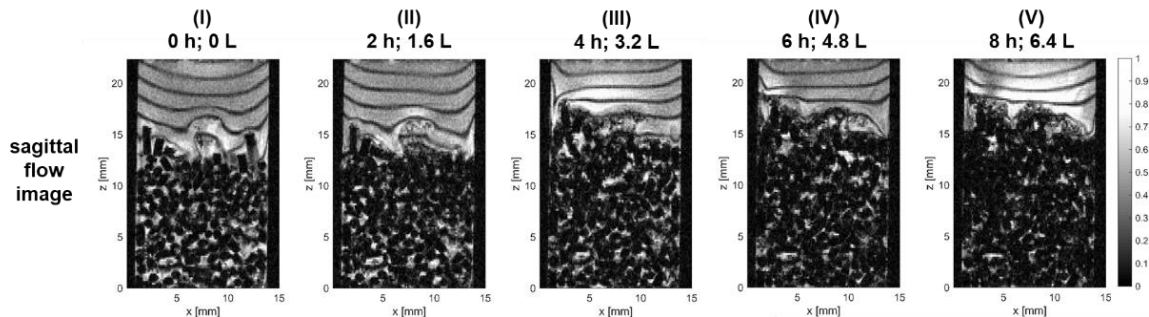


Figure 4-5: 2D sagittal flow images revealing flow profiles within the bulk liquid above the GAC filter. The accumulation of SS causes redistributions of GAC and accumulated SS at the top of the GAC filter aligned with changing inflow points into the GAC filter. Formation of channeling can be recognized.

Within the upper part of the bulk liquid a laminar flow profile is recognizable in form of a parabolic shape (Figure 4-5I, $z = 18 - 22$ mm). Altered by the geometry of the GAC filter, the flow profile changes at lower parts of the bulk liquid near the bulk – GAC interface. A resistance can be recognized in the middle of the filter (Figure 4-5I, $z = 13 - 18$ mm). Within the GAC filter the stripes are not recognizable. A deficit in visibility of structures and contours becomes obvious when comparing Figure 4-3 and Figure 4-5, which is aligned with the image acquisition under applied flow.

After 1.6 L of wastewater were added, preferential inflow locations are recognizable (Figure 4-5II; $x = 5$ mm and $x = 14$ mm). In addition, the initial parabolic flow profile is flatter and less distinct. At Figure 4-5III a dominant inflow spot is seen at $x = 1$ mm, while an even flow distribution is recognizable over other areas. Also the highest saturation stripe is affected by the preferential inflow spot (Figure 4-5III; $z = 21 - 22$ mm). After 4.8 L and 6.4 L of wastewater were loaded, a preferential spot is recognized at $y = 14$ mm (Figure 4-5IV and V).

Figure 4-6(I-III) shows axial flow maps. The GAC together with SS are superpositioned inside these images for visualization purposes and appear dark. The raw images can be found within the supporting information (Appendix 4-1). Figure 4-6I shows the initial flow regime obtained at a height of $z = 5$ mm. Within the flow map, low velocities along z -direction are found. Most of the void space is labeled in dark blue corresponding to low or no detected velocity along z -direction. Whereas some areas are labeled in cyan or green corresponding to velocities of 1.5 to 3 cm/s. Further, the GAC structure is clearly recognizable within the image (Figure 4-6I).

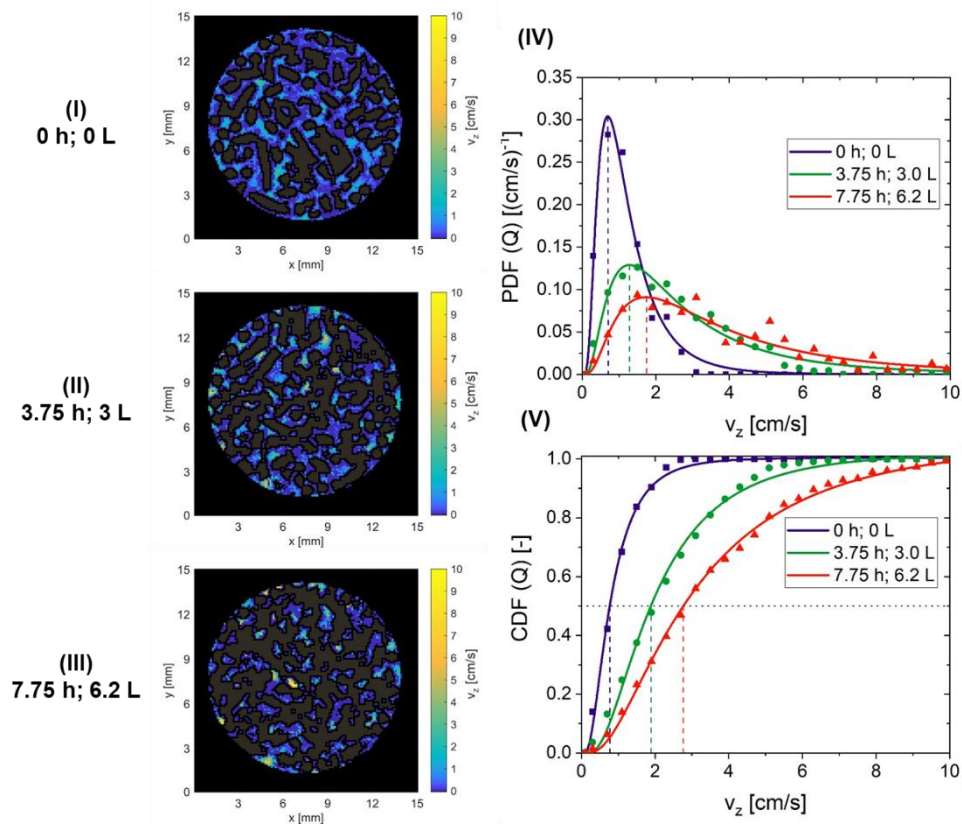


Figure 4-6: Axial flow maps before (I), after 3.0 L (II) and 6.2 L (III) addition of wastewater. Corresponding volume flow distributions are presented in (IV) as probability density and (V) cumulative density function. Characteristic values of Table 4-2 (mode and equivalent velocity) are highlighted within the diagram. The accumulation of SS promotes channeling effects and leads to higher equivalent velocities.

Chapter 4: Particle deposition on GAC filters

Overall an increasing amount of solid components (GAC and SS; dark grey) can be recognized during the experiment (Figure 4-6II and III). After 3.0 L of wastewater were loaded, higher velocities and less areas displaying markedly velocities are observed. In general, channels within the GAC filter with a higher velocity developed locally. Channeling further increases with successive loading of wastewater (compare Figure 4-6I, II and III). The trend towards higher velocities is further shown in Figure 4-6IV and V. In here, the volume flow distributions in z-direction are plotted against probability functions CDF (Q) and PDF (Q), respectively. Characteristic values are provided in Table 4-2.

The mode of the volume flow distribution shifts from 0.7 to 1.3 and 1.7 cm/s. Further, the equivalent velocity (the velocity at which 50% of the volume flow pass the image at a higher/lower velocity) increases from (0.8 to 1.9 and 2.8 cm/s). The comparison of mode and equivalent values further indicate the trend towards anomalous flow distributions caused by the accumulation of SS.

Table 4-2: Characteristic values of the volume flow distributions.

Operation time; Loaded volume	Mode of volume flow distribution	Equivalent velocity (50% quantile)
0.00 h; 0.0 L	0.7 cm/s [25.2 m/h]	0.8 cm/s [28.8 m/h]
3.75 h; 3.0 L	1.3 cm/s [46.8 m/h]	1.9 cm/s [68.4 m/h]
7.75 h; 6.2 L	1.7 cm/s [61.2 m/h]	2.8 cm/s [100.8 m/h]

4.4 Discussion

4.4.1 Retention of SS in GAC filters is affected by local flow field

The current study provides temporal and spatially resolved insights into the occurring filtration processes in GAC filters. Overall, the formation of a deposit layer and retention within the GAC filter is recognized. Tendencies either towards deep bed filtration or surface filtration were reported in previous studies (Benstoem et al. 2017, Telgmann et al. 2020). Further, the findings are in alignment with pilot scale observations, which reported of a major particle retention within the upper 15 cm of a GAC filter (Altmann et al. 2016, Telgmann et al. 2020). In general, diverse parameters affect the retention characteristics, including filter velocity, particle load, grain size and others.

In addition, the present study highlights the significance of the local flow field onto the particle deposition. Sagittal flow images revealed that the inflow points into the GAC filter vary with time. Further, the inflow points obscure the formation of a deposit layer that completely covers the GAC filter. The transition to another preferential inflow point was often aligned with redistributions of the filter structure at the top of the GAC filter. The issue of redistribution might be even more distinct in real applications, as smaller and less dense GAC particles are situated at the upper layer of GAC filters due to stratification (Frank et al. 2015). Further, the presence of preferential inflow points enhances the particle transport into deeper regions of the GAC filter. Regarding the resulting pressure loss observed in real applications, additional insights can be drawn: (I) pore coverage is significant especially at the top GAC layer; (II) indications of SS compaction are recognizable at the upper part. The combination of both potentially acts self-reinforcing on the pressure loss, which is undesirable for a filtration process. Due to the self-reinforcing action and occurring redistributions that prevent a pure surface filtration, the authors would recommend to apply a pretreatment with sedimentation or filtration.

4.4.2 Impact of volume flow distribution on GAC

The current study shows the occurrence of channeling within GAC filters. Already without SS accumulation channeling is present within the GAC filter. In our study with an equivalent velocity of 28.8 m/h (= 0.8 cm/s), water passes the plane faster than predicted by the average filter velocity (5 m/h), even when taking the porosity (40%) into account (12.5 m/h). In here, the particle size distribution as well as the sample geometry is determining the channeling extend. Overall, channeling effects become more dominant with increasing heterogeneity (Blunt et al. 2013, Lehoux et al. 2016, Scheven et al. 2005). Further, it should be considered that the equivalent velocity also impacts the actual contact time for mass transfer processes. For instance, Liang et al. (2007) highlighted within their simulations, that the overall removal efficiency decreases at higher equivalent velocities.

With ongoing accumulation of SS channeling becomes more dominant. Such, tendencies towards channeling are well known for the case of biofilm accumulation in porous media (Carrel et al. 2018, Graf von der Schulenburg et al. 2008, Seymour et al. 2004). In our study, an equivalent velocity of 68.4 m/h was found after 3.0 L of wastewater was added, which further increased to 100.8 m/h after 6.2 L. Implications on the adsorption process of MPs are roughly outlined in the following. As the volume is transported through less pores but at a higher velocity, imperfect mixing (low horizontal dispersion) as well as a decrease of the actual contact time (broad longitudinal dispersion) are likely. In contrary, the concentration boundary layer will decrease due to higher velocities and allow for a faster mass transport towards GAC. Overall, we expect that the adsorption coefficient along height is lowered due to the occurrence of higher equivalent velocities. However, as the particle retention is mostly taking place within the upper 15 cm of a GAC filter (Altmann et al. 2016, Telgmann et al. 2020), the equivalent velocity measured is not representative for the whole GAC filter. Commonly mass transfer towards GAC only occurs at a fraction of the filter height within the so called mass transfer zone. Regarding the sufficient MPs removal reported in real scale applications, the effect is most likely compensated due to the total height of GAC filters (Altmann et al. 2016, Bornemann et al. 2012, Kårelid et al. 2017).

4.5 Conclusions

- MRI is a suitable tool to visualize SS accumulations within GAC filters. The approach allowed for a spatially and time resolved observation of the filtration processes and alterations of the local flow field.
- The formation of a deposit layer above as well as SS accumulation within the GAC filter can be quantified based on the MR images. Varying inflow points into the GAC filter developed quickly indicating, that the deposit layer did not completely cover the GAC – bulk interface. Further, compaction of SS and redistribution at the top layer were aligned with changing inflow points.
- Channeling was present within the GAC filter previous to the addition of wastewater. The equivalent velocity of 28.8 m/h was 2.3 times higher than the average flow velocity. The accumulation of SS further increased channeling. At the end of the experiment an equivalent velocity of 100.8 m/h was measured.
- Overall, the filtration using GAC seems unfavorable due to increasing blocking and compaction of SS evident after 4 h and 8 h of filtration, respectively. Therefore, the authors would recommend to apply a pretreatment with sedimentation or filtration.

5 Summary

The present dissertation highlights the suitability of MRI to visualize depositions within porous media (e.g. through particle deposition or biofilm growth) spatially and time resolved. A visualization of all fractions was possible by the combination of three aspects: (I) individually chosen MRI-parameters (mainly Repetition and Echotime) to create an adequate contrast; (II) addition of iron as contrast agents to modify the relaxation time of the deposited fraction within the porous media; and (III) individually designed image processing.

Especially the usage of iron showed great potential as contrast agent. Even though, the addition has to be considered individually in every case, the present study highlights diverse ways of application for MRI experiments. The addition to the substratum allowed for an accumulation within the biofilm matrix and thus to an improvement of contrast for biofilm growth studies (chapter 2). Second the soaking under anoxic conditions and later oxidization within cellulose showed great potential for triggering particles (chapter 3). In here, advantage was taken from the water solubility of iron(II)salts. The later on oxidization lead to an immobilization of iron(III) within the cellulose particles. However, also manufactured particles consisting of an iron oxide core showed great potential. An advantage is the narrow particle size and broad choice of surface functionalization (chapter 3). Finally, the usage of iron(III) as precipitant for phosphorous and organic compounds created particles that were trackable by MRI (chapter 4). Especially the last case represents a real scale application as precipitation/flocculation steps are commonly applied within wastewater treatment.

Chapter 2 highlighted the potential of biofilms to alter hydraulic conditions in respect to the retained amount of water as well as air. Under alternating water availability, the biofilm was found to preferentially grow at the contact points between two particles or between particles and glass column that remained permanently wetted. Only to a smaller extend the growth of biofilm was found within voids or at the surface of glass spheres. With ongoing biofilm growth, the retention of entrapped water after drainage events increased. Vice versa, the amount of entrapped air increased after flushing events. Further the potential of biofilm to enhance liquid phase connectivity was shown. Therefore, it is assumed that biofilm supports diffusive mass transport processes within partially saturated porous media.

Chapter 3 focused on the fate and retention of particles within settled beds of aerobic granules. In here, particles of different size-ranges (e.g. nanometer or micrometer range) were used. The SPIONs (20 nm in diameter) were not affected by sedimentation. Thus, SPIONs were able to distribute homogeneously within the bed of aerobic granules during loading. Further, SPIONs were able to penetrate the biofilm-matrix. However, SPIONs immobilized close to the surface of aerobic granules and did not penetrate the aerobic granules deeper than 300 μm . In contrast, sedimentation played an important role in the retention mechanism of micrometer sized particles (Chapter 3; Experiment 2 and 3). In here, the particles were retained outside the EPS matrix. The retention in form of accumulations, highlighted that most of the particles were not in direct contact with the aerobic granules. Thus, no adsorption to the aerobic granules was possible for the majority of added particles. Therefore, micrometer sized particles will become available within the following aerobic mixing phase within SBRs where they become available for flocs as well as aerobic granules. Noteworthy is also the second manuscript: Layer et al. (2020) of the project. In here, lab scale experiments have been conducted to investigate the fate of particulate matter within anaerobic feeding and aerobic mixing. The outcome indicates that most of the particulate matter will attach to sludge flocs during the aerobic mixing phase. Due to the typical time for biodegradation of particulate matter around 14 days, particulate matter is likely to be partly degraded and further to be taken off with the regular withdrawal of excess sludge.

Chapter 4 visualized the deposition of SS onto GAC filters. Within the top-down filtration particles were retained within as well as above the porous media. The timely resolved process allowed to visualize the buildup of a deposit layer above as well as the particle deposition within the GAC filter. With ongoing time a successive blockage of pores and a compaction of SS could be shown, that might have the potential to drastically increase the head loss. Even though, a deposit layer formed on top of the layer, the visualization of preferential inflow points highlighted that the deposit layer did not cover the whole area of the GAC filter. The formation of a filter cake was mainly obscured by the hydraulic conditions. During the filtration process a successively increasing equivalent velocity was found. In detail the equivalent velocity increased from 28.8 m/h (before loading of SS); up to 68.4 m/h (after 3.75 h of filtration) and 100.8 m/h (after 7.75 h of filtration). Therefore, channeling is largely enhanced through the deposition of SS. As the contact time is affected by the equivalent velocity it is assumed

Chapter 5: Summary

that the adsorption performance towards the GAC is lowered due to the accumulation of SS. In regard of the overall good performance in terms of SS retention and pollutant adsorption in real scale applications, it is assumed that the effect is compensated due to the total height of a GAC filter.

As chapter 3 and 4 both addressed the particle retention within porous media, cross comparisons can be made. In both chapters, the transport of particles towards and filtration within the porous media was highly influenced by the hydraulic conditions. Further, pore-scale imaging revealed redistributions within the structure of the porous media during the filtration experiment. The filtration efficiency can be influenced by the inflow direction towards the porous media, applied filter velocity and characteristics of the porous media (e.g. grain size, density, compressibility).

In wastewater treatment a density close to water is desirable for backwashing and fluidization of the porous media. This aspect is applicable for GAC as well as aerobic granules. However, for the filtration process a low density of the porous media is prone for redistributions. Further, fluidization leads to stratification of the porous media due to sedimentation processes. Therefore, the porous media will consist of larger and denser grains at the bottom, while lighter and smaller grains can be found close to the top.

Further, the inflow direction does significantly influence the space for redistributions. In chapter 3 micro-particles entered from the bottom. In down-top direction the porous media can be pushed upwards, loosened or elevated, which can cause strong redistributions. For example, a preferential flow path was created due to flow induced redistributions in experiment 2. In the following, particles deposited along it, while others passed the porous media and deposited on top of the porous media. The risk of particle breakthrough can be lowered by decreasing the flow velocity, as shown in experiment 3. In here, the particles were largely retained at lower parts but were also pushed through the porous media during the experiment.

The top down filtration direction (top-down filtration) restricts the expansion of the porous media. Thus, it is more stable against particle breakthrough. However, due to a more successive blocking of pores on top of the porous media and the development of a deposit layer it is prone to develop a fast headloss. However, also redistributions occurred in here and avoided the formation of a filter cake covering all pores to completely retain particles before they enter the porous media. Due to progressing

channeling effects, particles were also transported into deeper regions of the porous media.

Overall the present study highlights the dynamic interplay between depositions (biofilm growth and particle accumulation) and hydraulic properties within the porous media. However, not only the depositing fraction is altered but also the porous media might be redistributed due to the dynamically changing hydraulic conditions. Therefore, the porous media should not be seen as a static system from the pore scale perspective, but does also align to the local flow conditions

6 Appendix

Appendix 2-1: Cultivation under saturated condition for OCT measurements

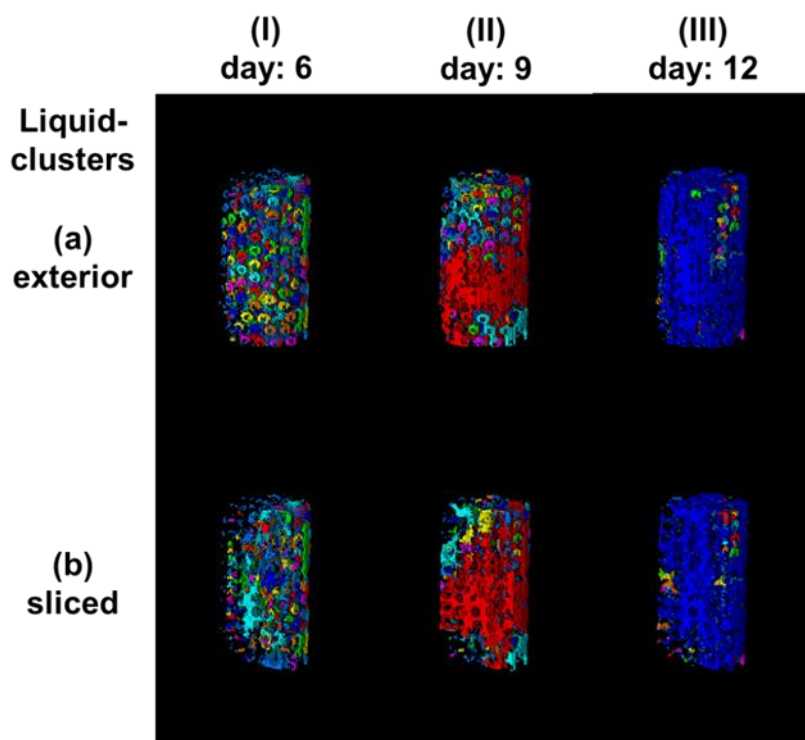
The sample was inoculated with *Bacillus subtilis* pre-cultures grown at 30°C overnight in Luria Broth (LB) medium. For the cultivation, a feed solution with the concentrations shown in table S1 was prepared and autoclaved. The feed solution was constantly lead into a beaker trough a peristaltic pump. This beaker was connected to the probes and served as a reservoir for mixing, recirculation and oxygen input through continuous stirring. An overflow drain allowed the discharge of excess solution.

To start the cultivation, the beaker was innocultated with 5 mL of pre-culture. Then, the mixture was pumped through the probes for 15 minutes to ensure a good distribution of bacteria, followed by an one hour waiting period to allow for surface attachment. This procedure was repeated a second time. During the following cultivation, the probes were constantly fed from the beaker with an average filter velocity of 5.4 m/h, resembling 0.6 mL/min. The probes were used as an indication of biofilm growth over time and could be examined with OCT, because of the complete saturation.

Substances added to one liter of demineralized water for preparing the feed solution.

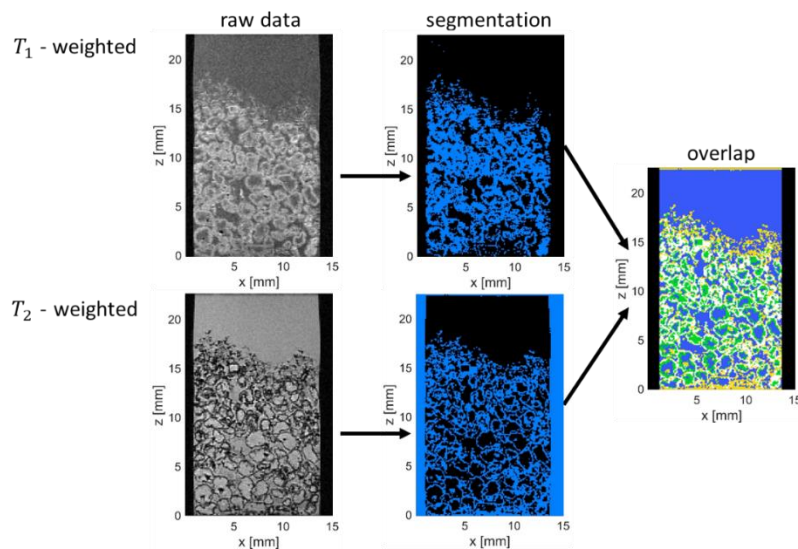
Substance	Concentration [mg/L]
Tryptophan	5
Phenylalanin	5
Thiaminhydrochlorid	0.67
ZnCl ₂	0.136
MnCl ₂	9.9
FeCl ₂	0.5
CaCl ₂	110
MgCl ₂	410
Glycerol	500

Appendix 2-2: Visualization of liquid clusters

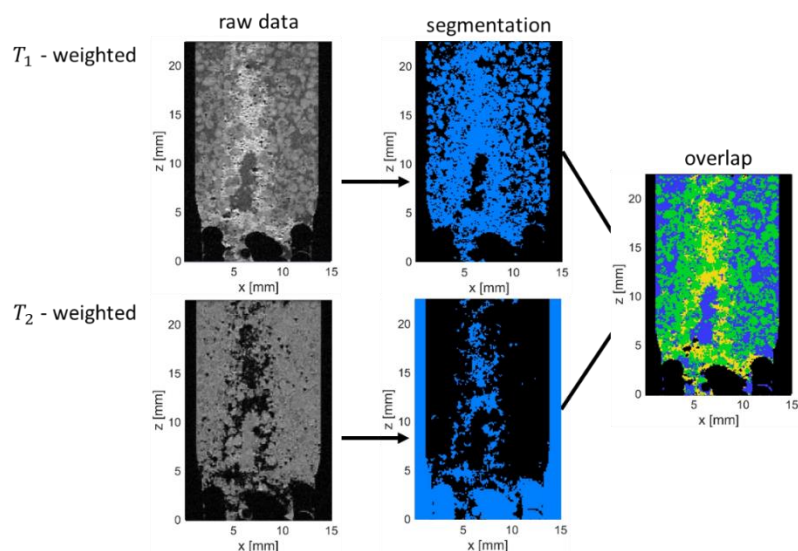


Visualization of liquid clusters. The same dataset is shown from an exterior perspective (a) and sliced through the center (b). On day 6, ringlike structures of retained water can be recognized. At day 9 a dominant cluster can be recognized, which covers contains almost the complete liquid phase at day 12.

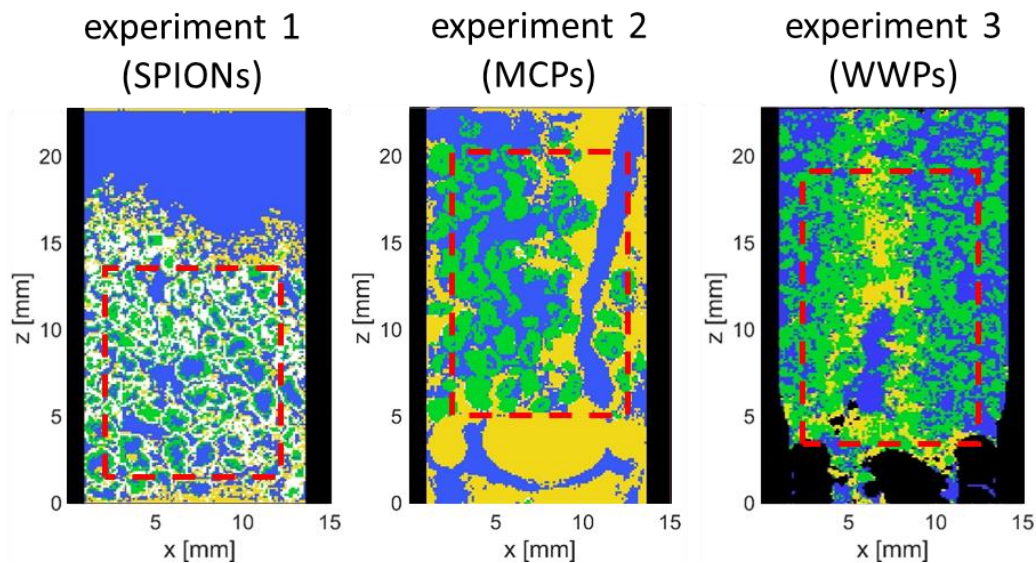
Appendix 3-1: Image segmentation; analysis and direct comparison



Data analysis of 3D MRI data sets. T_1 -weighted images were selected for granules via thresholding, while T_2 -weighted images were selected for the particles. As the field of view is the same the binary images can be directly merged and divided into volume fractions. Void space is indicated in blue; granules are aligned to green; particles are illustrated in yellow if they are located in the void space or in white when they spatially overlap with the granule fraction.

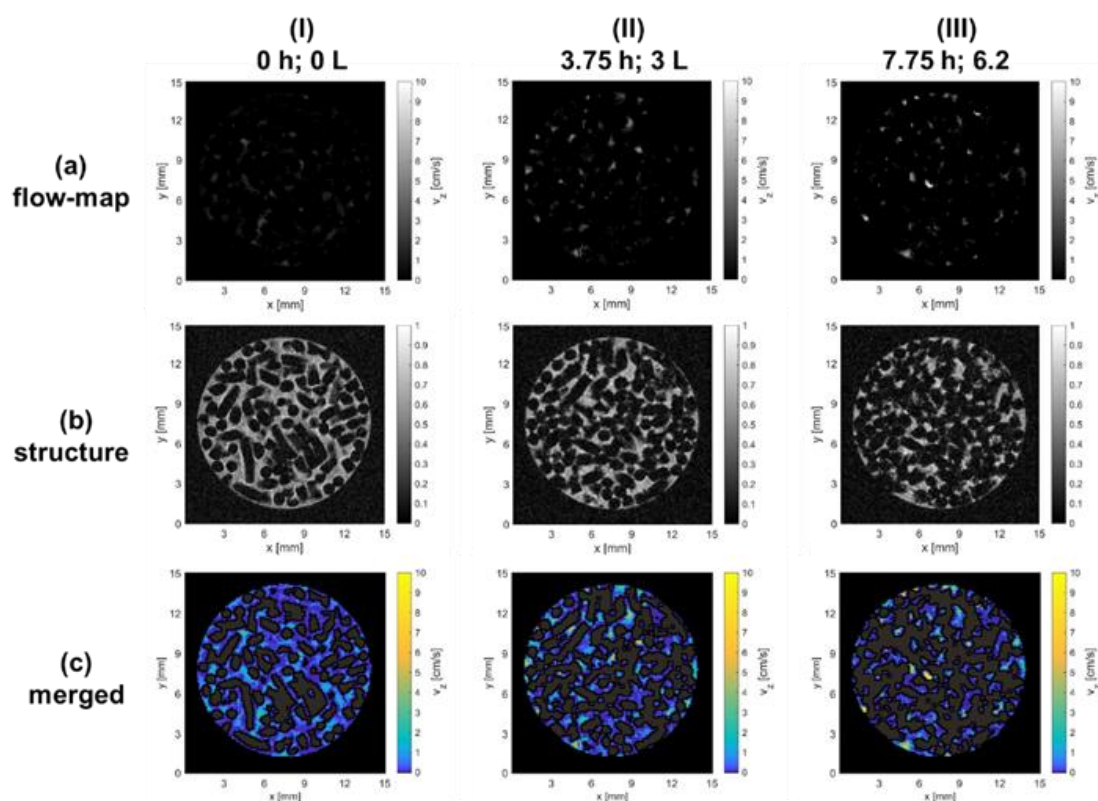


Data analysis of the 3D MRI data sets for wastewater particles. The T_1 -weighted images were selected for granules and particles because of their similar intensity range. T_2 -weighted images were selected for the particles. Because of the limited selectivity in T_1 -weighted images, it was not possible to quantify if wastewater particles overlap with granules.



3D data sets after quantification. 2D images out of the 3D data sets are shown for visualization purposes. Regions of interest of approximately 1000 mm³ have been defined (see red dashed rectangles) to quantify the aforementioned volumetric fractions in the granulated sludge bed. In Experiment 1, SPIONs are able to penetrate the granules, while MCPs and WWPs accumulate in the pore space in Experiment 2 and 3.

Appendix 5-1: Merging of structure and flow datasets.



Comparison of raw image data of the flow-map (a), structure (b) and processed images (c).

Verification of the contribution from the co-authors

Title: Investigation of Biofilm Growth within a Monodisperse Porous Medium under Fluctuating Water Level Assessed by Means of MRI

Journal: Water; Section Water and Soil, Water 13, no. 18

Authors: Florian Ranzinger, Karin Schröter, Harald Horn, and Michael Wagner

Position in the dissertation:

The content of this paper has been included in Chapter 2

Contribution of Florian Ranzinger (1st author)

- Conceived the concept of experiments
- Designed and conducted MRI experiments
- Visualized and analyzed data
- Wrote the manuscript

Contribution of Karin Schröter (2nd author)

- Designed and conducted preliminary experiments
- Conducted OCT measurements
- Wrote parts of methodology
- Discussed results
- Corrected manuscript

Contribution of Harald Horn (3rd author)

- Discussed concept and design of experiment
- Discussed results
- Corrected manuscript

Contribution of Michael Wagner (last author)

- Discussed concept and design of experiment
- Discussed results and visualization of data
- Corrected manuscript

Permission from MDPI:

“For all articles published in MDPI journals, copyright is retained by the authors.”

Source: <https://www.mdpi.com/authors/rights>

Accessed on: 15th of November 2021

Appendix

Title: Transport and retention of artificial and real wastewater particles inside a bed of settled aerobic granular sludge assessed applying magnetic resonance imaging

Journal: Water Research X 7

Authors: Florian Ranzinger, Maximilian Matern, Manuel Layer, Gisela Guthausen, Michael Wagner, Nicolas Derlon, and Harald Horn

Position in the dissertation:

The content of this paper has been included in Chapter 3

Contribution of Florian Ranzinger (1st author)

- Designed and conducted MRI experiments
- Visualized and analyzed data
- Wrote the manuscript

Contribution of Maximilian Matern (2nd author)

- Conducted MRI experiments
- Assisted in visualization and analysis of data

Contribution of Manuel Layer (3rd author)

- Supply of essential materials (Granules and Wastewater particles)
- Discussed design and results of experiments
- Corrected manuscript

Contribution of Gisela Guthausen (4th author)

- Designed and discussed experiments
- Advised setting of MRI parameters
- Corrected manuscript

Contribution of Michael Wagner (5th author)

- Discussed concept of experiments and manuscript
- Discussed results and visualization of data
- Corrected manuscript

Contribution of Nicolas Derlon (6th author)

- Conceived concept of experiments
- Discussed results
- Corrected manuscript

Contribution of Harald Horn (last author)

- Conceived concept of experiments
- Discussed concept and design of experiment
- Discussed results
- Corrected manuscript

Permission from Elsevier:

“Authors can include their articles in full or in part in a thesis or dissertation for non-commercial purposes.”

Source: <https://www.elsevier.com/about/policies/copyright/permissions>

Accessed on: 15th of November 2021

Appendix

Title: Locally and time resolved imaging of particle deposition within a granulated activated carbon filter – Impact on the flow field

Journal: (Submitted to Separation and Purification Technology)

Authors: Florian Ranzinger, Harald Horn, and Michael Wagner

Position in the dissertation:

The content of this paper has been included in Chapter 4

Contribution of Florian Ranzinger (1st author)

- Designed and conducted MRI experiments
- Visualized and analyzed data
- Wrote the manuscript

Contribution of Harald Horn (2nd author)

- Conceived concept of experiment
- Discussed concept and design of experiment
- Discussed results
- Corrected manuscript

Contribution of Michael Wagner (last author)

- Discussed concept and design of experiment
- Discussed results and visualization of data
- Corrected manuscript

7 Nomenclature

AGS	Aerobic granular sludge
CLSM	Confocal laser scanning microscopy
COD	Chemical oxygen demand
EPS	Extracellular polymeric substances
GAC	Granular activated carbon
GAO	Glycogen accumulating organism
LB	Luria broth
MCPs	Microcrystalline cellulose particles
MPs	Micro pollutants
MRI	Magnetic resonance imaging
MSME	Multi-slice-multi-echo
NMR	Nuclear magnetic resonance
OCT	Optical coherence tomography
PAO	Phosphate accumulating organism
PHA	Polyhydroxyalkanoate
SBR	Sequencing batch reactor
SPIONs	Super paramagnetic iron oxide nanoparticles
SS	Suspended solids
WWPs	Wastewater particle
WWTP	Wastewater treatment plant
μ -CT	Micro-computed tomography

8 References

- Adav, S.S., Lee, D.-J. and Tay, J.-H. (2008) Extracellular polymeric substances and structural stability of aerobic granule. *Water research* 42(6-7), 1644-1650.
- Adebayo, A.R. and Bageri, B.S. (2020) A simple NMR methodology for evaluating filter cake properties and drilling fluid-induced formation damage. *Journal of Petroleum Exploration and Production Technology* 10(4), 1643-1655.
- Al-Abduwani, F., Farajzadeh, R., Van den Broek, W., Currie, P. and Zitha, P. (2005) Filtration of micron-sized particles in granular media revealed by x-ray computed tomography. *Review of scientific instruments* 76(10), 103704.
- Altmann, J., Rehfeld, D., Träder, K., Sperlich, A. and Jekel, M. (2016) Combination of granular activated carbon adsorption and deep-bed filtration as a single advanced wastewater treatment step for organic micropollutant and phosphorus removal. *Water research* 92, 131-139.
- Anlauf, H. (2019) *Wet Cake Filtration: Fundamentals, Equipment, and Strategies*, John Wiley & Sons.
- Arndt, F., Schuhmann, S., Guthausen, G., Schütz, S. and Nirschl, H. (2017) In situ MRI of alginate fouling and flow in ceramic hollow fiber membranes. *Journal of Membrane Science* 524, 691-699.
- Bartacek, J., Vergeldt, F.J., Maca, J., Gerkema, E., Van As, H. and Lens, P.N. (2016) Iron, cobalt, and gadolinium transport in methanogenic granules measured by 3D magnetic resonance imaging. *Frontiers in Environmental Science* 4, 13.
- Bégin, S., Dupont-Therrien, O., Bélanger, E., Daradich, A., Laffray, S., De Koninck, Y. and Côté, D.C. (2014) Automated method for the segmentation and morphometry of nerve fibers in large-scale CARS images of spinal cord tissue. *Biomedical optics express* 5(12), 4145.
- Benneouala, M., Bareha, Y., Mengelle, E., Bounouba, M., Sperandio, M., Bessiere, Y. and Paul, E. (2017) Hydrolysis of particulate settleable solids (PSS) in activated sludge is determined by the bacteria initially adsorbed in the sewage. *Water research* 125, 400-409.
- Benstoem, F., Nahrstedt, A., Boehler, M., Knopp, G., Montag, D., Siegrist, H. and Pinnekamp, J. (2017) Performance of granular activated carbon to remove micropollutants from municipal wastewater—A meta-analysis of pilot-and large-scale studies. *Chemosphere* 185, 105-118.
- Bianchi, F., Wittel, F.K., Thielmann, M., Trtik, P. and Herrmann, H.J. (2018) Tomographic study of internal erosion of particle flows in porous media. *Transport in porous media* 122(1), 169-184.
- Blumich, B. (2000) *NMR imaging of materials*, OUP Oxford.
- Blunt, M.J., Bijeljic, B., Dong, H., Gharbi, O., Iglauer, S., Mostaghimi, P., Paluszny, A. and Pentland, C. (2013) Pore-scale imaging and modelling. *Advances in water resources* 51, 197-216.
- Boltz, J.P. and Motta, E.J.L. (2007) Kinetics of particulate organic matter removal as a response to bioflocculation in aerobic biofilm reactors. *Water environment research* 79(7), 725-735.
- Bornemann, C., Hachenberg, M., Kazner, C., Herr, J., Jagemann, P., Lyko, S., Benstöm, F., Montag, D., Platz, S. and Wett, M. (2012) Ertüchtigung kommunaler Kläranlagen, insbesondere kommunaler Flockungsfiltrationsanlagen durch den Einsatz von Aktivkohle. Projekt Nr. 5, Abschlussbericht zum Forschungsvorhaben, Elimination von Arzneimitteln und organischen Spurenstoffen: Entwicklung von Konzeptionen und innovativen, kostengünstigen Reinigungsverfahren.
- Bouma, B. (2001) *Handbook of optical coherence tomography*, CRC Press.
- Bozorg, A., Gates, I.D. and Sen, A. (2015) Using bacterial bioluminescence to evaluate the impact of biofilm on porous media hydraulic properties. *Journal of microbiological methods* 109, 84-92.

- Brack, W., Escher, B.I., Müller, E., Schmitt-Jansen, M., Schulze, T., Slobodnik, J. and Hollert, H. (2018) Towards a holistic and solution-oriented monitoring of chemical status of European water bodies: how to support the EU strategy for a non-toxic environment? *Environmental Sciences Europe* 30(1), 1-11.
- Bristow, N.W., Vogt, S.J., O'Neill, K.T., Vrouwenvelder, J.S., Johns, M.L. and Fridjonsson, E.O. (2020) Flow field in fouling spiral wound reverse osmosis membrane modules using MRI velocimetry. *Desalination* 491, 114508.
- Brussaard, L. (2012) Ecosystem services provided by the soil biota. *Soil ecology and ecosystem services*, 45-58.
- Buetehorn, S., Utiu, L., Küppers, M., Blümich, B., Wintgens, T., Wessling, M. and Melin, T. (2011) NMR imaging of local cumulative permeate flux and local cake growth in submerged microfiltration processes. *Journal of Membrane Science* 371(1-2), 52-64.
- Caizán-Juanarena, L., Krug, J.R., Vergeldt, F.J., Kleijn, J.M., Velders, A.H., Van As, H. and Ter Heijne, A. (2019) 3D biofilm visualization and quantification on granular bioanodes with magnetic resonance imaging. *Water research* 167, 115059.
- Callaghan, P.T. (1993) *Principles of nuclear magnetic resonance microscopy*, Oxford University Press on Demand.
- Carrel, M., Beltran, M.A., Morales, V.L., Derlon, N., Morgenroth, E., Kaufmann, R. and Holzner, M. (2017) Biofilm imaging in porous media by laboratory X-Ray tomography: Combining a non-destructive contrast agent with propagation-based phase-contrast imaging tools. *PloS one* 12(7), e0180374.
- Carrel, M., Morales, V.L., Beltran, M.A., Derlon, N., Kaufmann, R., Morgenroth, E. and Holzner, M. (2018) Biofilms in 3D porous media: Delineating the influence of the pore network geometry, flow and mass transfer on biofilm development. *Water research* 134, 280-291.
- Chen, C., Packman, A.I. and Gaillard, J.F. (2008) Pore-scale analysis of permeability reduction resulting from colloid deposition. *Geophysical Research Letters* 35(7).
- Chen, C., Packman, A.I., Zhang, D. and Gaillard, J.F. (2010) A multi-scale investigation of interfacial transport, pore fluid flow, and fine particle deposition in a sediment bed. *Water Resources Research* 46(11).
- Chenu, C. (1993) *Soil Structure/Soil Biota Interrelationships*, pp. 143-156, Elsevier.
- Chenu, C. and Roberson, E. (1996) Diffusion of glucose in microbial extracellular polysaccharide as affected by water potential. *Soil Biology and Biochemistry* 28(7), 877-884.
- Confer, D.R. and Logan, B.E. (1997) Molecular weight distribution of hydrolysis products during the biodegradation of model macromolecules in suspended and biofilm cultures. II. Dextran and dextrin. *Water research* 31(9), 2137-2145.
- Costerton, J.W. (1999) Introduction to biofilm. *International journal of antimicrobial agents* 11(3-4), 217-221.
- Council of the European Communities (1976) Council Directive 76/464/EEC of 4 May 1976 on pollution caused by certain dangerous substances discharged into the aquatic environment of the Community. *Official journal L* 129(18/05), 0023-0029.
- Crittenden, J.C., Trussell, R.R., Hand, D.W., Howe, K. and Tchobanoglous, G. (2012) *MWH's water treatment: principles and design*, John Wiley & Sons.
- Cuny, L., Herrling, M.P., Guthausen, G., Horn, H. and Delay, M. (2015) Magnetic resonance imaging reveals detailed spatial and temporal distribution of iron-based nanoparticles transported through water-saturated porous media. *Journal of contaminant hydrology* 182, 51-62.
- De Kreuk, M., Kishida, N., Tsuneda, S. and Van Loosdrecht, M. (2010) Behavior of polymeric substrates in an aerobic granular sludge system. *Water research* 44(20), 5929-5938.

References

- de Kreuk, M.K., Heijnen, J. and Van Loosdrecht, M. (2005) Simultaneous COD, nitrogen, and phosphate removal by aerobic granular sludge. *Biotechnology and bioengineering* 90(6), 761-769.
- de Kreuk, M.v. and Van Loosdrecht, M. (2004) Selection of slow growing organisms as a means for improving aerobic granular sludge stability. *Water Science and Technology* 49(11-12), 9-17.
- Derlon, N., Wagner, J., da Costa, R.H.R. and Morgenroth, E. (2016) Formation of aerobic granules for the treatment of real and low-strength municipal wastewater using a sequencing batch reactor operated at constant volume. *Water research* 105, 341-350.
- Eggen, R.I., Hollender, J., Joss, A., Schäfer, M. and Stamm, C. (2014) Reducing the discharge of micropollutants in the aquatic environment: the benefits of upgrading wastewater treatment plants, ACS Publications.
- European Parliament and Council of the European Union (2008) Directive 2008/105/EC of the European Parliament and of the Council of 16 December 2008 on environmental quality standards in the field of water policy, amending and subsequently repealing. *Official Journal of the European Union* 348, 84-97.
- Flemming, H.-C. and Wingender, J. (2010) The biofilm matrix. *Nature reviews microbiology* 8(9), 623.
- Frank, J., Ruhl, A.S. and Jekel, M. (2015) Impacts of backwashing on granular activated carbon filters for advanced wastewater treatment. *Water research* 87, 166-174.
- Fundneider, T., Alejo, L. and Lackner, S. (2020) Tertiary phosphorus removal to extremely low levels by coagulation-flocculation and cloth-filtration. *Water Science and Technology* 82(1), 131-143.
- Fundneider, T., Alonso, V.A., Abbt-Braun, G., Wick, A., Albrecht, D. and Lackner, S. (2021a) Empty bed contact time: The key for micropollutant removal in activated carbon filters. *Water research* 191, 116765.
- Fundneider, T., Alonso, V.A., Wick, A., Albrecht, D. and Lackner, S. (2021b) Implications of biological activated carbon filters for micropollutant removal in wastewater treatment. *Water research* 189, 116588.
- Gaillard, J.F., Chen, C., Stonedahl, S.H., Lau, B.L., Keane, D.T. and Packman, A.I. (2007) Imaging of colloidal deposits in granular porous media by X-ray difference micro-tomography. *Geophysical Research Letters* 34(18).
- Giesen, A., De Bruin, L., Niermans, R. and Van der Roest, H. (2013) Advancements in the application of aerobic granular biomass technology for sustainable treatment of wastewater. *Water Practice and Technology* 8(1), 47-54.
- Gladden, L.F. and Mitchell, J. (2011) Measuring adsorption, diffusion and flow in chemical engineering: applications of magnetic resonance to porous media. *New Journal of Physics* 13(3), 035001.
- Godinho, J.R., Chellappah, K., Collins, I., Ng, P., Smith, M. and Withers, P.J. (2019) Time-lapse imaging of particle invasion and deposition in porous media using in situ X-ray radiography. *Journal of Petroleum Science and Engineering* 177, 384-391.
- Graf von der Schulenburg, D., Akpa, B., Gladden, L. and Johns, M. (2008) Non-invasive mass transfer measurements in complex biofilm-coated structures. *Biotechnology and bioengineering* 101(3), 602-608.
- Gujer, W. (1999) *Siedlungswasserwirtschaft*, Springer.
- Hamid, K.I.A., Sanciolo, P., Gray, S., Duke, M. and Muthukumaran, S. (2017) Impact of ozonation and biological activated carbon filtration on ceramic membrane fouling. *Water research* 126, 308-318.
- HaskoningDHW, R. (2020) A to Z NEREDA® Plants.
- Herrling, M.P., Lackner, S., Nirschl, H., Horn, H. and Guthausen, G. (2019) Recent NMR/MRI studies of biofilm structures and dynamics. *Annual Reports on NMR Spectroscopy* 97, 163.

- Herrling, M.P., Weisbrodt, J., Kirkland, C.M., Williamson, N.H., Lackner, S., Codd, S.L., Seymour, J.D., Guthausen, G. and Horn, H. (2017) NMR investigation of water diffusion in different biofilm structures. *Biotechnology and bioengineering* 114(12), 2857-2867.
- Hillenbrand, T., Tettenborn, F., Fuchs, S., Tochovski, S., Metzger, S., Tjoeng, I., Wermter, P., Kersting, M., Hecht, D. and Werbeck, N. (2016) Maßnahmen zur Verminderung des Eintrages von Mikroschadstoffen in die Gewässer–Phase 2. UBA-Texte 60, 2016.
- Holzner, M., Morales, V.L., Willmann, M. and Dentz, M. (2015) Intermittent Lagrangian velocities and accelerations in three-dimensional porous medium flow. *Physical Review E* 92(1), 013015.
- Hoskins, B.C., Fevang, L., Majors, P.D., Sharma, M.M. and Georgiou, G. (1999) Selective imaging of biofilms in porous media by NMR relaxation. *Journal of Magnetic Resonance* 139(1), 67-73.
- Hounsfield, G.N. (1973) Computerized transverse axial scanning (tomography): Part 1. Description of system. *The British journal of radiology* 46(552), 1016-1022.
- Hu, X., Chen, K., Lai, X., Ji, S. and Kaiser, K. (2016) Effects of Fe (III) on biofilm and its extracellular polymeric substances (EPS) in fixed bed biofilm reactors. *Water Science and Technology* 73(9), 2060-2066.
- Iltis, G.C., Armstrong, R.T., Jansik, D.P., Wood, B.D. and Wildenschild, D. (2011) Imaging biofilm architecture within porous media using synchrotron-based X-ray computed microtomography. *Water Resources Research* 47(2).
- Im, D., Nakada, N., Fukuma, Y. and Tanaka, H. (2019) Effects of the inclusion of biological activated carbon on membrane fouling in combined process of ozonation, coagulation and ceramic membrane filtration for water reclamation. *Chemosphere* 220, 20-27.
- Jekel, M. and Czekalla, C. (2016) Wasseraufbereitung – Grundlagen und Verfahren. DVGW Lehr- und Handbuch Wasserversorgung Band 6.
- Kårelid, V., Larsson, G. and Björleinius, B. (2017) Pilot-scale removal of pharmaceuticals in municipal wastewater: Comparison of granular and powdered activated carbon treatment at three wastewater treatment plants. *Journal of environmental management* 193, 491-502.
- Karimifard, S., Li, X., Elowsky, C. and Li, Y. (2021) Modeling the impact of evolving biofilms on flow in porous media inside a microfluidic channel. *Water research* 188, 116536.
- Kim, J.-W., Choi, H. and Pachepsky, Y.A. (2010) Biofilm morphology as related to the porous media clogging. *Water research* 44(4), 1193-1201.
- Kimmich, R. (2012) NMR: tomography, diffusometry, relaxometry, Springer Science & Business Media.
- Kirkland, C.M. (2017) Nuclear magnetic resonance studies of biofilm-porous media systems, Montana State University-Bozeman, College of Engineering.
- Klotz, A.R. (2019) Towards an understanding of mass transfer and hydrodynamics in packed bed reactors using Nuclear Magnetic Resonance, University of Cambridge.
- Knopp, G., Yang, F. and Cornel, P. (2016) Elimination von Mikroverunreinigungen aus biologisch gereinigtem Kommunalabwasser mittels kombinierter Membran- und Aktivkohleadsorptionsverfahren. *gwf Wasser | Abwasser* 157(01), 46-59.
- Kumi, F., Hanping, M., Jianping, H. and Ullah, I. (2015) Review of applying X-ray computed tomography for imaging soil-root physical and biological processes. *International Journal of Agricultural and Biological Engineering* 8(5), 1-14.
- Lani, C. and Zboray, R. (2020) Development of a high frame rate neutron imaging method for two-phase flows. *Nuclear Instruments and Methods in Physics Research Section A: Accelerators, Spectrometers, Detectors and Associated Equipment* 954, 161707.

References

- Layer, M., Adler, A., Reynaert, E., Hernandez, A., Pagni, M., Morgenroth, E., Holliger, C. and Derlon, N. (2019) Organic substrate diffusibility governs microbial community composition, nutrient removal performance and kinetics of granulation of aerobic granular sludge. *Water Research X* 4, 100033.
- Layer, M., Bock, K., Ranzinger, F., Horn, H., Morgenroth, E. and Derlon, N. (2020) Particulate substrate retention in plug-flow and fully-mixed conditions during operation of aerobic granular sludge systems. *Water Research X* 9, 100075.
- Leaf, S. (2018) Taking the P out of pollution: an English perspective on phosphorus stewardship and the Water Framework Directive. *Water and Environment Journal* 32(1), 4-8.
- Lehoux, A.P., Rodts, S., Faure, P., Michel, E., Courtier-Murias, D. and Coussot, P. (2016) Magnetic resonance imaging measurements evidence weak dispersion in homogeneous porous media. *Physical Review E* 94(5), 053107.
- Lewandowski, Z., Altobelli, S., Majors, P. and Fukushima, E. (1992) NMR imaging of hydrodynamics near microbially colonized surfaces. *Water Science and Technology* 26(3-4), 577-584.
- Li, C., Brunner, F., Wagner, M., Lackner, S. and Horn, H. (2018) Quantification of particulate matter attached to the bulk-biofilm interface and its influence on local mass transfer. *Separation and Purification Technology* 197, 86-94.
- Li, J., Ding, L.-B., Cai, A., Huang, G.-X. and Horn, H. (2014) Aerobic sludge granulation in a full-scale sequencing batch reactor. *BioMed research international* 2014.
- Liang, C.-H., Chiang, P.-C. and Chang, E. (2007) Modeling the behaviors of adsorption and biodegradation in biological activated carbon filters. *Water research* 41(15), 3241-3250.
- Manz, B., Volke, F., Goll, D. and Horn, H. (2003) Measuring local flow velocities and biofilm structure in biofilm systems with magnetic resonance imaging (MRI). *Biotechnology and bioengineering* 84(4), 424-432.
- Maurer, M., Gujer, W., Hany, R. and Bachmann, S. (1997) Intracellular carbon flow in phosphorus accumulating organisms from activated sludge systems. *Water research* 31(4), 907-917.
- McSwain, B., Irvine, R., Hausner, M. and Wilderer, P. (2005) Composition and distribution of extracellular polymeric substances in aerobic flocs and granular sludge. *Appl. Environ. Microbiol.* 71(2), 1051-1057.
- Meinel, F., Ruhl, A., Sperlich, A., Zietzschmann, F. and Jekel, M. (2015) Pilot-scale investigation of micropollutant removal with granular and powdered activated carbon. *Water, Air, & Soil Pollution* 226(1), 1-10.
- Metzger, U., Lankes, U., Hardy, E.H., Gordalla, B.C. and Frimmel, F.H. (2006) Monitoring the formation of an *Aureobasidium pullulans* biofilm in a bead-packed reactor via flow-weighted magnetic resonance imaging. *Biotechnology letters* 28(16), 1305-1311.
- Mikolajczyk, G., Huang, L., Wilhelm, M., Dreher, W. and Odenbach, S. (2018) Colloid deposition in monolithic porous media—experimental investigations using x-ray computed microtomography and magnetic resonance velocimetry. *Chemical Engineering Science* 175, 257-266.
- Morgenroth, E., Kommedal, R. and Harremoës, P. (2002) Processes and modeling of hydrolysis of particulate organic matter in aerobic wastewater treatment—a review. *Water Science and Technology* 45(6), 25-40.
- Neu, T.R., Manz, B., Volke, F., Dynes, J.J., Hitchcock, A.P. and Lawrence, J.R. (2010) Advanced imaging techniques for assessment of structure, composition and function in biofilm systems. *FEMS microbiology ecology* 72(1), 1-21.
- Nott, K.P., Paterson-Beedle, M., Macaskie, L.E. and Hall, L.D. (2001) Visualisation of metal deposition in biofilm reactors by three-dimensional magnetic resonance imaging (MRI). *Biotechnology letters* 23(21), 1749-1757.

- O'Toole, G.A. and Kolter, R. (1998) Initiation of biofilm formation in *Pseudomonas fluorescens* WCS365 proceeds via multiple, convergent signalling pathways: a genetic analysis. *Molecular microbiology* 28(3), 449-461.
- Or, D., Phutane, S. and Dechesne, A. (2007a) Extracellular polymeric substances affecting pore-scale hydrologic conditions for bacterial activity in unsaturated soils. *Vadose Zone Journal* 6(2), 298-305.
- Or, D., Smets, B.F., Wraith, J., Dechesne, A. and Friedman, S. (2007b) Physical constraints affecting bacterial habitats and activity in unsaturated porous media—a review. *Advances in water resources* 30(6-7), 1505-1527.
- Orhon, D. and Çokgör, E.U. (1997) COD fractionation in wastewater characterization—the state of the art. *Journal of Chemical Technology & Biotechnology: International Research in Process, Environmental AND Clean Technology* 68(3), 283-293.
- Pereira, H., Lemos, P.C., Reis, M.A., Crespo, J.P., Carrondo, M.J. and Santos, H. (1996) Model for carbon metabolism in biological phosphorus removal processes based on in vivo ¹³C-NMR labelling experiments. *Water research* 30(9), 2128-2138.
- Peszynska, M., Trykozko, A., Iltis, G., Schlueter, S. and Wildenschild, D. (2016) Biofilm growth in porous media: Experiments, computational modeling at the porescale, and upscaling. *Advances in water resources* 95, 288-301.
- Peulen, T.-O. and Wilkinson, K.J. (2011) Diffusion of nanoparticles in a biofilm. *Environmental science & technology* 45(8), 3367-3373.
- Phoenix, V., Holmes, W. and Ramanan, B. (2008) Magnetic resonance imaging (MRI) of heavy-metal transport and fate in an artificial biofilm. *Mineralogical Magazine* 72(1), 483-486.
- Pintelon, T.R., Picioreanu, C., van Loosdrecht, M.C. and Johns, M.L. (2012) The effect of biofilm permeability on bio-clogging of porous media. *Biotechnology and bioengineering* 109(4), 1031-1042.
- Pramanik, B.K., Roddick, F.A. and Fan, L. (2014) Effect of biological activated carbon pre-treatment to control organic fouling in the microfiltration of biologically treated secondary effluent. *Water research* 63, 147-157.
- Pronk, M., Abbas, B., Al-Zuhairy, S., Kraan, R., Kleerebezem, R. and Van Loosdrecht, M. (2015a) Effect and behaviour of different substrates in relation to the formation of aerobic granular sludge. *Applied microbiology and biotechnology* 99(12), 5257-5268.
- Pronk, M., De Kreuk, M., De Bruin, B., Kamminga, P., Kleerebezem, R.v. and Van Loosdrecht, M. (2015b) Full scale performance of the aerobic granular sludge process for sewage treatment. *Water research* 84, 207-217.
- Ramanan, B., Holmes, W.M., Sloan, W.T. and Phoenix, V.R. (2013) Magnetic resonance imaging of mass transport and structure inside a phototrophic biofilm. *Current microbiology* 66(5), 456-461.
- Ranzinger, F., Herrling, M.P., Lackner, S., Grande, V.W., Baniodeh, A., Powell, A.K., Horn, H. and Guthausen, G. (2016) Direct surface visualization of biofilms with high spin coordination clusters using magnetic resonance imaging. *Acta biomaterialia* 31, 167-177.
- Ranzinger, F., Hille-Reichel, A., Zehe, E., Guthausen, G. and Horn, H. (2020a) Quantification of evaporation and drainage processes in unsaturated porous media using Magnetic Resonance Imaging (MRI). *Water Resources Research*.
- Ranzinger, F., Matern, M., Layer, M., Guthausen, G., Wagner, M., Derlon, N. and Horn, H. (2020b) Transport and retention of artificial and real wastewater particles inside a bed of settled aerobic granular sludge assessed applying magnetic resonance imaging. *Water Research X*, 100050.
- Ritman, E.L. (2004) Micro-computed tomography—current status and developments. *Annu. Rev. Biomed. Eng.* 6, 185-208.

References

- Rittmann, B.E. (1993) The significance of biofilms in porous media. *Water Resources Research* 29(7), 2195-2202.
- Roberson, E.B. and Firestone, M.K. (1992) Relationship between desiccation and exopolysaccharide production in a soil *Pseudomonas* sp. *Appl. Environ. Microbiol.* 58(4), 1284-1291.
- Rockhold, M.L., Yarwood, R., Niemet, M.R., Bottomley, P.J. and Selker, J.S. (2002) Considerations for modeling bacterial-induced changes in hydraulic properties of variably saturated porous media. *Advances in water resources* 25(5), 477-495.
- Rocktäschel, T., Klarmann, C., Helmreich, B., Ochoa, J., Boisson, P., Sørensen, K. and Horn, H. (2013) Comparison of two different anaerobic feeding strategies to establish a stable aerobic granulated sludge bed. *Water research* 47(17), 6423-6431.
- Rocktäschel, T., Klarmann, C., Ochoa, J., Boisson, P., Sørensen, K. and Horn, H. (2015) Influence of the granulation grade on the concentration of suspended solids in the effluent of a pilot scale sequencing batch reactor operated with aerobic granular sludge. *Separation and Purification Technology* 142, 234-241.
- Ruiken, C., Breuer, G., Klaversma, E., Santiago, T. and Van Loosdrecht, M. (2013) Sieving wastewater–Cellulose recovery, economic and energy evaluation. *Water research* 47(1), 43-48.
- Scheven, U., Verganelakis, D., Harris, R., Johns, M. and Gladden, L. (2005) Quantitative nuclear magnetic resonance measurements of preasymptotic dispersion in flow through porous media. *Physics of Fluids* 17(11), 117107.
- Schuhmann, S., Schork, N., Beller, K., Nirschl, H., Oerther, T. and Guthausen, G. (2018) In-situ characterization of deposits in ceramic hollow fiber membranes by compressed sensing RARE-MRI. *AIChE journal* 64(11), 4039-4046.
- Schwarzenbeck, N., Erley, R. and Wilderer, P. (2004) Aerobic granular sludge in an SBR-system treating wastewater rich in particulate matter. *Water Science and Technology* 49(11-12), 41-46.
- Sederman, A. and Gladden, L. (2001) MRI as a probe of the deposition of solid fines in a porous medium. *Magnetic resonance imaging* 19(3-4), 565-567.
- Selamet, O., Pasaogullari, U., Spornjak, D., Hussey, D., Jacobson, D. and Mat, M. (2013) Two-phase flow in a proton exchange membrane electrolyzer visualized in situ by simultaneous neutron radiography and optical imaging. *international journal of hydrogen energy* 38(14), 5823-5835.
- Seymour, J.D., Gage, J.P., Codd, S.L. and Gerlach, R. (2004) Anomalous fluid transport in porous media induced by biofilm growth. *Physical review letters* 93(19), 198103.
- Sharp, R.R., Stoodley, P., Adgie, M., Gerlach, R. and Cunningham, A. (2005) Visualization and characterization of dynamic patterns of flow, growth and activity of biofilms growing in porous media. *Water Science and Technology* 52(7), 85-90.
- Sophonsiri, C. and Morgenroth, E. (2004) Chemical composition associated with different particle size fractions in municipal, industrial, and agricultural wastewaters. *Chemosphere* 55(5), 691-703.
- Strobl, M., Manke, I., Kardjilov, N., Hilger, A., Dawson, M. and Banhart, J. (2009) Advances in neutron radiography and tomography. *Journal of Physics D: Applied Physics* 42(24), 243001.
- Sutherland, K.S. and Chase, G. (2011) *Filters and filtration handbook*, Elsevier.
- Tecon, R. and Or, D. (2017) Biophysical processes supporting the diversity of microbial life in soil. *FEMS Microbiology Reviews* 41(5), 599-623.
- Telgmann, U., Borowska, E., Felmeden, J. and Frechen, F.-B. (2020) The locally resolved filtration process for removal of phosphorus and micropollutants with GAC. *Journal of Water Process Engineering* 35, 101236.

- Valiei, A., Kumar, A., Mukherjee, P.P., Liu, Y. and Thundat, T. (2012) A web of streamers: biofilm formation in a porous microfluidic device. *Lab on a Chip* 12(24), 5133-5137.
- Vogel, H.-J. and Roth, K. (2001) Quantitative morphology and network representation of soil pore structure. *Advances in water resources* 24(3-4), 233-242.
- Vogt, S.J., Sanderlin, A.B., Seymour, J.D. and Codd, S.L. (2013) Permeability of a growing biofilm in a porous media fluid flow analyzed by magnetic resonance displacement-relaxation correlations. *Biotechnology and bioengineering* 110(5), 1366-1375.
- Volk, E., Iden, S.C., Furman, A., Durner, W. and Rosenzweig, R. (2016) Biofilm effect on soil hydraulic properties: Experimental investigation using soil-grown real biofilm. *Water Resources Research* 52(8), 5813-5828.
- Wagner, J., Weissbrodt, D.G., Manguin, V., da Costa, R.H.R., Morgenroth, E. and Derlon, N. (2015) Effect of particulate organic substrate on aerobic granulation and operating conditions of sequencing batch reactors. *Water research* 85, 158-166.
- Wagner, M. and Horn, H. (2017) Optical coherence tomography in biofilm research: a comprehensive review. *Biotechnology and bioengineering* 114(7), 1386-1402.
- Wagner, M., Manz, B., Volke, F., Neu, T.R. and Horn, H. (2010) Online assessment of biofilm development, sloughing and forced detachment in tube reactor by means of magnetic resonance microscopy. *Biotechnology and bioengineering* 107(1), 172-181.
- Wang, Z.-W., Liu, Y. and Tay, J.-H. (2005) Distribution of EPS and cell surface hydrophobicity in aerobic granules. *Applied microbiology and biotechnology* 69(4), 469.
- Westbrook, C. and Talbot, J. (2018) *MRI in Practice*, John Wiley & Sons.
- Wilén, B.-M., Liébana, R., Persson, F., Modin, O. and Hermansson, M. (2018) The mechanisms of granulation of activated sludge in wastewater treatment, its optimization, and impact on effluent quality. *Applied microbiology and biotechnology* 102(12), 5005-5020.
- Zheng, W., Zeng, S., Bais, H., LaManna, J.M., Hussey, D.S., Jacobson, D.L. and Jin, Y. (2018) Plant Growth-Promoting Rhizobacteria (PGPR) Reduce Evaporation and Increase Soil Water Retention. *Water Resources Research* 54(5), 3673-3687.